ChemRxiv™

doi.org/10.26434/chemrxiv.13725904.v1

Vibronic Coupling in a Molecular 4f Qubit

Jonathan Marbey, Jon G. C. Kragskow, Christian Dirk Buch, Joscha Nehrkorn, Mykhaylo Ozerov, Stergios Piligkos, Stephen Hill, Nicholas Chilton

Submitted date: 06/02/2021 • Posted date: 08/02/2021

Licence: CC BY-NC-ND 4.0

Citation information: Marbey, Jonathan; Kragskow, Jon G. C.; Buch, Christian Dirk; Nehrkorn, Joscha; Ozerov, Mykhaylo; Piligkos, Stergios; et al. (2021): Vibronic Coupling in a Molecular 4f Qubit. ChemRxiv. Preprint. https://doi.org/10.26434/chemrxiv.13725904.v1

Vibronic coupling, the interaction between molecular vibrations and electronic states, is a pervasive effect that profoundly affects chemical processes. In the case of molecular magnetic materials, vibronic, or spin-phonon, coupling leads to magnetic relaxation, which equates to loss of magnetic memory and loss of phase coherence in molecular magnets and qubits, respectively. The study of vibronic coupling is challenging, and most experimental evidence is indirect. Here we employ far-infrared magnetospectroscopy to probe vibronic transitions in a Yb^{III} molecular qubit directly. We find intense signals near electronic states, which we show arise due to an “envelope effect” in the vibronic coupling Hamiltonian, and we calculate the vibronic coupling fully ab initio to simulate the spectra. We subsequently show that vibronic coupling is strongest for vibrational modes that simultaneously distort the first coordination sphere and break the C_3 symmetry of the molecule. With this knowledge, vibrational modes could be identified and engineered to shift their energy towards or away from particular electronic states to alter their impact. Hence, these findings provide new insights towards developing general guidelines for the control of vibronic coupling in molecules.

File list (3)

yb_trensal_paper_final.docx (1.65 MiB) view on ChemRxiv • download file

yb_trensal_paper_final.pdf (859.00 KiB) view on ChemRxiv • download file

yb_trensal_SI_final.docx (4.33 MiB) view on ChemRxiv • download file

Vibronic coupling in a molecular 4f qubit

Jonathan Marbey[a,b,†], Jon G. C. Kragskow[c,†], Christian D. Buch,[d] Joscha Nehrkorn[a], Mykhaylo Ozerov[a], Stergios Piligkos[d,*], Stephen Hill[a,b,*] and Nicholas F. Chilton[c,*]

[a] National High Magnetic Field Laboratory, Tallahassee, Florida, 32310, United States of America

[b] Department of Physics, Florida State University, Tallahassee, Florida, 32306, United States of America

[c] Department of Chemistry, School of Natural Sciences, University of Manchester, Oxford Road, Manchester, M13 9PL, United Kingdom

[d] Department of Chemistry, University of Copenhagen, DK-2100 Copenhagen, Denmark

[†] These two authors contributed equally to this work.

Email: piligkos@chem.ku.dk; shill@magnet.fsu.edu; nicholas.chilton@manchester.ac.uk

Vibronic coupling, the interaction between molecular vibrations and electronic states, is a pervasive effect that profoundly affects chemical processes. In the case of molecular magnetic materials, vibronic, or spin-phonon, coupling leads to magnetic relaxation, which equates to loss of magnetic memory and loss of phase coherence in molecular magnets and qubits, respectively. The study of vibronic coupling is challenging, and most experimental evidence is indirect. Here we employ far-infrared magnetospectroscopy to probe vibronic transitions in a Yb^{III} molecular qubit directly. We find intense signals near electronic states, which we show arise due to an "envelope effect" in the vibronic coupling Hamiltonian, and we calculate the vibronic coupling fully *ab initio* to simulate the spectra. We subsequently show that vibronic coupling is strongest for vibrational modes that simultaneously distort the first coordination sphere and break the C_3 symmetry of the molecule. With this knowledge, vibrational modes could be identified and engineered to shift their energy towards or away from particular electronic states to alter their impact. Hence, these findings provide new insights towards developing general guidelines for the control of vibronic coupling in molecules.

Vibronic coupling is pervasive – all materials vibrate and have electronic states – and its impact is crucial in many settings. For example, it is thought to be central in photosynthesis[1,2] and in light-harvesting proteins,[3] but, more generally, it is implicated in enantioselective catalysis[4] and luminescent materials,[5] and is pivotal in the operation of molecular qubits[6,7] and single-molecule magnets.[8] Synthetic chemists have made extensive strides in controlling vibronic coupling through judicious molecular design,[9] but the community at large is far from general design guidelines to control such effects. A key roadblock to progress is obtaining direct evidence of vibronic coupling: conventional experiments probing magnetic relaxation and quantum phase coherence only probe the effects of vibronic coupling indirectly,[6–8,10] and studies using direct probes such as ultrafast[9,11] or infrared (IR)[12–14] spectroscopies are rare. To this end, here we perform far-IR magnetospectroscopy (FIRMS)[15,16] measurements on the Yb^{III} qubit [Yb(trensal)] (**1**, where H_3trensal = 2,2,2-tris(salicylideneimino)trimethylamine, Figure 1, chosen due to its extensive existing magnetic and spectroscopic characterisation[10,17–21]) to directly probe the vibronic coupling in this molecule, and develop *ab initio* simulations of the FIRMS map to elucidate the origins of the vibronic transitions. A FIRMS map is obtained from a series of far-IR spectra collected in varying magnetic fields, which is then normalised to remove field-independent signals corresponding to purely vibrational modes. Thus, a FIRMS map highlights vibronic transitions which involve a simultaneous change in both electronic and vibrational states due to absorption of an IR photon; this is distinct from transitions between electronic states induced by absorption of phonons, which are the origin of magnetic relaxation in single-molecule magnets and quantum decoherence in molecular qubits. Nonetheless, we can learn a great deal about these latter effects from measurement and simulation of the vibronic coupling.

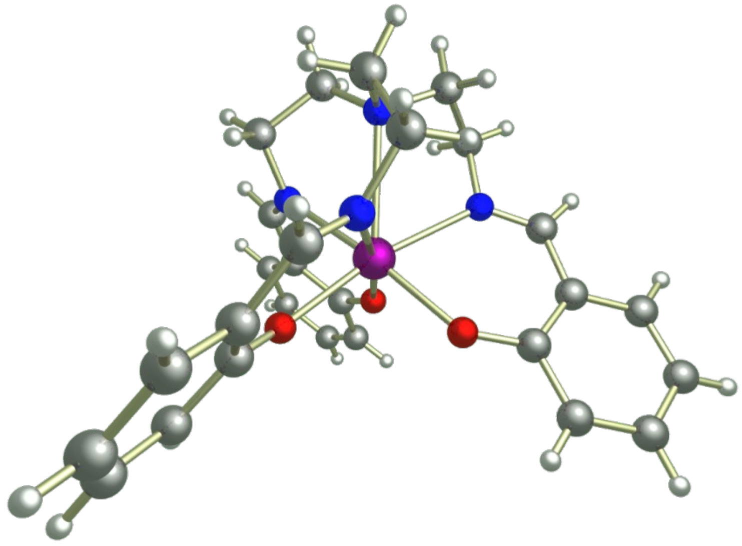

Figure 1. Structure of [Yb(trensal)] (1) viewed perpendicular to the C_3 axis. Hydrogen = white, carbon = grey, nitrogen = blue, oxygen = red, ytterbium = purple.

Complex **1** has C_3 point symmetry and crystallises in the $P\bar{3}c1$ space group. Yb^{III} has a $4f^{13}$ ground configuration which is split into the ground $^2F_{7/2}$ and excited $^2F_{5/2}$ multiplets by spin-orbit coupling (Figure 2, inset), which are then further split by the crystal field (CF) of the molecule; in the absence of a magnetic field all states are doubly degenerate owing to Kramers theorem.[22] Some of us have previously reported near-IR absorption and luminescence measurements of **1** in a diamagnetic host $[Yb_{0.07}Lu_{0.93}(trensal)]$ (**1'**) and have experimentally determined the CF splitting of both spin-orbit multiplets. Fitting the magnetic susceptibility, magnetisation, and optical data simultaneously with a CF Hamiltonian (Tables S1 and S2), yields effective *g*-values for the ground doublet which match those from electron paramagnetic resonance (EPR) spectroscopy.[20] This reveals considerable axial and trigonal contributions to the CF, where nearly all states are mixtures of m_J functions, except for the 3rd Kramers doublet (KD) which comprises the pure $m_J = \pm 3/2$ states as these cannot mix with other m_J states in C_3 symmetry. Additional peaks are found in the luminescence spectrum of **1'** which do not correspond to CF energy levels of the $^2F_{7/2}$ multiplet (Figure 2, *e.g.,* peaks 2a and 2b); these were attributed to "vibrational side-bands" in the original paper,[10] but the true nature of these features was unknown. Herein we collect and perform a detailed theoretical analysis of the FIRMS map of **1** to study the vibronic coupling. We find that vibronic transitions appear near CF states due to a hitherto undescribed "envelope effect", and that vibronic coupling is strongest for vibrational modes that distort the first coordination sphere of Yb^{III} as well as breaking the C_3 point symmetry. Such findings are paramount in unravelling the complex nature of vibronic coupling and for developing future molecular design criteria to deliver control of this phenomenon.

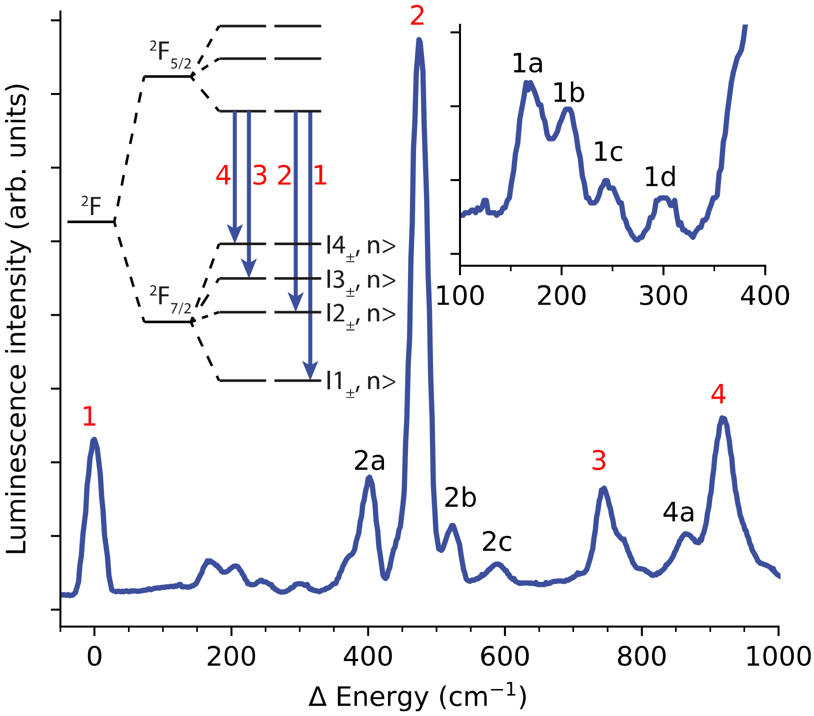

Figure 2. Measurement and assignment of low-lying electronic states in [Yb(trensal)]. Experimental luminescence (emission) spectrum of [Yb$_{0.07}$Lu$_{0.93}$(trensal)] (**1'**) at 5 K.[10] Transitions are from the lowest KD of the excited $^2F_{5/2}$ spin-orbit multiplet to the different KDs of the ground $^2F_{7/2}$ multiplet (inset left; not to scale) and occur in the near-IR around 980 nm.[10,23] The spectrum is plotted as energy differences with respect to the zero-phonon line of the ground KD (peak 1), thus the spectrum is reversed compared to a conventional emission spectrum. The energies of the four KDs of the $^2F_{7/2}$ multiplet, as determined from the spectrum relative to the ground KD at 0 cm^{-1} (1) are: 474 cm^{-1} (2), 745 cm^{-1} (3) and 920 cm^{-1} (4). Additional features are at 169 cm^{-1} (1a), 207 cm^{-1} (1b), 247 cm^{-1} (1c), 302 cm^{-1} (1d), 403 cm^{-1} (2a) and 524 cm^{-1} (2b), 588 cm^{-1} (2c), 864 cm^{-1} (4a).

Results and Discussion

Ab initio electronic structure

Using the structure from X-ray diffraction (XRD), complete active space self-consistent field calculations with extended multi-state perturbative corrections and spin-orbit coupling (CASSCF-XMS-CASPT2-SO; see Methods) are in excellent agreement with the experimentally-determined CF energies, however the first excited state appears ~60 cm^{-1} lower than experiment (Figure S1, Tables S2 and S3). The composition of the ground KD is very similar to the experimental CF model and to EPR data ($g_{\parallel,calc}$ = 4.68 and $g_{\perp,calc}$ = 2.80, *cf.,* $g_{\parallel,\exp}$ = 4.29 and $g_{\perp,\exp}$ = 2.90).[20] Optimisation of the structure of **1** using density-functional theory (DFT, see Methods) yields the structure **1$_{\mathbf{opt}}$** (Table S4), which shows only minor structural changes (root mean squared deviation of 0.127 Å compared to **1**). The vibrational modes of **1$_{\mathbf{opt}}$** are classified as A (singly degenerate) or E (doubly degenerate) irreducible representations of the C_3 point group (Table S5), and we find good agreement between the calculated vibrational energies and the experimental Fourier transform IR (FTIR) spectrum in zero-field (Figure S2). CASSCF-XMS-CASPT2-SO calculations on **1$_{\mathbf{opt}}$** give a slightly worse agreement with the experimental electronic energy spectrum overall (Figure S1), though the first excited state is now only ~30 cm^{-1} higher than the experimental value and the ground state *g*-values remain practically unchanged (Table S6). The considerable impact of small structural changes on the electronic states of **1** (first excited state shifts by ~100 cm^{-1}) indicates that the electronic structure of **1** is highly susceptible to molecular distortion, providing a physical basis for significant vibronic coupling found for this molecule.

FIRMS map and model Hamiltonian

A FIRMS map highlights vibronic transitions driven by IR photons with energy $h\upsilon$. The positions of vibronic transitions are $h\upsilon = \Delta_e \pm \Delta_v$, where Δ_e is the difference in electronic energy and Δ_v is the difference in vibrational energy. The intensity of a vibronic transition in a FIRMS map is related to both the intensities of IR absorption of the pure vibrational and the pure electronic transitions, but also the strength of vibronic coupling between the vibration and the electronic states involved. The FIRMS map for **1** (Figure 3) reproduces the vibronic side-bands observed in luminescence measurements (Figure 2), and reveals evidence of their movement (along with several other features) as a function of applied magnetic field. While the zero-field FTIR spectrum of **1** shows vibrational modes ranging from 0 to 900 cm^{-1}, in good agreement with our DFT calculations (Figure S2), the FIRMS map shows far fewer field-dependent signals that appear in bands from 370-550 cm^{-1} and 740-815 cm^{-1} (Figures 3a and S5b) near the energies of the electronic doublets in **1** (474 and 745 cm^{-1}). Interestingly, the spectrum shows field-dependent vibronic signals below the energy of the first excited doublet (*i.e.*, 370-474 cm^{-1}), which mainly arise from very low-energy intra-KD electronic transitions coupled to vibrational excitations near the observed transition energy (hot transitions are very unlikely at 4.2 K, see below and Figure S3). Given this, it is odd that vibronic transitions are not observed in other ranges with significant IR absorption, for instance around 200 cm^{-1}. We first develop a simple toy model to gain qualitative fundamental understanding of this pattern before moving onto a full *ab initio* analysis of the spectrum.

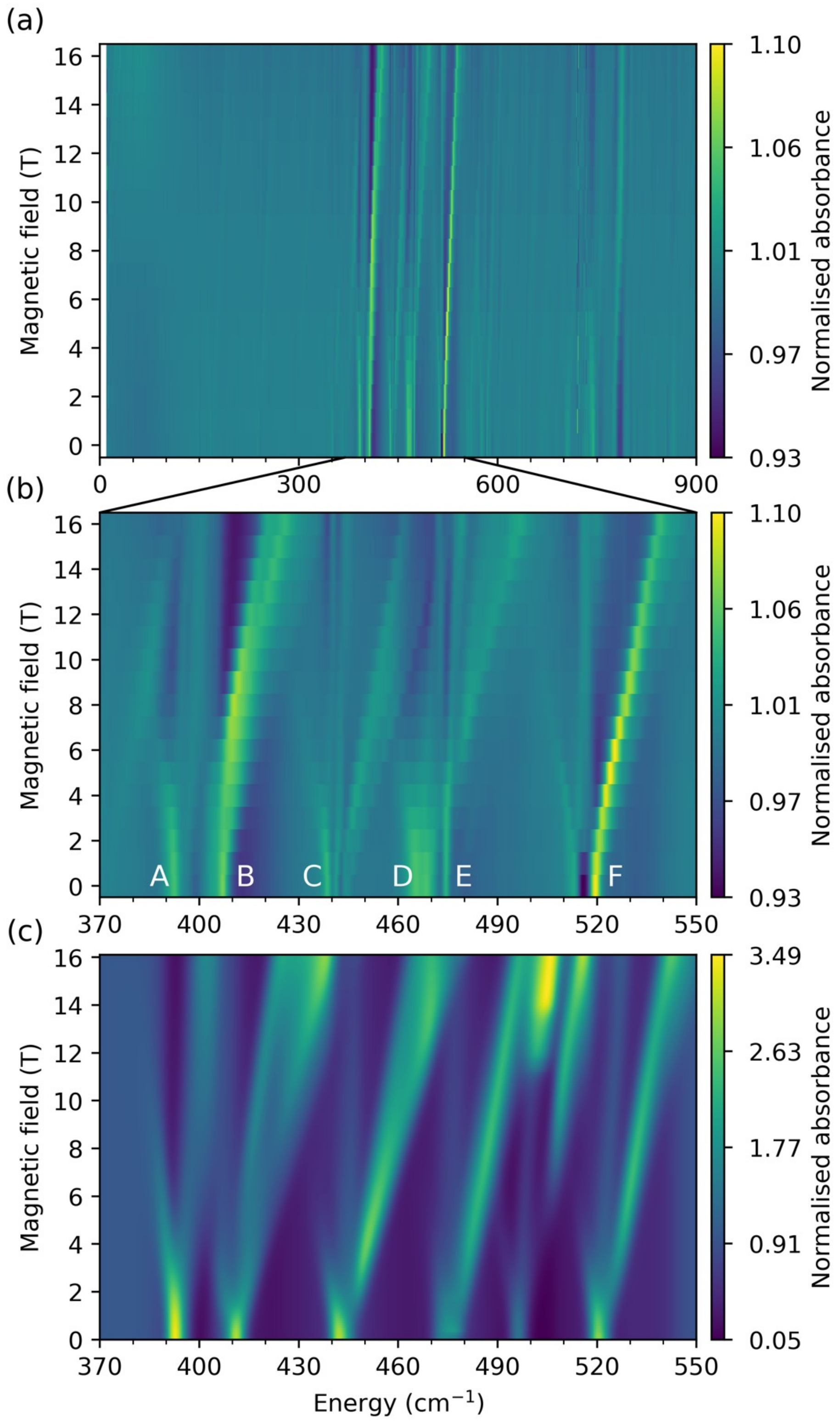

Figure 3. Experimental and simulated FIRMS maps for 1. Experimental FIRMS map measured at 4.2 K in the range (a) 0-900 cm^{-1} and (b) 370-550 cm^{-1} (field dependent signals are labelled as **A**-**F**). (c) Composite *ab initio* simulated FIRMS map for signals **A**-**F** using XMS-CASPT2-SO equilibrium CF parameters with experimental CF energies and CASSCF-SO vibronic couplings (see Methods and Supporting Information); this composite image was generated from two independent simulations including vibrational modes 34-42 and 4-5 (Table S5). The colour bars

show fractional changes in relative transmittance (normalised absorbance) due to the magnetic field.

FIRMS maps have been expertly modelled by Atanasov and Neese,[24] among others,[12–14] and we follow a similar conceptual approach. Our simple toy model consists of two electronic KDs separated by Δ, coupled to a single vibrational mode of energy $\hbar\omega$, for which we consider only the ground $n=0$ and first excited $n=1$ vibrational quantum states. We label the states as $\left|N_{\pm}, n\right\rangle$ where N is the index of the electronic state, ± represents each state of the KD, and n is the vibrational state. For simplicity, we assume both KDs have the same *g*-values and hence parameterize the effect of the magnetic field as $\delta = g\,\mu_B B/2$ (Figure 4). Without vibronic coupling, the zeroth-order Hamiltonian $\hat{H}_0$ of this toy model in the direct product basis ¿ is:

$$\hat{H}_0 = \begin{bmatrix} -\delta & 0 & 0 & 0 & 0 & 0 & 0 & 0 \\ 0 & -\delta+\hbar\omega & 0 & 0 & 0 & 0 & 0 & 0 \\ 0 & 0 & \delta & 0 & 0 & 0 & 0 & 0 \\ 0 & 0 & 0 & \delta+\hbar\omega & 0 & 0 & 0 & 0 \\ 0 & 0 & 0 & 0 & \Delta-\delta & 0 & 0 & 0 \\ 0 & 0 & 0 & 0 & 0 & \Delta-\delta+\hbar\omega & 0 & 0 \\ 0 & 0 & 0 & 0 & 0 & 0 & \Delta+\delta & 0 \\ 0 & 0 & 0 & 0 & 0 & 0 & 0 & \Delta+\delta+\hbar\omega \end{bmatrix} \qquad 1$$

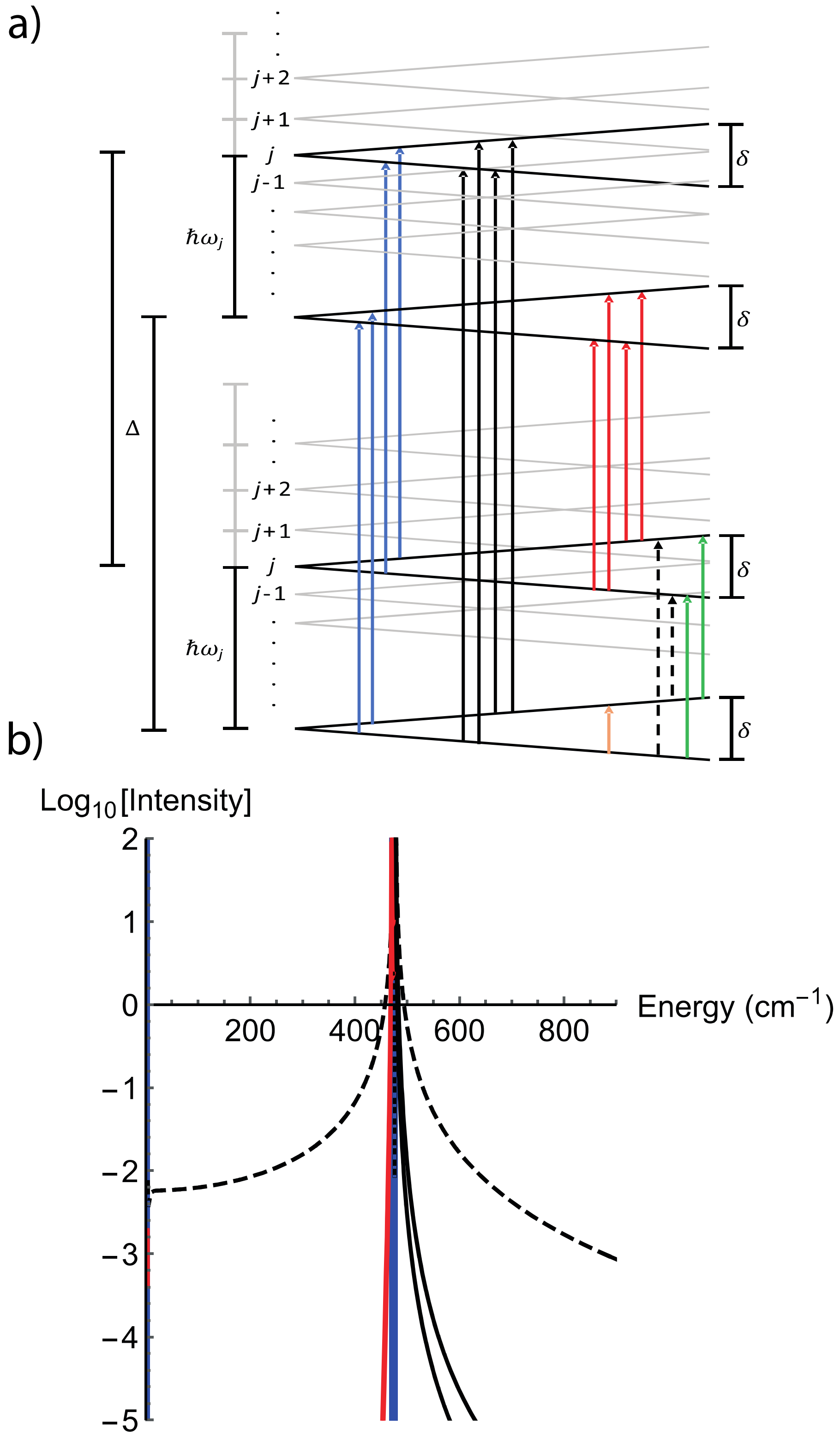

Figure 4. Vibronic states and theoretical FIRMS intensity for toy model. (a) States of toy model; note that the vibrational energy $\hbar\omega_j$ is a variable, and all values are considered in (b). Purely electronic transitions are shown in blue, purely vibrational transitions in green, cold vibronic inter-KD transitions in black, hot vibronic transitions in red, and cold vibronic intra-KD transitions in dashed black; EPR transitions (not studied in this work) in orange. (b) Absorption intensity for cold intra-KD vibronic transitions (black dashed lines), cold inter-KD vibronic transitions (solid black

lines), hot inter-KD vibronic transitions (red solid lines), and purely electronic (solid blue lines) transitions, under irradiation from an IR source with uniform intensity and uniform vibronic coupling. Purely vibrational transitions are not shown. Constructed with model parameters F = G = 0.1 cm^{-1}, A_v = 1, A_e = 10^2, Δ = 474 cm^{-1} and δ = 2 cm^{-1} (field *ca.* 2 T, see Equations 3 and 4).

Vibronic transitions involve a change in both the electronic and vibrational states, otherwise they are purely electronic or purely vibrational. There are two types of vibronic transitions in this toy model: intra-KD transitions (dashed black arrows in Figure 4a) and inter-KD transitions (solid black and red arrows in Figure 4a). Due to the low temperature of the experiment (4.2 K) and large CF splitting (Δ = 474 cm^{-1}), all absorptions must arise from the four initial states ¿ or ¿, and for magnetic fields > 5 T and vibrational modes with $\hbar\omega$ > 20 cm^{-1}, only cold transitions originating from ¿ are relevant (Figure S3). We define the transition matrix elements due to the IR radiation between electronic states as A_e and between vibrational states as A_v (Equation S1). For the system without vibronic coupling described by $\hat{H}_0$, the only possible transitions are purely electronic at $h\upsilon=2\delta$, $h\upsilon=\Delta$ and $h\upsilon=\Delta\pm2\delta$ (intensities proportional to A_e^2) or purely vibrational at $h\upsilon=\hbar\omega$ (intensities proportional to A_v^2); the observation of multiple transitions in the vicinity of a single electronic excitation in the FIRMS map provides direct evidence for the vibronic coupling. Anticipating our *ab initio* model (see Supporting Information), we define the vibronic coupling as perturbations to the electronic states in the weak-coupling limit: diagonal terms G express energy shifts and off-diagonal terms F describe coupling between different electronic states (Equation S2). The coupling Hamiltonian $\hat{H}_1$ in the direct product basis is (block structure highlighted for clarity):

$$\hat{H}_1=\begin{bmatrix} 0 & G & 0 & F & 0 & F & 0 & F \\ G & 0 & F & 0 & F & 0 & F & 0 \\ 0 & F & 0 & G & 0 & F & 0 & F \\ F & 0 & G & 0 & F & 0 & F & 0 \\ 0 & F & 0 & F & 0 & G & 0 & F \\ F & 0 & F & 0 & G & 0 & F & 0 \\ 0 & F & 0 & F & 0 & F & 0 & G \\ F & 0 & F & 0 & F & 0 & G & 0 \end{bmatrix} \tag{2}$$

We can determine the eigenstates of $\hat{H}_0+\hat{H}_1$ with first-order perturbation theory (Equation S3) and hence calculate the intensity of FIRMS transitions. Considering the cold intra-KD vibronic transition (absorption of an IR photon with $h\upsilon=2\delta+\hbar\omega$), under the approximation that $\delta\ll\Delta$ and $\delta\ll\hbar\omega$ we obtain:

$$I\text{¿} \tag{3}$$

The intensity of this transition thus increases when the vibronic coupling (F and G), the electronic transition intensity (A_e) or the vibrational transition intensity (A_v) increase. But notably, the intensity diverges (in first-order perturbation theory, due to coupling between ¿ and ¿) when $\hbar\omega=\Delta$ and, therefore, this toy model predicts that we should expect intense intra-KD vibronic signals when the energy of the vibrational mode is similar to CF gaps in the molecule: because $\delta \ll \hbar\omega$ for such intra-KD transitions, these appear in the regime where$h\upsilon \approx \hbar\omega \approx \Delta$ (Figure 4b; *n.b.*, this transition does not involve absorption of a phonon at $\hbar\omega$ to generate an electronic excitation at Δ). This is a general conclusion that applies to other FIRMS experiments; indeed, such effects have been observed previously but not explained.[12] Similar expressions occur for the inter-KD vibronic transitions (Equations S4 and S5, under the approximation that $\hbar\omega \ll \Delta$ and $\delta \ll \Delta$), that diverge when $\delta \rightarrow 0$ and/or $\hbar\omega \rightarrow 0$ (*i.e.* in proximity to purely electronic transitions). From these results we are able to calculate a theoretical FIRMS intensity spectrum for each class of transition (Figure 4b). As expected from Equations 3, S4 and S5, our theoretical spectrum predicts envelopes of increased intensity for vibronic transitions around $h\upsilon=\Delta$, in agreement with experiment; we expect enhanced vibronic intensity near the second excited KD at 745 cm^{-1} for the same reasons (not included in this toy model). Thus, our toy model explains the “envelope effect” of the FIRMS map with intensity concentrated in the regions 370-550 cm^{-1} and 740-815 cm^{-1}.

Ab initio FIRMS analysis

Moving beyond simple toy models where state energies and vibronic coupling are parameters, we now endeavour to understand the details of the FIRMS map of **1** (Figure 3) by calculating the vibronic coupling *ab initio*. The conceptual framework is similar to the toy model, but now we consider the realistic details of **1**, where the energies of the coupled electronic and vibrational states as a function of magnetic field are obtained from the total Hamiltonian $\widehat{H}_T$:

$$\widehat{H}_T=\widehat{H}_{CF}+\widehat{H}_{Zee}+\sum_j \left[\widehat{H}_{vib,j}+\widehat{H}_{coup,j}\right]=\sum_{k=2,4,6}\sum_{q=-k}^{k} B_k^q \widehat{O}_k^q+\mu_B g_J \vec{B}\cdot\vec{\hat{J}}+\sum_{j=1}^{3N-6}\left[\hbar\omega_j\left(n_j+\right.\right. \quad 4$$

The first and second terms are the electronic CF and Zeeman Hamiltonians, evaluated in the ¿$m_J\rangle$ basis of the ground $^2F_{7/2}$ spin-orbit multiplet of Yb^{III}, the third term is the quantum harmonic oscillator Hamiltonian, evaluated in the basis of vibrational quanta ¿$n_j\rangle$ for mode j, and the fourth term $\widehat{H}_{coup,j}$ is the vibronic coupling Hamiltonian; μ_B is the Bohr magneton, g_J is the Landé *g*-factor for Yb^{III}, $\vec{B}$ is the magnetic field vector, $\vec{\hat{J}}$ is the electronic total angular momentum vector operator, B_k^q are the Stevens CF parameters (CFPs), $\widehat{O}_k^q$ are the Stevens operators, $\hbar\omega_j$ is the energy of vibrational mode j, $\hbar$ is the reduced Planck constant, and N is the number of atoms. As $\widehat{H}_{CF}+\widehat{H}_{Zee}$

commutes with each $\hat{H}_{vib,j}$, and all $\hat{H}_{vib,j}$ commute with one-another in the harmonic approximation, Equation 4 can be written in the direct product basis ¿$m_J, n_1, n_2, \ldots\rangle$ (see Supporting information). $\hat{H}_{CF}$ is constructed using CFPs from CASSCF-XMS-CASPT2-SO calculations (see Methods; this encodes all information on the CF energies and anisotropic *g*-values, but we correct the former to match experiment) and each $\hbar\omega_j$ is obtained from DFT calculations (see Methods), where we only consider the $n_j = 0$ and $n_j = 1$ states (thus ignoring vibrational overtones). To construct each $\hat{H}_{coup,j}$, we expand the CFPs for **1** in a Taylor series in the displacement Q_j along normal mode *j* around equilibrium $Q_{eq} = 0$:[25]

$$B_k^q(Q_j) = B_k^q(Q_{eq}) + \sum_j^{3N-6} Q_j \left(\frac{\partial B_k^q}{\partial Q_j} \right)_{eq} + \frac{1}{2} \sum_j^{3N-6} \sum_{j'}^{3N-6} Q_j Q_{j'} \left(\frac{\partial^2 B_k^q}{\partial Q_j \partial Q_{j'}} \right)_{eq} + \ldots \qquad 5$$

Here, we simulate FIRMS maps by employing a first-order approximation in which the linear term is assumed to be dominant (verified by our *ab initio* calculations, Figure S4). This assumption leads to the vibronic coupling Hamiltonian, Equation 6. We calculate the vibronic coupling coefficients $\left(\frac{\partial B_k^q}{\partial Q_j} \right)_{eq}$ with CASSCF-SO methods, and the matrix representation of Equation 6 is constructed in the direct product basis (see Supporting Information).

$$\hat{H}_{coup,j} = \sum_{k=2,4,6} \sum_{q=-k}^{k} \hat{Q}_j \left(\frac{\partial B_k^q}{\partial Q_j} \right)_{eq} \hat{O}_k^q \qquad 6$$

At equilibrium geometry, the C₃ point symmetry of **1** means that only B_k^q with $q = 0, \pm 3, \pm 6$ are non-zero. However, this constraint can be lost when the molecule vibrates and, thus, up to 27 non-zero $\left(\frac{\partial B_k^q}{\partial Q_j} \right)_{eq}$ contributions to $\hat{H}_{coup,j}$ are possible. Hence, we can also define the overall vibronic coupling strength for each mode as S_j (Equation 7);[26] note here that $B_{k,q}$ are CFPs in Wybourne notation and are linear combinations of the CFPs in Stevens notation B_k^q.[27]

$$S_j = \sqrt{\frac{1}{3} \sum_k \frac{1}{2k+1} \sum_{q=-k}^{k} \left| \left(\frac{\partial B_{k,q}}{\partial Q_j} \right)_{eq} \right|^2} \qquad 7$$

Using this *ab initio* method of vibronic coupling, along with a simple method for calculating transition intensities and spherical integration of the magnetic field to reproduce the powder spectrum (see Supporting Information), we can simulate a FIRMS map for the electronic states of **1** coupled to selections of vibrational modes; calculation of the full vibronic manifold with all vibrational modes is far beyond current computational feasibility, and is not necessary as only modes in energetic proximity of one another need be modelled simultaneously. When considering more than one vibrational mode, $\widehat{H}_{coup,j}$ does not couple them directly (*i.e.*, the $\left(\frac{\partial^2 B_k^q}{\partial Q_j \partial Q_{j'}}\right)_{eq}$ term of Equation 5 is not included in Equation 6), but Equation 4 does allow vibrational mode interactions *via* the electronic states.

We focus on the most intense signals near the first electronic transition (370-550 cm^{-1}, Figure 3), but there is also a strong signal in proximity to the second electronic transition (775 cm^{-1}) and far weaker signals at 167 cm^{-1}, 238 cm^{-1}, 553 cm^{-1} and 581 cm^{-1}, all of which are more distant from any electronic transitions; these are discussed in the Supporting Information, along with a full assignment of the proceeding signals. Examining the 370-550 cm^{-1} region, we can identify intense field-dependent signals emerging from 393, 407, 444, 468, 474, and 520 cm^{-1} in zero-field (**A**-**F**, respectively, Figures 3b and 5). Signals below the first CF state (*i.e.* 370-474 cm^{-1}, **A**-**C**) must mainly be due to cold intra-KD vibronic transitions ($|1_\pm,0\rangle \rightarrow |1_\mp,1\rangle$, Figure 4, because hot transitions are very unlikely at 4.2 K, Figure S3), where the observed energy in the FIRMS map is close to the vibrational energy (as $\delta \ll \hbar\omega$ and hence $h\upsilon = \hbar\omega \pm 2\delta \approx \hbar\omega$). Signals above the electronic excitation (*i.e.* 474-550 cm^{-1}, **D**-**F**) can either be intra- or inter-KD vibronic transitions ($|1_\pm,0\rangle \rightarrow |1_\mp,1\rangle$, $|1_\pm,n\rangle \rightarrow |2_\pm,n'\rangle$ or $|1_\pm,n\rangle \rightarrow |2_\mp,n'\rangle$) or purely electronic transitions ($|1_\pm,n\rangle \rightarrow |2_\pm,n\rangle$, Figure 4). Signals that move to higher energies with increasing field are electronically cold (originating from ¿), whilst those moving to lower energies are electronically hot (originating from ¿). On this basis, and considering the DFT-calculated vibrational spectrum, we can assign signals **A** and **B** (corresponding to peak 2a in the luminescence spectrum, Figure 2) as intra-KD transitions coupled to vibrational modes j = 34-36 (Figure S6, Videos S13-15), and signal **C** as an intra-KD band coupled to modes j = 37-39 (Figure S7, Videos S16-18). Signals **D** and **E** are complicated as they contain contributions from purely electronic and intra-KD bands coupled to modes 40-42 (Figure S8, Videos S19-21); we rule out inter-KD hot bands (requiring $\hbar\omega$ < 20 cm^{-1}) arising from acoustic phonon modes as the vibrational transition intensities will be negligible compared to intramolecular modes. Due to our approximate *ab initio* vibronic couplings, signals **D** and **E** are shifted higher in energy in our simulations versus experiment (see Supporting Information). The intense signal **F** (corresponding to peak 2b in the luminescence spectrum, Figure 2) could either be an intra-KD or an inter-KD vibronic transition, or both; the former would involve either mode 43, and/or modes 44 and 45 (Figure S9, Videos S22-S24) and the latter would involve modes 4 and 5 (Figure S10, Videos S1 and S2). Comparison of our simulations to the experiment suggest that signal **F** is an inter-KD transition coupled to modes 4 and 5, as the alternative, an intra-KD transition coupled to modes 43, 44 and 45, yields additional peaks unobserved in experiment and has the wrong intensity pattern. Hence, we can simulate the FIRMS map of **1** in the 370-550 cm^{-1} range by building a composite (summative) image of our *ab initio* simulations of the maps arising from coupling to vibrational modes 34-42 (signals **A**-**E**) and to modes 4 and 5 (signal **F**; Figure 3c), which shows excellent agreement with the experiment; thus, we are confident in the vibronic assignments (Figure 5).

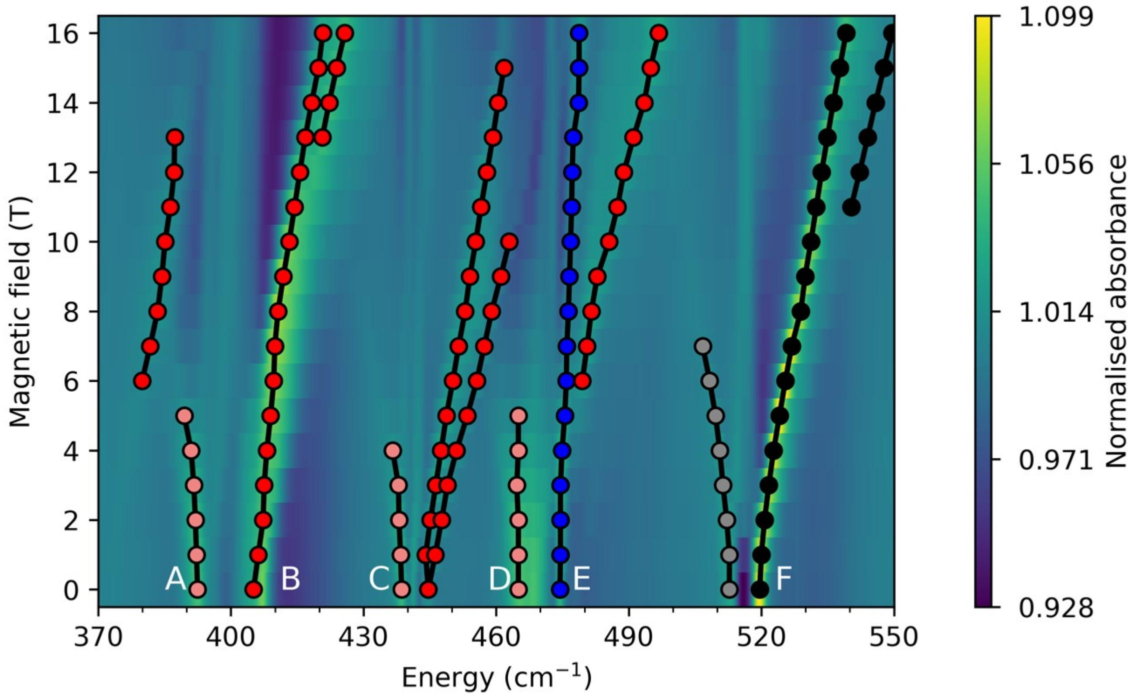

Figure 5. Experimental FIRMS map for 1 with transitions highlighted. Experimental FIRMS map in the range 370-550 cm^{-1}, with purely electronic transitions shown in blue, vibronic inter-KD transitions in black/grey (cold/hot), and vibronic intra-KD transitions in red/pink (cold/hot). Assignments are based on *ab initio* simulation (Figure 3c). Note that the weak field-independent signals (vertical lines) may be pure vibrational modes, but as they appear at the turning points of the raw transmission spectra they could very well be instrumental artefacts.

While the FIRMS map allows us to observe vibronic transitions, we have shown that such spectra are subject to an “envelope effect”, making them most sensitive to transitions near electronic excited states (Figure 4, Equations 3, S4 and S5). As such, these experiments do not provide a direct measure of the strength of the vibronic coupling for all modes. However, our high-quality modelling of the FIRMS map here serves as a detailed benchmark of our *ab initio* calculation of the vibronic coupling and, thus, we are in a position to examine the vibronic coupling strength of all vibrational modes. The values of S for all vibrational modes (Figures 6 and S14, Table S5) reveal that those in the 370-550 cm^{-1} region are not more strongly coupled than modes at other energies. While modes 35 and 36 (responsible for signal **B**) have the second-largest vibronic coupling overall, they have a similar value of S to modes 26 and 27 at 305 cm^{-1}, but we do not see any intra-

KD transitions in this range in the FIRMS experiment; this is due to the envelope effect (Figure 4b). Overall, there are seven pairs of modes with $S > 1.5$ cm^{-1} (7, 8, 14, 15, 20, 21, 22, 23, 26, 27, 35, 36, 142 and 143); interestingly, these modes all have E-symmetry, which break the C_3 point symmetry of the equilibrium structure (see Supplementary Videos). However, it is not as simple as A- *vs.* E-symmetry dictating the strength of vibronic coupling: the modes listed above all involve significant distortions to the first coordination sphere of Yb$^{\mathrm{III}}$ while, for instance, there are E-symmetry modes at 477 and 762 cm^{-1} (modes 41-42 and 58-59, respectively) that involve peripheral motion (see Supplementary Videos) and hence have small S values of 0.20 and 0.03 cm^{-1}, respectively. However, there are also A-symmetry modes that involve distortions to the first coordination sphere which have significantly weaker coupling than the modes that couple most strongly (*e.g.* mode 34 at 406 cm^{-1} with $S = 1.10$ cm^{-1}). Therefore, we can conclude that modes that distort the first coordination sphere and also break the local point symmetry have the strongest vibronic coupling. Further corroborating this analysis, we find that there is excellent agreement between the strongly-coupled modes below 300 cm^{-1} and peaks 1a-d in the luminescence spectrum (Figures 2 and S15). Despite having very strong vibronic coupling, these features are weak in the FIRMS map due to the "envelope effect" (although can be observed, Figure S12), but appear in the luminescence spectrum as this is a spontaneous emission experiment compared to transitions driven by IR photons in FIRMS; the only outlier is the absence of modes 7 and 8 (99 cm^{-1}, $S = 2.03$ cm^{-1}) in the luminescence spectrum which we cannot presently explain.

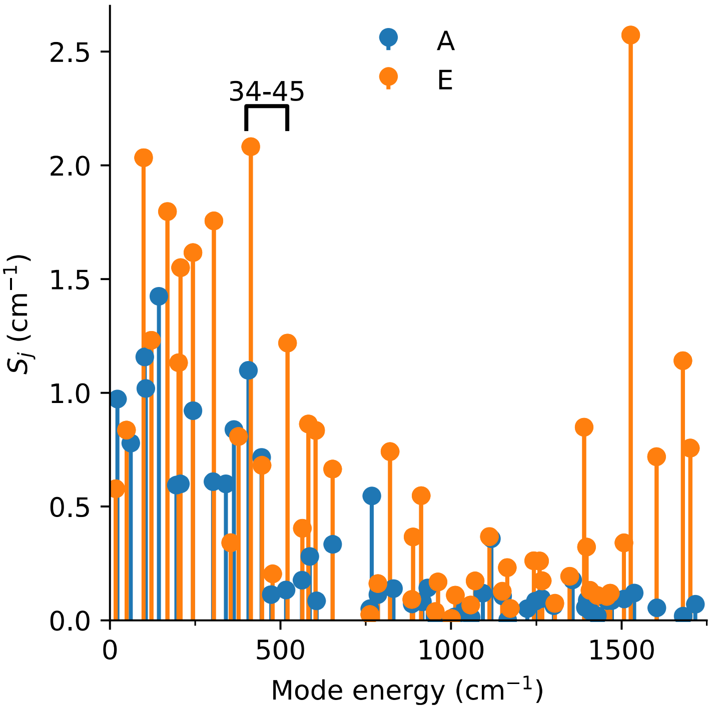

Figure 6. *Ab initio* calculated vibronic coupling strength. S_j of the vibrational modes of **1**$_{\text{opt}}$ with A (blue) and E (orange) symmetry. Modes 34-45 are highlighted.

In summary, we have measured the FIRMS map for [Yb(trensal)] (**1**) and developed an *ab initio* model to calculate the vibronic coupling and hence simulate the map. Our theoretical model shows that vibronic transitions in FIRMS experiments are subject to an “envelope effect” and thus should be most intense near electronic excitations, explaining the structure of our spectra; this is a general phenomenon that has not been found before. Our fully *ab initio* calculation of the FIRMS map shows excellent agreement with experiment and thus directly validates our approach for calculating vibronic coupling. Hence, we can determine the vibrational modes which are most strongly coupled to the electronic states; for [Yb(trensal)] these are E-symmetry modes involving significant motion in the first coordination sphere at 99, 169, 207, 243, 305, 413 and 1527 cm^{-1}. To extract yet more information on the vibronic coupling, future low energy (20-100 cm^{-1}) and single crystal FIRMS experiments will allow direct probing of acoustic phonon modes and anisotropy effects, respectively, which are both crucial in low-temperature Raman relaxation of SMMs and decoherence in spin qubits. Indeed, we can use the same computational methodology to predict magnetic relaxation due to vibronic coupling in single-molecule magnets,[28] and similar methods can be used to directly probe the contribution of vibronic coupling to decoherence in molecular qubits.[29] Only by combined experimental and theoretical studies such as these can we unravel the details of vibronic coupling in molecules and thus begin to develop guidelines for control of this crucial interaction.

Methods

FIRMS measurements

FIRMS measurements were made on 5 mg of a polycrystalline sample of **1** at 4.2 K for IR energies <900 cm^{-1} using a Bruker Vertex 80v vacuum FTIR spectrometer with a resolution of 0.3 cm^{-1}. FTIR spectra were recorded under a series of applied magnetic fields from 0 to 16 T in the Voigt geometry such that propagation of the incident radiation was perpendicular to the applied field. Transmission was detected using a Si bolometer placed immediately behind the sample (in the magnetic field) in order to minimize loss of power. Transmitted intensity spectra were measured in 1 T field steps. Here, the strong field-independent dips in transmission are due to a combination of electric-dipole-active vibrational absorptions and an instrumental function caused by standing waves in the far-IR propagation system (Figure S5a). To improve the signal-to-noise ratio, each FTIR measurement was repeated four times at each field step, then averaged. To distinguish field dependent excitations from those that are field independent, spectra at each magnetic field step were divided by the average of all spectra, resulting in clear “magnetic” spectral features above a more-or-less flat baseline and successful suppression of strong field-independent ‘dips’ in transmittance (Figure 3, Figure S5b). This normalisation procedure does, however, introduce artefacts wherever the raw transmission is near zero (*e.g.* around 0 and 720 cm^{-1}, Figure S5) due to division of zero-by-zero; these 'blind spots' are due to destructive interference in the beam splitter employed in the FTIR spectrometer. We note also that, outside of these blind spots, a few weak field independent signals remain after background division, which could also be instrumental artefacts as they occur at the turning points of the raw transmission spectra. As the measurements were performed on a polycrystalline sample, all molecular orientations in the FIRMS map are sampled at once which, in turn, results in a continuous magnetic field dependent absorption profile superimposed onto the raw FTIR spectrum.

Ab initio calculations

Geometry optimisation and calculation of the normal modes of vibration of **1** was performed in the gas-phase using unrestricted DFT within the Gaussian 09 rev. D package.[30] The X-Ray crystallographic structure was used as a starting point, and all atomic positions were optimised simultaneously. The PBE0 density-functional was used in conjunction with Grimme's D3 dispersion correction,[31–33] the cc-pVDZ basis set was used for carbon and hydrogen atoms and the cc-pVTZ basis set was used for nitrogen and oxygen atoms,[34,35] while the Stuttgart RSC 1997 effective core potential (ECP) was employed for the 28 core electrons of ytterbium and the remaining valence electrons were described with the corresponding valence basis set.[36–38] Symmetry was enabled in the optimisation to preserve the C_3 point group.

We use OpenMolcas to perform CASSCF-(XMS-CASPT2)-SO calculations for the crystallographic, optimised and distorted geometries of **1**.[39] Basis sets from the ANO-RCC library were employed with VTZP quality for Yb, VDZP quality for the N atoms and O atoms, and VDZ quality for all remaining atoms.[40,41] Density fitting of the two-electron integrals using the acCD scheme was performed to speed up the calculations.[42] The active space consisted of thirteen 4f electrons in the seven 4f orbitals of Yb^{III}. State-averaged CASSCF calculations were performed for seven roots of the $S = 1/2$ state and then mixed by spin orbit coupling using the RASSI module.[43] For the crystallographic and optimised structures, CASPT2 corrections to the energies of the seven $S = 1/2$ roots were calculated using the extended multistate (XMS) method prior to RASSI.[44] SINGLE_ANISO was used to decompose the spin orbit wave functions into the crystal field Hamiltonian formalism, using a fixed reference frame determined from the optimised structure.[45] Here we report the crystal field parameters in the context of the Stevens operator equivalent formalism (Table S8).[46]

Data availability

Raw research data files supporting this publication are available at doi: xxxx

References

1 E. Collini, C. Y. Wong, K. E. Wilk, P. M. G. Curmi, P. Brumer and G. D. Scholes, *Nature*, 2010, **463**, 644–647.

2 H. Lee, Y.-C. Cheng and G. R. Fleming, *Science (80-.).*, 2007, **316**, 1462–1465.

3 J. C. Dean, T. Mirkovic, Z. S. D. Toa, D. G. Oblinsky and G. D. Scholes, *Chem*, 2016, **1**, 858–872.

4 A. Milo, E. N. Bess and M. S. Sigman, *Nature*, 2014, **507**, 210–214.

5 C. M. Marian, *Wiley Interdiscip. Rev. Comput. Mol. Sci.*, 2012, **2**, 187–203.

6 A. Gaita-Ariño, F. Luis, S. Hill and E. Coronado, *Nat. Chem.*, 2019, **11**, 301–309.

7 M. Shiddiq, D. Komijani, Y. Duan, A. Gaita-Ariño, E. Coronado and S. Hill, *Nature*, 2016, **531**, 348–351.

8 C. A. P. Goodwin, F. Ortu, D. Reta, N. F. Chilton and D. P. Mills, *Nature*, 2017, **548**, 439–442.

9 B. C. Paulus, S. L. Adelman, L. L. Jamula and J. K. McCusker, *Nature*, 2020, **582**, 214–218.

10 K. S. Pedersen, J. Dreiser, H. Weihe, R. Sibille, H. V. Johannesen, M. A. Sørensen, B. E. Nielsen, M. Sigrist, H. Mutka, S. Rols, J. Bendix and S. Piligkos, *Inorg. Chem.*, 2015, **54**, 7600–7606.

11 F. Liedy, J. Eng, R. McNab, R. Inglis, T. J. Penfold, E. K. Brechin and J. O. Johansson, *Nat. Chem.*, 2020, **12**, 452–458.

12 Y. Rechkemmer, F. D. Breitgoff, M. Van Der Meer, M. Atanasov, M. Hakl, M. Orlita, P. Neugebauer, F. Neese, B. Sarkar and J. Van Slageren, *Nat. Commun.*, 2016, **7**, 10467.

13 D. H. Moseley, S. E. Stavretis, K. Thirunavukkuarasu, M. Ozerov, Y. Cheng, L. L. Daemen, J. Ludwig, Z. Lu, D. Smirnov, C. M. Brown, A. Pandey, A. J. Ramirez-Cuesta, A. C. Lamb, M. Atanasov, E. Bill, F. Neese and Z. L. Xue, *Nat. Commun.*, 2018, **9**, 2572.

14 D. H. Moseley, S. E. Stavretis, Z. Zhu, M. Guo, C. M. Brown, M. Ozerov, Y. Cheng, L. L. Daemen, R. Richardson, G. Knight, K. Thirunavukkuarasu, A. J. Ramirez-Cuesta, J. Tang and Z.-L. Xue, *Inorg. Chem.*, 2020, **59**, 5218–5230.

15 J. C. Hill and R. G. Wheeler, *Phys. Rev.*, 1966, **152**, 482–494.

16 A. J. Sievers and M. Tinkham, *Phys. Rev.*, 1963, **129**, 1995–2004.

17 B. M. Flanagan, P. V Bernhardt, E. R. Krausz, S. R. Lüthi and M. J. Riley, *Inorg. Chem.*, 2002, **41**, 5024–5033.

18 M. Perfetti, E. Lucaccini, L. Sorace, J. P. Costes and R. Sessoli, *Inorg. Chem.*, 2015, **54**,

3090–3092.

19 J. Dreiser, C. Wäckerlin, M. E. Ali, C. Piamonteze, F. Donati, A. Singha, K. S. Pedersen, S. Rusponi, J. Bendix, P. M. Oppeneer, T. A. Jung and H. Brune, *ACS Nano*, 2014, **8**, 4662–4671.

20 K. S. Pedersen, A. M. Ariciu, S. McAdams, H. Weihe, J. Bendix, F. Tuna and S. Piligkos, *J. Am. Chem. Soc.*, 2016, **138**, 5801–5804.

21 R. Hussain, G. Allodi, A. Chiesa, E. Garlatti, D. Mitcov, A. Konstantatos, K. S. Pedersen, R. De Renzi, S. Piligkos and S. Carretta, *J. Am. Chem. Soc.*, 2018, **140**, 9814–9818.

22 H. A. Kramers, *Proc. Acad. Sci.*, 1930, **32**, 1176.

23 J.-C. G. Bünzli and S. V. Eliseeva, in *Lanthanide Luminescence: Photophysical, Analytical and Biological Aspects*, eds. P. Hänninen and H. Härmä, Springer Berlin Heidelberg, Berlin, Heidelberg, 2010, pp. 1–45.

24 M. Atanasov and F. Neese, *J. Phys. Conf. Ser.*, 2018, **1148**, 012006.

25 R. Orbach, *Proc. R. Soc. London. Ser. A. Math. Phys. Sci.*, 1961, **264**, 458–484.

26 N. C. Chang, J. B. Gruber, R. P. Leavitt and C. A. Morrison, *J. Chem. Phys.*, 1982, **76**, 3877–3889.

27 J. Mulak and M. Mulak, *Phys. status solidi*, 2006, **243**, 2796–2810.

28 D. Reta, J. G. C. Kragskow and N. F. Chilton, *ChemRxiv*, , DOI:10.26434/chemrxiv.13606556.v1.

29 L. Escalera-Moreno, N. Suaud, A. Gaita-Ariño and E. Coronado, *J. Phys. Chem. Lett.*, 2017, **8**, 1695–1700.

30 M. J. Frisch, G. W. Trucks, H. B. Schlegel, G. E. Scuseria, M. A. Robb, J. R. Cheeseman, G. Scalmani, V. Barone, G. A. Petersson, H. Nakatsuji, X. Li, M. Caricato, A. Marenich, J. Bloino, B. G. Janesko, R. Gomperts, B. Mennucci, H. P. Hratchian, J. V. Ortiz, A. F. Izmaylov, J. L. Sonnenberg, D. Williams-Young, F. Ding, F. Lipparini, F. Egidi, J. Goings, B. Peng, A. Petrone, T. Henderson, D. Ranasinghe, V. G. Zakrzewski, J. Gao, N. Rega, G. Zheng, W. Liang, M. Hada, M. Ehara, K. Toyota, R. Fukuda, J. Hasegawa, M. Ishida, T. Nakajima, Y. Hondo, O. Kitao, H. Nakai, T. Vreven, K. Throssell, J. A. Montgomery Jr., J. E. Peralta, F. Ogliaro, M. Bearpark, J. J. Heyd, E. Brothers, K. N. Kudin, V. N. Staroverov, T. Keith, R. Kobayashi, J. Normand, K. Raghavachari, A. Rendell, J. C. Burant, S. S. Iyengar, J. Tomasi, M. Cossi, J. M. Millam, M. Klene, C. Adamo, R. Cammi, J. W. Ochterski, R. L. Martin, K. Morokuma, O. Farakas, J. B. Foresman and D. J. Fox, *Gaussian 09, Revision D.01*, Wallingford CT, 2013.

31 S. Grimme, *J. Comput. Chem.*, 2006, **27**, 1787–1799.

32 S. Grimme, *J. Comput. Chem.*, 2004, **25**, 1463–1473.

33 J. P. Perdew, M. Ernzerhof and K. Burke, *J. Chem. Phys.*, 1996, **105**, 9982–9985.

34 D. E. Woon and T. H. Dunning, *J. Chem. Phys.*, 1993, **98**, 1358–1371.

35 T. H. Dunning, *J. Chem. Phys.*, 1989, **90**, 1007–1023.

36 A. Bergner, M. Dolg, W. Küchle, H. Stoll and H. Preuß, *Mol. Phys.*, 1993, **80**, 1431–1441.

37 M. Dolg, H. Stoll, H. Preuss and R. M. Pitzer, *J. Phys. Chem.*, 1993, **97**, 5852–5859.

38 M. Kaupp, P. v. R. Schleyer, H. Stoll and H. Preuss, *J. Chem. Phys.*, 1991, **94**, 1360–1366.

39 I. Fdez. Galván, M. Vacher, A. Alavi, C. Angeli, F. Aquilante, J. Autschbach, J. J. Bao, S. I. Bokarev, N. A. Bogdanov, R. K. Carlson, L. F. Chibotaru, J. Creutzberg, N. Dattani, M. G. Delcey, S. S. Dong, A. Dreuw, L. Freitag, L. M. Frutos, L. Gagliardi, F. Gendron, A. Giussani, L. González, G. Grell, M. Guo, C. E. Hoyer, M. Johansson, S. Keller, S. Knecht, G. Kovačević, E. Källman, G. Li Manni, M. Lundberg, Y. Ma, S. Mai, J. P. Malhado, P. Å. Malmqvist, P. Marquetand, S. A. Mewes, J. Norell, M. Olivucci, M. Oppel, Q. M. Phung, K. Pierloot, F. Plasser, M. Reiher, A. M. Sand, I. Schapiro, P. Sharma, C. J. Stein, L. K. Sørensen, D. G. Truhlar, M. Ugandi, L. Ungur, A. Valentini, S. Vancoillie, V. Veryazov, O. Weser, T. A. Wesołowski, P. O. Widmark, S. Wouters, A. Zech, J. P. Zobel and R. Lindh, *J. Chem. Theory Comput.*, 2019, **15**, 5925–5964.

40 B. O. Roos, V. Veryazov and P.-O. Widmark, *Theor. Chem. Acc.*, 2004, **111**, 345–351.

41 B. O. Roos, R. Lindh, P.-Å. Malmqvist, V. Veryazov and P.-O. Widmark, *J. Phys. Chem. A*, 2005, **109**, 6575–6579.

42 F. Aquilante, R. Lindh and T. Bondo Pedersen, *J. Chem. Phys.*, 2007, **127**, 114107.

43 P. Å. Malmqvist, B. O. Roos and B. Schimmelpfennig, *Chem. Phys. Lett.*, 2002, **357**, 230–240.

44 T. Shiozaki, W. Győrffy, P. Celani and H.-J. Werner, *J. Chem. Phys.*, 2011, **135**, 081106.

45 L. Ungur and L. F. Chibotaru, *Chem. - A Eur. J.*, 2017, **23**, 3708–3718.

46 K. W. H. Stevens, *Proc. Phys. Soc. London Sect. A*, 1952, **65**, 209–215.

Acknowledgements

We thank The University of Manchester for access to the Computational Shared Facility, the EPSRC (studentship to J.G.C.K.), and The Royal Society (University Research Fellowship to N.F.C.). This project has received funding from the European Research Council (ERC) under the European Union’s Horizon 2020 research and innovation programme (grant agreement No.

851504) and the US National Science Foundation (NSF grant numbers DMR-1610226 and DMR-2004732). A portion of this work was performed at the NHMFL which is supported by the NSF (grant number DMR-1644779) and the State of Florida. S.P. thanks the VILLUM FONDEN for research grant 13376. We thank Prof. Richard Winpenny, Prof. Eric McInnes and Dr David Mills for insightful comments.

Author contributions

J.M. and S.H. designed the experiment. C.D.B. synthesised and purified the compound. S.P performed and interpreted the luminescence experiments. J.M., J.N. and M.O. performed the FIRMS measurements. J.G.C.K. and N.F.C. developed theory, wrote code, performed calculations and interpreted spectra. J.M., J.G.C.K., S.H. and N.F.C. wrote the manuscript with contributions from all authors.

Additional information

Supplementary information is available in the online version of the paper. Correspondence and requests for materials should be directed to S.P., S.H and N.F.C.

Competing financial interests

The authors declare no competing financial interests.

yb_trensal_paper_final.docx (1.65 MiB) view on ChemRxiv • download file

Vibronic coupling in a molecular 4f qubit

Jonathan Marbey[a,b,†], Jon G. C. Kragskow[c,†], Christian D. Buch,[d] Joscha Nehrkorn[a], Mykhaylo Ozerov[a], Stergios Piligkos[d,*], Stephen Hill[a,b,*] and Nicholas F. Chilton[c,*]

[a] National High Magnetic Field Laboratory, Tallahassee, Florida, 32310, United States of America

[b] Department of Physics, Florida State University, Tallahassee, Florida, 32306, United States of America

[c] Department of Chemistry, School of Natural Sciences, University of Manchester, Oxford Road, Manchester, M13 9PL, United Kingdom

[d] Department of Chemistry, University of Copenhagen, DK-2100 Copenhagen, Denmark

[†] These two authors contributed equally to this work.

Email: piligkos@chem.ku.dk; shill@magnet.fsu.edu; nicholas.chilton@manchester.ac.uk

Vibronic coupling, the interaction between molecular vibrations and electronic states, is a pervasive effect that profoundly affects chemical processes. In the case of molecular magnetic materials, vibronic, or spin-phonon, coupling leads to magnetic relaxation, which equates to loss of magnetic memory and loss of phase coherence in molecular magnets and qubits, respectively. The study of vibronic coupling is challenging, and most experimental evidence is indirect. Here we employ far-infrared magnetospectroscopy to probe vibronic transitions in a Yb^{III} molecular qubit directly. We find intense signals near electronic states, which we show arise due to an "envelope effect" in the vibronic coupling Hamiltonian, and we calculate the vibronic coupling fully *ab initio* to simulate the spectra. We subsequently show that vibronic coupling is strongest for vibrational modes that simultaneously distort the first coordination sphere and break the C_3 symmetry of the molecule. With this knowledge, vibrational modes could be identified and engineered to shift their energy towards or away from particular electronic states to alter their impact. Hence, these findings provide new insights towards developing general guidelines for the control of vibronic coupling in molecules.

Vibronic coupling is pervasive – all materials vibrate and have electronic states – and its impact is crucial in many settings. For example, it is thought to be central in photosynthesis[1,2] and in light-harvesting proteins,[3] but, more generally, it is implicated in enantioselective catalysis[4] and luminescent materials,[5] and is pivotal in the operation of molecular qubits[6,7] and single-molecule magnets.[8] Synthetic chemists have made extensive strides in controlling vibronic coupling through judicious molecular design,[9] but the community at large is far from general design guidelines to control such effects. A key roadblock to progress is obtaining direct evidence of vibronic coupling: conventional experiments probing magnetic relaxation and quantum phase coherence only probe the effects of vibronic coupling indirectly,[6–8,10] and studies using direct probes such as ultrafast[9,11] or infrared (IR)[12–14] spectroscopies are rare. To this end, here we perform far-IR magnetospectroscopy (FIRMS)[15,16] measurements on the Yb^{III} qubit [Yb(trensal)] (**1**, where H_3trensal = 2,2,2-tris(salicylideneimino)trimethylamine, Figure 1, chosen due to its extensive existing magnetic and spectroscopic characterisation[10,17–21]) to directly probe the vibronic coupling in this molecule, and develop *ab initio* simulations of the FIRMS map to elucidate the origins of the vibronic transitions. A FIRMS map is obtained from a series of far-IR spectra collected in varying magnetic fields, which is then normalised to remove field-independent signals corresponding to purely vibrational modes. Thus, a FIRMS map highlights vibronic transitions which involve a simultaneous change in both electronic and vibrational states due to absorption of an IR photon; this is distinct from transitions between electronic states induced by absorption of phonons, which are the origin of magnetic relaxation in single-molecule magnets and quantum decoherence in molecular qubits. Nonetheless, we can learn a great deal about these latter effects from measurement and simulation of the vibronic coupling.

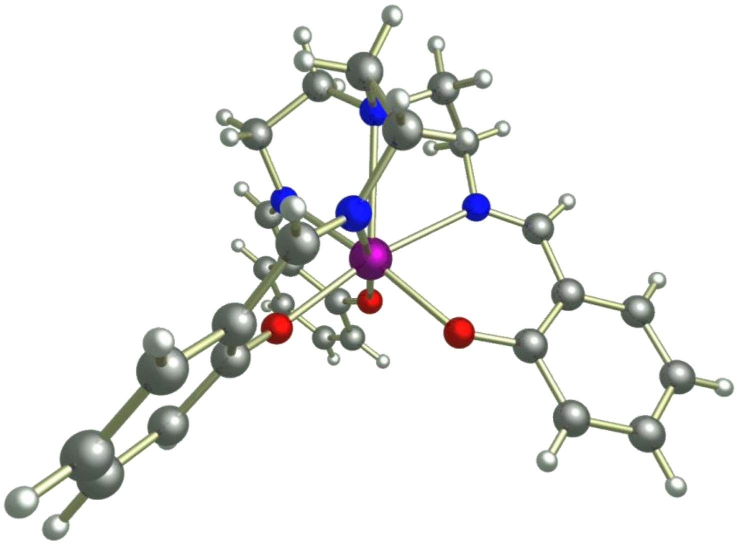

Figure 1. Structure of [Yb(trensal)] (1) viewed perpendicular to the C_3 axis. Hydrogen = white, carbon = grey, nitrogen = blue, oxygen = red, ytterbium = purple.

Complex **1** has C_3 point symmetry and crystallises in the $P\overline{3}c1$ space group. Yb^{III} has a $4f^{13}$ ground configuration which is split into the ground $^2F_{7/2}$ and excited $^2F_{5/2}$ multiplets by spin-orbit coupling (Figure 2, inset), which are then further split by the crystal field (CF) of the molecule; in the absence of a magnetic field all states are doubly degenerate owing to Kramers theorem.[22] Some of us have previously reported near-IR absorption and luminescence measurements of **1** in a diamagnetic host $[Yb_{0.07}Lu_{0.93}$(trensal)] (**1’**) and have experimentally determined the CF splitting of both spin-orbit multiplets. Fitting the magnetic susceptibility, magnetisation, and optical data simultaneously with a CF Hamiltonian (Tables S1 and S2), yields effective *g*-values for the ground doublet which match those from electron paramagnetic resonance (EPR) spectroscopy.[20] This reveals considerable axial and trigonal contributions to the CF, where nearly all states are mixtures of m_J functions, except for the 3rd Kramers doublet (KD) which comprises the pure $m_J = \pm 3/2$ states as these cannot mix with other m_J states in C_3 symmetry. Additional peaks are found in the luminescence spectrum of **1'** which do not correspond to CF energy levels of the ${}^2F_{7/2}$ multiplet (Figure 2, *e.g.,* peaks 2a and 2b); these were attributed to "vibrational side-bands" in the original paper,[10] but the true nature of these features was unknown. Herein we collect and perform a detailed theoretical analysis of the FIRMS map of **1** to study the vibronic coupling. We find that vibronic transitions appear near CF states due to a hitherto undescribed "envelope effect", and that vibronic coupling is strongest for vibrational modes that distort the first coordination sphere of Yb^{III} as well as breaking the C_3 point symmetry. Such findings are paramount in unravelling the complex nature of vibronic coupling and for developing future molecular design criteria to deliver control of this phenomenon.

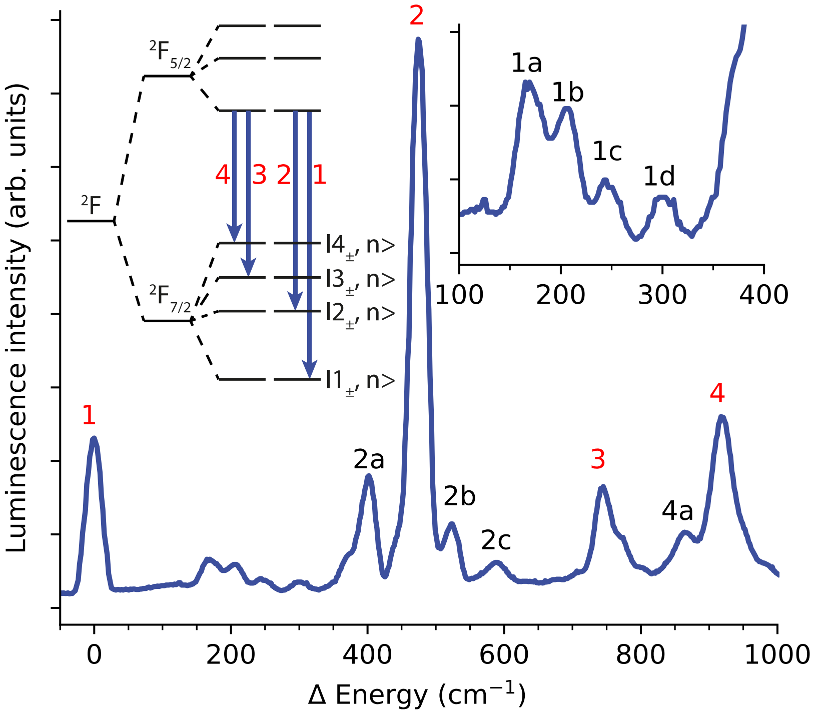

Figure 2. Measurement and assignment of low-lying electronic states in [Yb(trensal)]. Experimental luminescence (emission) spectrum of $[Yb_{0.07}Lu_{0.93}(trensal)]$ (**1'**) at 5 K.[10] Transitions are from the lowest KD of the excited ${}^2F_{5/2}$ spin-orbit multiplet to the different KDs of the ground ${}^2F_{7/2}$ multiplet (inset left; not to scale) and occur in the near-IR around 980 nm.[10,23] The spectrum is plotted as energy differences with respect to the zero-phonon line of the ground KD (peak 1), thus the spectrum is reversed compared to a conventional emission spectrum. The energies of the four KDs of the ${}^2F_{7/2}$ multiplet, as determined from the spectrum relative to the ground KD at 0 cm^{-1} (1) are: 474 cm^{-1} (2), 745 cm^{-1} (3) and 920 cm^{-1} (4). Additional features are at 169 cm^{-1} (1a), 207 cm^{-1} (1b), 247 cm^{-1} (1c), 302 cm^{-1} (1d), 403 cm^{-1} (2a) and 524 cm^{-1} (2b), 588 cm^{-1} (2c), 864 cm^{-1} (4a).

Results and Discussion

Ab initio electronic structure

Using the structure from X-ray diffraction (XRD), complete active space self-consistent field calculations with extended multi-state perturbative corrections and spin-orbit coupling (CASSCF-XMS-CASPT2-SO; see Methods) are in excellent agreement with the experimentally-determined CF energies, however the first excited state appears ~60 cm^{-1} lower than experiment (Figure S1, Tables S2 and S3). The composition of the ground KD is very similar to the experimental CF model and to EPR data ($g_{\parallel,\mathrm{calc}}$ = 4.68 and $g_{\perp,\mathrm{calc}}$ = 2.80, *cf.*, $g_{\parallel,\mathrm{exp}}$ = 4.29 and $g_{\perp,\mathrm{exp}}$ = 2.90).[20] Optimisation of the structure of **1** using density-functional theory (DFT, see Methods) yields the structure $\mathbf{1_{opt}}$ (Table S4), which shows only minor structural changes (root mean squared deviation of 0.127 Å compared to **1**). The vibrational modes of $\mathbf{1_{opt}}$ are classified as A (singly degenerate) or E (doubly degenerate) irreducible representations of the C_3 point group (Table S5), and we find good agreement between the calculated vibrational energies and the experimental Fourier transform IR (FTIR) spectrum in zero-field (Figure S2). CASSCF-XMS-CASPT2-SO calculations on $\mathbf{1_{opt}}$ give a slightly worse agreement with the experimental electronic energy spectrum overall (Figure S1), though the first excited state is now only ~30 cm^{-1} higher than the experimental value and the ground state *g*-values remain practically unchanged (Table S6). The considerable impact of small structural changes on the electronic states of **1** (first excited state shifts by ~100 cm^{-1}) indicates that the electronic structure of **1** is highly susceptible to molecular distortion, providing a physical basis for significant vibronic coupling found for this molecule.

FIRMS map and model Hamiltonian

A FIRMS map highlights vibronic transitions driven by IR photons with energy $h\upsilon$. The positions of vibronic transitions are $h\upsilon = \Delta_\mathrm{e} \pm \Delta_\mathrm{v}$, where Δ_e is the difference in electronic energy and Δ_v is the difference in vibrational energy. The intensity of a vibronic transition in a FIRMS map is related to both the intensities of IR absorption of the pure vibrational and the pure electronic transitions, but also the strength of vibronic coupling between the vibration and the electronic states involved. The FIRMS map for **1** (Figure 3) reproduces the vibronic side-bands observed in luminescence measurements (Figure 2), and reveals evidence of their movement (along with several other features) as a function of applied magnetic field. While the zero-field FTIR spectrum of **1** shows vibrational modes ranging from 0 to 900 cm^{-1}, in good agreement with our DFT calculations (Figure S2), the FIRMS map shows far fewer field-dependent signals that appear in bands from 370-550 cm^{-1} and 740-815 cm^{-1} (Figures 3a and S5b) near the energies of the electronic doublets in **1** (474 and 745 cm^{-1}). Interestingly, the spectrum shows field-dependent vibronic signals below the energy of the first excited doublet (*i.e.*, 370-474 cm^{-1}), which mainly arise from very low-energy intra-KD electronic transitions coupled to vibrational excitations near the observed transition energy (hot transitions are very unlikely at 4.2 K, see below and Figure S3). Given this, it is odd that vibronic transitions are not observed in other ranges with significant IR absorption, for instance around 200 cm^{-1}. We first develop a simple toy model to gain qualitative fundamental understanding of this pattern before moving onto a full *ab initio* analysis of the spectrum.

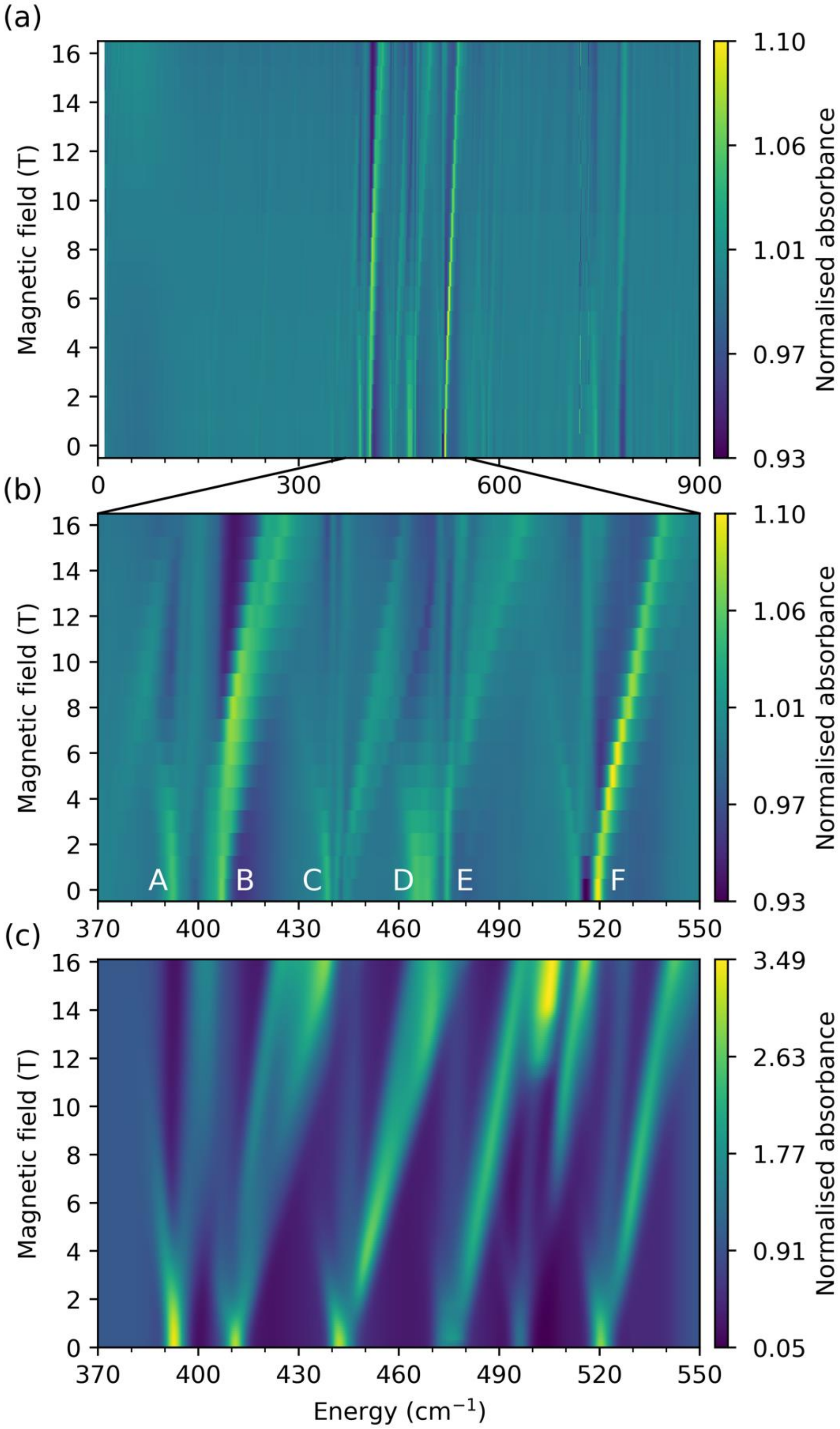

Figure 3. Experimental and simulated FIRMS maps for 1. Experimental FIRMS map measured at 4.2 K in the range (a) 0-900 cm^{-1} and (b) 370-550 cm^{-1} (field dependent signals are labelled as **A**-**F**). (c) Composite *ab initio* simulated FIRMS map for signals **A**-**F** using XMS-CASPT2-SO equilibrium CF parameters with experimental CF energies and CASSCF-SO vibronic couplings (see Methods and Supporting Information); this composite image was generated from two independent simulations including vibrational modes 34-42 and 4-5 (Table S5). The colour bars show fractional changes in relative transmittance (normalised absorbance) due to the magnetic field.

FIRMS maps have been expertly modelled by Atanasov and Neese,[24] among others,[12–14] and we follow a similar conceptual approach. Our simple toy model consists of two electronic KDs separated by Δ, coupled to a single vibrational mode of energy $\hbar\omega$, for which we consider only the ground $n = 0$ and first excited $n = 1$ vibrational quantum states. We label the states as $|N_\pm, n\rangle$ where N is the index of the electronic state, $\pm$ represents each state of the KD, and n is the vibrational state. For simplicity, we assume both KDs have the same *g*-values and hence parameterize the effect of the magnetic field as $\delta = g\mu_\mathrm{B}B/2$ (Figure 4). Without vibronic coupling, the zeroth-order Hamiltonian $\hat{H}_0$ of this toy model in the direct product basis $\{|1_-, 0\rangle, |1_-, 1\rangle, |1_+, 0\rangle, |1_+, 1\rangle, |2_-, 0\rangle, |2_-, 1\rangle, |2_+, 0\rangle, |2_+, 1\rangle\}$ is:

$$\hat{H}_0 = \begin{bmatrix} -\delta & 0 & 0 & 0 & 0 & 0 & 0 & 0 \\ 0 & -\delta + \hbar\omega & 0 & 0 & 0 & 0 & 0 & 0 \\ 0 & 0 & \delta & 0 & 0 & 0 & 0 & 0 \\ 0 & 0 & 0 & \delta + \hbar\omega & 0 & 0 & 0 & 0 \\ 0 & 0 & 0 & 0 & \Delta - \delta & 0 & 0 & 0 \\ 0 & 0 & 0 & 0 & 0 & \Delta - \delta + \hbar\omega & 0 & 0 \\ 0 & 0 & 0 & 0 & 0 & 0 & \Delta + \delta & 0 \\ 0 & 0 & 0 & 0 & 0 & 0 & 0 & \Delta + \delta + \hbar\omega \end{bmatrix} \quad 1$$

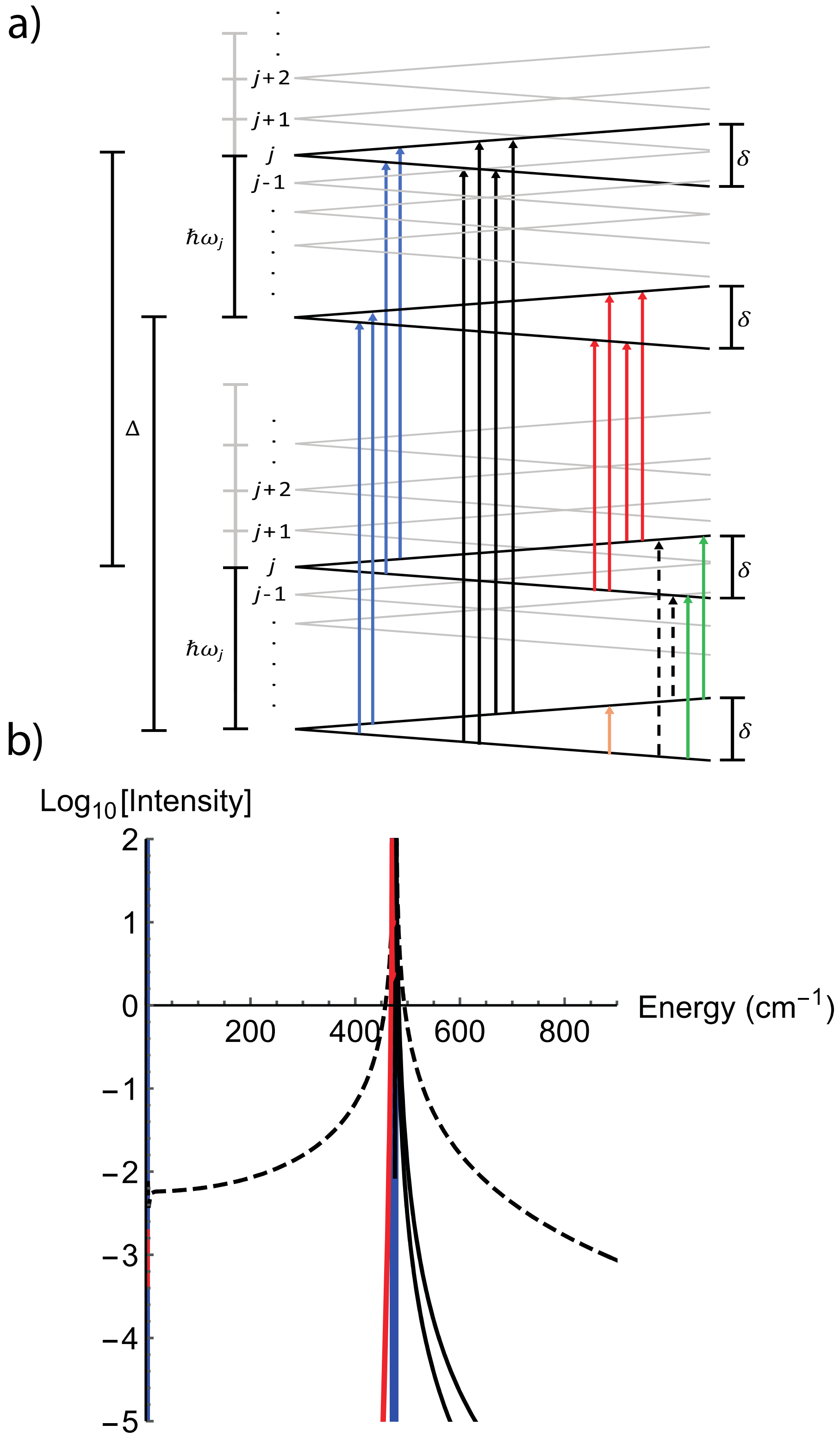

Figure 4. Vibronic states and theoretical FIRMS intensity for toy model. (a) States of toy model; note that the vibrational energy $\hbar\omega_j$ is a variable, and all values are considered in (b). Purely electronic transitions are shown in blue, purely vibrational transitions in green, cold vibronic inter-KD transitions in black, hot vibronic transitions in red, and cold vibronic intra-KD transitions in dashed black; EPR transitions (not studied in this work) in orange. (b) Absorption intensity for cold intra-KD vibronic transitions (black dashed lines), cold inter-KD vibronic transitions (solid black lines), hot

inter-KD vibronic transitions (red solid lines), and purely electronic (solid blue lines) transitions, under irradiation from an IR source with uniform intensity and uniform vibronic coupling. Purely vibrational transitions are not shown. Constructed with model parameters F = G = 0.1 cm^{-1}, A_{v} = 1, A_{e} = 10^{2}, Δ = 474 cm^{-1} and δ = 2 cm^{-1} (field *ca.* 2 T, see Equations 3 and 4).

Vibronic transitions involve a change in both the electronic and vibrational states, otherwise they are purely electronic or purely vibrational. There are two types of vibronic transitions in this toy model: intra-KD transitions (dashed black arrows in Figure 4a) and inter-KD transitions (solid black and red arrows in Figure 4a). Due to the low temperature of the experiment (4.2 K) and large CF splitting (Δ = 474 cm^{-1}), all absorptions must arise from the four initial states $|1_{-},0\rangle, |1_{-},1\rangle, |1_{+},0\rangle$ or $|1_{+},1\rangle$, and for magnetic fields > 5 T and vibrational modes with $\hbar\omega$ > 20 cm^{-1}, only cold transitions originating from $|1_{-},0\rangle$ are relevant (Figure S3). We define the transition matrix elements due to the IR radiation between electronic states as A_{e} and between vibrational states as A_{v} (Equation S1). For the system without vibronic coupling described by $\widehat{H}_0$, the only possible transitions are purely electronic at $hv = 2\delta$, $hv = \Delta$ and $hv = \Delta \pm 2\delta$ (intensities proportional to ${A_{\mathrm{e}}}^2$) or purely vibrational at $hv = \hbar\omega$ (intensities proportional to ${A_{\mathrm{v}}}^2$); the observation of multiple transitions in the vicinity of a single electronic excitation in the FIRMS map provides direct evidence for the vibronic coupling. Anticipating our *ab initio* model (see Supporting Information), we define the vibronic coupling as perturbations to the electronic states in the weak-coupling limit: diagonal terms G express energy shifts and off-diagonal terms F describe coupling between different electronic states (Equation S2). The coupling Hamiltonian $\widehat{H}_1$ in the direct product basis is (block structure highlighted for clarity):

$$\widehat{H}_1 = \begin{bmatrix} 0 & G & 0 & F & 0 & F & 0 & F \\ G & 0 & F & 0 & F & 0 & F & 0 \\ 0 & F & 0 & G & 0 & F & 0 & F \\ F & 0 & G & 0 & F & 0 & F & 0 \\ 0 & F & 0 & F & 0 & G & 0 & F \\ F & 0 & F & 0 & G & 0 & F & 0 \\ 0 & F & 0 & F & 0 & F & 0 & G \\ F & 0 & F & 0 & F & 0 & G & 0 \end{bmatrix} \tag{2}$$

We can determine the eigenstates of $\widehat{H}_0 + \widehat{H}_1$ with first-order perturbation theory (Equation S3) and hence calculate the intensity of FIRMS transitions. Considering the cold intra-KD vibronic transition (absorption of an IR photon with $hv = 2\delta + \hbar\omega$), under the approximation that $\delta \ll \Delta$ and $\delta \ll \hbar\omega$ we obtain:

$$I(|1_{-},0\rangle \rightarrow |1_{+},1\rangle) \propto \left(\frac{2F\left(A_{\mathrm{v}}F\hbar^2\omega^2 - 2A_{\mathrm{e}}\Delta\hbar^2\omega^2 + A_{\mathrm{v}}G(\hbar^2\omega^2 - \Delta^2)\right)}{\hbar^2\omega^2(\hbar^2\omega^2 - \Delta^2)}\right)^2 \tag{3}$$

The intensity of this transition thus increases when the vibronic coupling (F and G), the electronic transition intensity (A_{e}) or the vibrational transition intensity (A_{v}) increase. But notably, the intensity diverges (in first-order perturbation theory, due to coupling between $|1_{+},1\rangle$ and $|2_{+},0\rangle$) when $\hbar\omega = \Delta$ and, therefore, this toy model predicts that we should expect intense intra-KD vibronic signals when the energy of the vibrational mode is similar to CF gaps in the molecule: because $\delta \ll \hbar\omega$ for such intra-KD transitions, these appear in the regime where $h\nu \approx \hbar\omega \approx \Delta$ (Figure 4b; *n.b.*, this transition does not involve absorption of a phonon at $\hbar\omega$ to generate an electronic excitation at Δ). This is a general conclusion that applies to other FIRMS experiments; indeed, such effects have been observed previously but not explained.[12] Similar expressions occur for the inter-KD vibronic transitions (Equations S4 and S5, under the approximation that $\hbar\omega \ll \Delta$ and $\delta \ll \Delta$), that diverge when $\delta \to 0$ and/or $\hbar\omega \to 0$ (*i.e.* in proximity to purely electronic transitions). From these results we are able to calculate a theoretical FIRMS intensity spectrum for each class of transition (Figure 4b). As expected from Equations 3, S4 and S5, our theoretical spectrum predicts envelopes of increased intensity for vibronic transitions around $h\nu = \Delta$, in agreement with experiment; we expect enhanced vibronic intensity near the second excited KD at 745 cm^{-1} for the same reasons (not included in this toy model). Thus, our toy model explains the "envelope effect" of the FIRMS map with intensity concentrated in the regions 370-550 cm^{-1} and 740-815 cm^{-1}.

Ab initio FIRMS analysis

Moving beyond simple toy models where state energies and vibronic coupling are parameters, we now endeavour to understand the details of the FIRMS map of **1** (Figure 3) by calculating the vibronic coupling *ab initio*. The conceptual framework is similar to the toy model, but now we consider the realistic details of **1**, where the energies of the coupled electronic and vibrational states as a function of magnetic field are obtained from the total Hamiltonian $\hat{H}_{\mathrm{T}}$:

$$\begin{aligned}\hat{H}_{\mathrm{T}} &= \hat{H}_{\mathrm{CF}} + \hat{H}_{\mathrm{Zee}} + \sum_{j}\left[\hat{H}_{\mathrm{vib},j} + \hat{H}_{\mathrm{coup},j}\right] \\ &= \sum_{k\,=\,2,4,6}\sum_{q=-k}^{k} B_k^q \hat{O}_k^q + \mu_{\mathrm{B}} g_J \vec{B}\cdot\vec{J} + \sum_{j=1}^{3N-6}\left[\hbar\omega_j\left(n_j + \frac{1}{2}\right) + \hat{H}_{\mathrm{coup},j}\right]\end{aligned} \qquad 4$$

The first and second terms are the electronic CF and Zeeman Hamiltonians, evaluated in the $|m_J\rangle$ basis of the ground $^2F_{7/2}$ spin-orbit multiplet of Yb$^{\mathrm{III}}$, the third term is the quantum harmonic oscillator Hamiltonian, evaluated in the basis of vibrational quanta $|n_j\rangle$ for mode j, and the fourth term $\hat{H}_{\mathrm{coup},j}$ is the vibronic coupling Hamiltonian; μ_{B} is the Bohr magneton, g_J is the Landé *g*-factor for Yb$^{\mathrm{III}}$, $\vec{B}$ is the magnetic field vector, $\vec{J}$ is the electronic total angular momentum vector operator, B_k^q are the Stevens CF parameters (CFPs), $\hat{O}_k^q$ are the Stevens operators, $\hbar\omega_j$ is the energy of vibrational mode j, $\hbar$ is the reduced Planck constant, and N is the number of atoms. As $\hat{H}_{\mathrm{CF}} + \hat{H}_{\mathrm{Zee}}$ commutes with each $\hat{H}_{\mathrm{vib},j}$, and all $\hat{H}_{\mathrm{vib},j}$ commute with one-another in the harmonic approximation, Equation 4 can be written in the direct product basis $|m_J, n_1, n_2, \ldots\rangle$ (see Supporting information). $\hat{H}_{\mathrm{CF}}$ is constructed using CFPs from CASSCF-XMS-CASPT2-SO calculations (see Methods; this encodes all information on the CF energies and anisotropic *g*-values, but we correct the former to match experiment) and each $\hbar\omega_j$ is obtained from DFT calculations (see Methods), where we only consider the $n_j = 0$ and $n_j = 1$ states (thus ignoring vibrational overtones). To construct each $\hat{H}_{\mathrm{coup},j}$, we expand the CFPs for **1** in a Taylor series in the displacement Q_j along normal mode j around equilibrium $Q_{\mathrm{eq}} = 0$:[25]

$$B_k^q(Q_j) = B_k^q(Q_{\mathrm{eq}}) + \sum_j^{3N-6} Q_j \left(\frac{\partial B_k^q}{\partial Q_j}\right)_{\mathrm{eq}} + \frac{1}{2}\sum_j^{3N-6}\sum_{j'}^{3N-6} Q_j Q_{j'} \left(\frac{\partial^2 B_k^q}{\partial Q_j \partial Q_{j'}}\right)_{\mathrm{eq}} + \cdots \qquad 5$$

Here, we simulate FIRMS maps by employing a first-order approximation in which the linear term is assumed to be dominant (verified by our *ab initio* calculations, Figure S4). This assumption leads to the vibronic coupling Hamiltonian, Equation 6. We calculate the vibronic coupling coefficients $\left(\frac{\partial B_k^q}{\partial Q_j}\right)_{\mathrm{eq}}$ with CASSCF-SO methods, and the matrix representation of Equation 6 is constructed in the direct product basis (see Supporting Information).

$$\hat{H}_{\mathrm{coup},j} = \sum_{k=2,4,6} \sum_{q=-k}^{k} \hat{Q}_j \left(\frac{\partial B_k^q}{\partial Q_j}\right)_{\mathrm{eq}} \hat{O}_k^q \qquad 6$$

At equilibrium geometry, the C$_3$ point symmetry of **1** means that only B_k^q with $q = 0, \pm 3, \pm 6$ are non-zero. However, this constraint can be lost when the molecule vibrates and, thus, up to 27 non-zero $\left(\frac{\partial B_k^q}{\partial Q_j}\right)_{\mathrm{eq}}$ contributions to $\hat{H}_{\mathrm{coup},j}$ are possible. Hence, we can also define the overall vibronic coupling strength for each mode as S_j (Equation 7);[26] note here that $\mathcal{B}_{k,q}$ are CFPs in Wybourne notation and are linear combinations of the CFPs in Stevens notation B_k^q.[27]

$$S_j = \sqrt{\frac{1}{3}\sum_k \frac{1}{2k+1} \sum_{q=-k}^{k} \left|\left(\frac{\partial \mathcal{B}_{k,q}}{\partial Q_j}\right)_{\mathrm{eq}}\right|^2} \qquad 7$$

Using this *ab initio* method of vibronic coupling, along with a simple method for calculating transition intensities and spherical integration of the magnetic field to reproduce the powder spectrum (see Supporting Information), we can simulate a FIRMS map for the electronic states of **1** coupled to selections of vibrational modes; calculation of the full vibronic manifold with all vibrational modes is far beyond current computational feasibility, and is not necessary as only modes in energetic proximity of one another need be modelled simultaneously. When considering more than one vibrational mode, $\hat{H}_{\mathrm{coup},j}$ does not couple them directly (*i.e.*, the $\left(\frac{\partial^2 B_k^q}{\partial Q_j \partial Q_{j'}}\right)_{\mathrm{eq}}$ term of Equation 5 is not included in Equation 6), but Equation 4 does allow vibrational mode interactions *via* the electronic states.

We focus on the most intense signals near the first electronic transition (370-550 cm^{-1}, Figure 3), but there is also a strong signal in proximity to the second electronic transition (775 cm^{-1}) and far weaker signals at 167 cm^{-1}, 238 cm^{-1}, 553 cm^{-1} and 581 cm^{-1}, all of which are more distant from any electronic transitions; these are discussed in the Supporting Information, along with a full assignment of the proceeding signals. Examining the 370-550 cm^{-1} region, we can identify intense field-dependent signals emerging from 393, 407, 444, 468, 474, and 520 cm^{-1} in zero-field (**A**-**F**, respectively, Figures 3b and 5). Signals below the first CF state (*i.e.* 370-474 cm^{-1}, **A**-**C**) must mainly be due to cold intra-KD vibronic transitions ($\left|1_{\pm},0\right\rangle \rightarrow |1_{\mp},1\rangle$, Figure 4, because hot transitions are very unlikely at 4.2 K, Figure S3), where the observed energy in the FIRMS map is close to the vibrational energy (as $\delta \ll \hbar\omega$ and hence $hv = \hbar\omega \pm 2\delta \approx \hbar\omega$). Signals above the electronic excitation (*i.e.* 474-550 cm^{-1}, **D**-**F**) can either be intra- or inter-KD vibronic transitions ($\left|1_{\pm},0\right\rangle \rightarrow |1_{\mp},1\rangle$, $\left|1_{\pm},n\right\rangle \rightarrow \left|2_{\pm},n'\right\rangle$ or $\left|1_{\pm},n\right\rangle \rightarrow |2_{\mp},n'\rangle$) or purely electronic transitions ($\left|1_{\pm},n\right\rangle \rightarrow \left|2_{\pm},n\right\rangle$, Figure 4). Signals that move to higher energies with increasing field are electronically cold (originating from $|1_{-},n\rangle$), whilst those moving to lower energies are electronically hot (originating from $|1_{+},n\rangle$). On this basis, and considering the DFT-calculated vibrational spectrum, we can assign signals **A** and **B** (corresponding to peak 2a in the luminescence spectrum, Figure 2) as intra-KD transitions coupled to vibrational modes *j* = 34-36 (Figure S6, Videos S13-15), and signal **C** as an intra-KD band coupled to modes *j* = 37-39 (Figure S7, Videos S16-18). Signals **D** and **E** are complicated as they contain contributions from purely electronic and intra-KD bands coupled to modes 40-42 (Figure S8, Videos S19-21); we rule out inter-KD hot bands (requiring $\hbar\omega$ < 20 cm^{-1}) arising from acoustic phonon modes as the vibrational transition intensities will be negligible compared to intramolecular modes. Due to our approximate *ab initio* vibronic couplings, signals **D** and **E** are shifted higher in energy in our simulations versus experiment (see Supporting Information). The intense signal **F** (corresponding to peak 2b in the luminescence spectrum, Figure 2) could either be an intra-KD or an inter-KD vibronic transition, or both; the former would involve either mode 43, and/or modes 44 and 45 (Figure S9, Videos S22-S24) and the latter would involve modes 4 and 5 (Figure S10, Videos S1 and S2). Comparison of our simulations to the experiment suggest that signal **F** is an inter-KD transition coupled to modes 4 and 5, as the alternative, an intra-KD transition coupled to modes 43, 44 and 45, yields additional peaks unobserved in experiment and has the wrong intensity pattern. Hence, we can simulate the FIRMS map of **1** in the 370-550 cm^{-1} range by building a composite (summative) image of our *ab initio* simulations of the maps arising from coupling to vibrational modes 34-42 (signals **A**-**E**) and to modes 4 and 5 (signal **F**; Figure 3c), which shows excellent agreement with the experiment; thus, we are confident in the vibronic assignments (Figure 5).

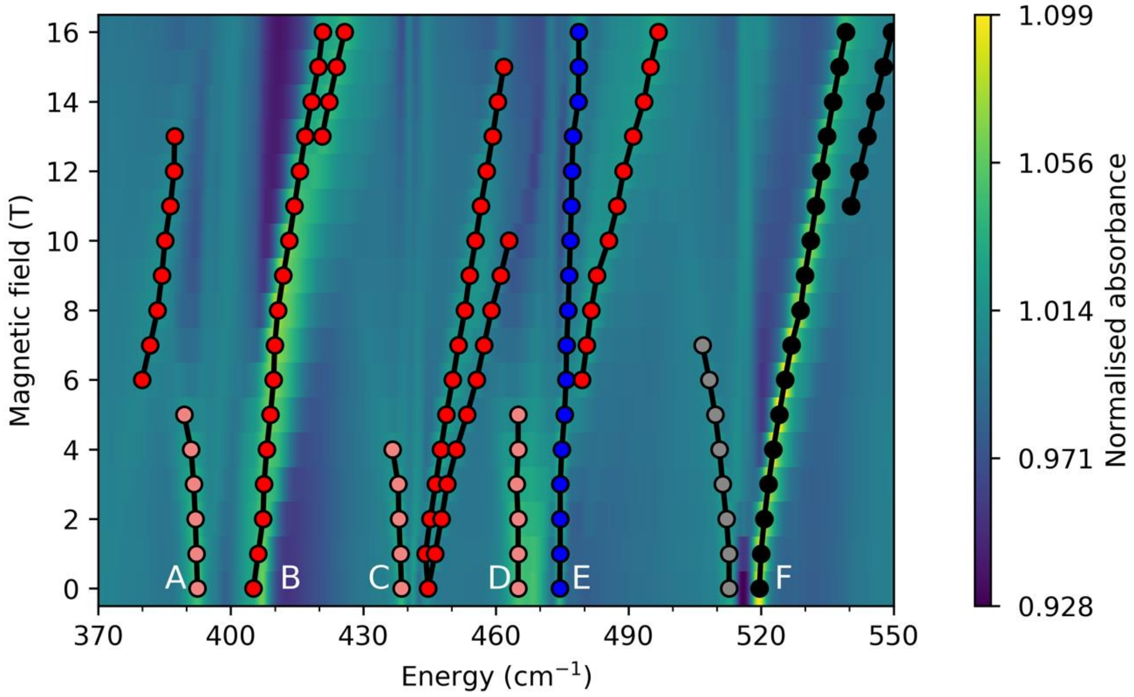

Figure 5. Experimental FIRMS map for 1 with transitions highlighted. Experimental FIRMS map in the range 370-550 cm^{-1}, with purely electronic transitions shown in blue, vibronic inter-KD transitions in black/grey (cold/hot), and vibronic intra-KD transitions in red/pink (cold/hot). Assignments are based on *ab initio* simulation (Figure 3c). Note that the weak field-independent signals (vertical lines) may be pure vibrational modes, but as they appear at the turning points of the raw transmission spectra they could very well be instrumental artefacts.

While the FIRMS map allows us to observe vibronic transitions, we have shown that such spectra are subject to an "envelope effect", making them most sensitive to transitions near electronic excited states (Figure 4, Equations 3, S4 and S5). As such, these experiments do not provide a direct measure of the strength of the vibronic coupling for all modes. However, our high-quality modelling of the FIRMS map here serves as a detailed benchmark of our *ab initio* calculation of the vibronic coupling and, thus, we are in a position to examine the vibronic coupling strength of all vibrational modes. The values of S for all vibrational modes (Figures 6 and S14, Table S5) reveal that those in the 370-550 cm^{-1} region are not more strongly coupled than modes at other energies. While modes 35 and 36 (responsible for signal **B**) have the second-largest vibronic coupling overall, they have a similar value of S to modes 26 and 27 at 305 cm^{-1}, but we do not see any intra-KD transitions in this range in the FIRMS experiment; this is due to the envelope effect (Figure 4b). Overall, there are seven pairs of modes with S > 1.5 cm^{-1} (7, 8, 14, 15, 20, 21, 22, 23, 26, 27, 35, 36, 142 and 143); interestingly, these modes all have E-symmetry, which break the C_3 point symmetry of the equilibrium structure (see Supplementary Videos). However, it is not as simple as A- *vs.* E-symmetry dictating the strength of vibronic coupling: the modes listed above all involve significant distortions to the first coordination sphere of Yb^{III} while, for instance, there are E-symmetry modes at 477 and 762 cm^{-1} (modes 41-42 and 58-59, respectively) that involve peripheral motion (see Supplementary Videos) and hence have small S values of 0.20 and 0.03 cm^{-1}, respectively. However, there are also A-symmetry modes that involve distortions to the first coordination sphere which have significantly weaker coupling than the modes that couple most strongly (*e.g.* mode 34 at 406 cm^{-1} with S = 1.10 cm^{-1}). Therefore, we can conclude that modes that distort the first coordination sphere and also break the local point symmetry have the strongest vibronic coupling. Further corroborating this analysis, we find that there is excellent agreement between the strongly-coupled modes below 300 cm^{-1} and peaks 1a-d in the luminescence spectrum (Figures 2 and S15). Despite having very strong vibronic coupling, these features are weak in the FIRMS map due to the "envelope effect" (although can be observed, Figure S12), but appear in the luminescence spectrum as this is a spontaneous emission experiment compared to transitions driven by IR photons in FIRMS; the only outlier is the absence of modes 7 and 8 (99 cm^{-1}, S = 2.03 cm^{-1}) in the luminescence spectrum which we cannot presently explain.

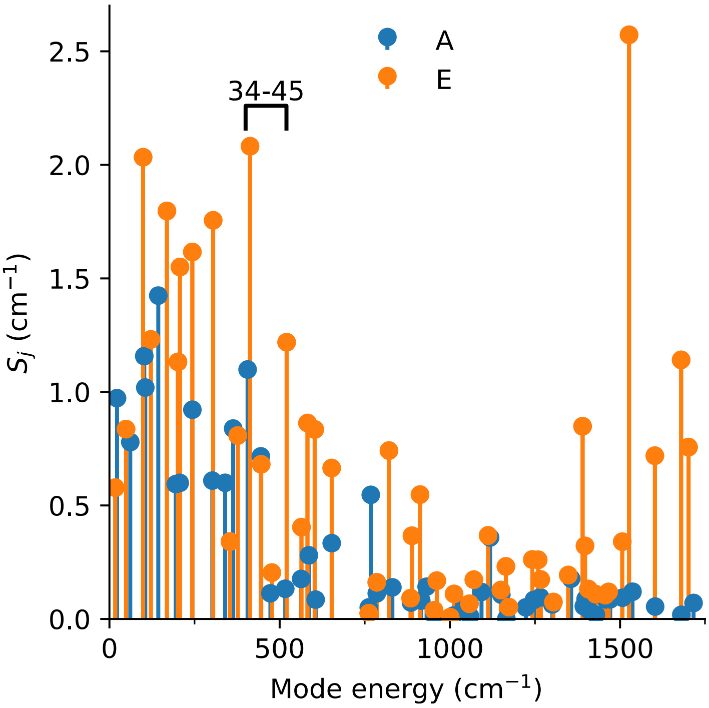

Figure 6. ***Ab initio*** **calculated vibronic coupling strength.** S_j of the vibrational modes of $\mathbf{1}_{\mathbf{opt}}$ with A (blue) and E (orange) symmetry. Modes 34-45 are highlighted.

In summary, we have measured the FIRMS map for [Yb(trensal)] (**1**) and developed an *ab initio* model to calculate the vibronic coupling and hence simulate the map. Our theoretical model shows that vibronic transitions in FIRMS experiments are subject to an "envelope effect" and thus should be most intense near electronic excitations, explaining the structure of our spectra; this is a general phenomenon that has not been found before. Our fully *ab initio* calculation of the FIRMS map shows excellent agreement with experiment and thus directly validates our approach for calculating vibronic coupling. Hence, we can determine the vibrational modes which are most strongly coupled to the electronic states; for [Yb(trensal)] these are E-symmetry modes involving significant motion in the first coordination sphere at 99, 169, 207, 243, 305, 413 and 1527 cm^{-1}. To extract yet more information on the vibronic coupling, future low energy (20-100 cm^{-1}) and single crystal FIRMS experiments will allow direct probing of acoustic phonon modes and anisotropy effects, respectively, which are both crucial in low-temperature Raman relaxation of SMMs and decoherence in spin qubits. Indeed, we can use the same computational methodology to predict magnetic relaxation due to vibronic coupling in single-molecule magnets,[28] and similar methods can be used to directly probe the contribution of vibronic coupling to decoherence in molecular qubits.[29] Only by combined experimental and theoretical studies such as these can we unravel the details of vibronic coupling in molecules and thus begin to develop guidelines for control of this crucial interaction.

Methods

FIRMS measurements

FIRMS measurements were made on 5 mg of a polycrystalline sample of **1** at 4.2 K for IR energies <900 cm^{-1} using a Bruker Vertex 80v vacuum FTIR spectrometer with a resolution of 0.3 cm^{-1}. FTIR spectra were recorded under a series of applied magnetic fields from 0 to 16 T in the Voigt geometry such that propagation of the incident radiation was perpendicular to the applied field. Transmission was detected using a Si bolometer placed immediately behind the sample (in the magnetic field) in order to minimize loss of power. Transmitted intensity spectra were measured in 1 T field steps. Here, the strong field-independent dips in transmission are due to a combination of electric-dipole-active vibrational absorptions and an instrumental function caused by standing waves in the far-IR propagation system (Figure S5a). To improve the signal-to-noise ratio, each FTIR measurement was repeated four times at each field step, then averaged. To distinguish field dependent excitations from those that are field independent, spectra at each magnetic field step were divided by the average of all spectra, resulting in clear “magnetic” spectral features above a more-or-less flat baseline and successful suppression of strong field-independent ‘dips’ in transmittance (Figure 3, Figure S5b). This normalisation procedure does, however, introduce artefacts wherever the raw transmission is near zero (*e.g.* around 0 and 720 cm^{-1}, Figure S5) due to division of zero-by-zero; these ‘blind spots’ are due to destructive interference in the beam splitter employed in the FTIR spectrometer. We note also that, outside of these blind spots, a few weak field independent signals remain after background division, which could also be instrumental artefacts as they occur at the turning points of the raw transmission spectra. As the measurements were performed on a polycrystalline sample, all molecular orientations in the FIRMS map are sampled at once which, in turn, results in a continuous magnetic field dependent absorption profile superimposed onto the raw FTIR spectrum.

Ab initio calculations

Geometry optimisation and calculation of the normal modes of vibration of **1** was performed in the gas-phase using unrestricted DFT within the Gaussian 09 rev. D package.[30] The X-Ray crystallographic structure was used as a starting point, and all atomic positions were optimised simultaneously. The PBE0 density-functional was used in conjunction with Grimme's D3 dispersion correction,[31–33] the cc-pVDZ basis set was used for carbon and hydrogen atoms and the cc-pVTZ basis set was used for nitrogen and oxygen atoms,[34,35] while the Stuttgart RSC 1997 effective core potential (ECP) was employed for the 28 core electrons of ytterbium and the remaining valence electrons were described with the corresponding valence basis set.[36–38] Symmetry was enabled in the optimisation to preserve the C_3 point group.

We use OpenMolcas to perform CASSCF-(XMS-CASPT2)-SO calculations for the crystallographic, optimised and distorted geometries of **1**.[39] Basis sets from the ANO-RCC library were employed with VTZP quality for Yb, VDZP quality for the N atoms and O atoms, and VDZ quality for all remaining atoms.[40,41] Density fitting of the two-electron integrals using the acCD scheme was performed to speed up the calculations.[42] The active space consisted of thirteen 4f electrons in the seven 4f orbitals of $\mathrm{Yb^{III}}$. State-averaged CASSCF calculations were performed for seven roots of the $S = 1/2$ state and then mixed by spin orbit coupling using the RASSI module.[43] For the crystallographic and optimised structures, CASPT2 corrections to the energies of the seven $S = 1/2$ roots were calculated using the extended multistate (XMS) method prior to RASSI.[44] SINGLE_ANISO was used to decompose the spin orbit wave functions into the crystal field Hamiltonian formalism, using a fixed reference frame determined from the optimised structure.[45] Here we report the crystal field parameters in the context of the Stevens operator equivalent formalism (Table S8).[46]

Data availability

Raw research data files supporting this publication are available at doi: xxxx

References

1 E. Collini, C. Y. Wong, K. E. Wilk, P. M. G. Curmi, P. Brumer and G. D. Scholes, *Nature*, 2010, **463**, 644–647.

2 H. Lee, Y.-C. Cheng and G. R. Fleming, *Science (80-.).*, 2007, **316**, 1462–1465.

3 J. C. Dean, T. Mirkovic, Z. S. D. Toa, D. G. Oblinsky and G. D. Scholes, *Chem*, 2016, **1**, 858–872.

4 A. Milo, E. N. Bess and M. S. Sigman, *Nature*, 2014, **507**, 210–214.

5 C. M. Marian, *Wiley Interdiscip. Rev. Comput. Mol. Sci.*, 2012, **2**, 187–203.

6 A. Gaita-Ariño, F. Luis, S. Hill and E. Coronado, *Nat. Chem.*, 2019, **11**, 301–309.

7 M. Shiddiq, D. Komijani, Y. Duan, A. Gaita-Ariño, E. Coronado and S. Hill, *Nature*, 2016, **531**, 348–351.

8 C. A. P. Goodwin, F. Ortu, D. Reta, N. F. Chilton and D. P. Mills, *Nature*, 2017, **548**, 439–442.

9 B. C. Paulus, S. L. Adelman, L. L. Jamula and J. K. McCusker, *Nature*, 2020, **582**, 214–218.

10 K. S. Pedersen, J. Dreiser, H. Weihe, R. Sibille, H. V. Johannesen, M. A. Sørensen, B. E. Nielsen, M. Sigrist, H. Mutka, S. Rols, J. Bendix and S. Piligkos, *Inorg. Chem.*, 2015, **54**, 7600–7606.

11 F. Liedy, J. Eng, R. McNab, R. Inglis, T. J. Penfold, E. K. Brechin and J. O. Johansson, *Nat. Chem.*, 2020, **12**, 452–458.

12 Y. Rechkemmer, F. D. Breitgoff, M. Van Der Meer, M. Atanasov, M. Hakl, M. Orlita, P. Neugebauer, F. Neese, B. Sarkar and J. Van Slageren, *Nat. Commun.*, 2016, **7**, 10467.

13 D. H. Moseley, S. E. Stavretis, K. Thirunavukkuarasu, M. Ozerov, Y. Cheng, L. L. Daemen, J. Ludwig, Z. Lu, D. Smirnov, C. M. Brown, A. Pandey, A. J. Ramirez-Cuesta, A. C. Lamb, M. Atanasov, E. Bill, F. Neese and Z. L. Xue, *Nat. Commun.*, 2018, **9**, 2572.

14 D. H. Moseley, S. E. Stavretis, Z. Zhu, M. Guo, C. M. Brown, M. Ozerov, Y. Cheng, L. L. Daemen, R. Richardson, G. Knight, K. Thirunavukkuarasu, A. J. Ramirez-Cuesta, J. Tang and Z.-L. Xue, *Inorg. Chem.*, 2020, **59**, 5218–5230.

15 J. C. Hill and R. G. Wheeler, *Phys. Rev.*, 1966, **152**, 482–494.

16 A. J. Sievers and M. Tinkham, *Phys. Rev.*, 1963, **129**, 1995–2004.

17 B. M. Flanagan, P. V Bernhardt, E. R. Krausz, S. R. Lüthi and M. J. Riley, *Inorg. Chem.*, 2002, **41**, 5024–5033.

18 M. Perfetti, E. Lucaccini, L. Sorace, J. P. Costes and R. Sessoli, *Inorg. Chem.*, 2015, **54**, 3090–3092.

19 J. Dreiser, C. Wäckerlin, M. E. Ali, C. Piamonteze, F. Donati, A. Singha, K. S. Pedersen, S. Rusponi, J. Bendix, P. M. Oppeneer, T. A. Jung and H. Brune, *ACS Nano*, 2014, **8**, 4662–4671.

20 K. S. Pedersen, A. M. Ariciu, S. McAdams, H. Weihe, J. Bendix, F. Tuna and S. Piligkos, *J. Am. Chem. Soc.*, 2016, **138**, 5801–5804.

21 R. Hussain, G. Allodi, A. Chiesa, E. Garlatti, D. Mitcov, A. Konstantatos, K. S. Pedersen, R. De Renzi, S. Piligkos and S. Carretta, *J. Am. Chem. Soc.*, 2018, **140**, 9814–9818.

22 H. A. Kramers, *Proc. Acad. Sci.*, 1930, **32**, 1176.

23 J.-C. G. Bünzli and S. V. Eliseeva, in *Lanthanide Luminescence: Photophysical, Analytical and Biological Aspects*, eds. P. Hänninen and H. Härmä, Springer Berlin Heidelberg, Berlin, Heidelberg, 2010, pp. 1–45.

24 M. Atanasov and F. Neese, *J. Phys. Conf. Ser.*, 2018, **1148**, 012006.

25 R. Orbach, *Proc. R. Soc. London. Ser. A. Math. Phys. Sci.*, 1961, **264**, 458–484.

26 N. C. Chang, J. B. Gruber, R. P. Leavitt and C. A. Morrison, *J. Chem. Phys.*, 1982, **76**, 3877–3889.

27 J. Mulak and M. Mulak, *Phys. status solidi*, 2006, **243**, 2796–2810.

28 D. Reta, J. G. C. Kragskow and N. F. Chilton, *ChemRxiv*, , DOI:10.26434/chemrxiv.13606556.v1.

29 L. Escalera-Moreno, N. Suaud, A. Gaita-Ariño and E. Coronado, *J. Phys. Chem. Lett.*, 2017, **8**, 1695–1700.

30 M. J. Frisch, G. W. Trucks, H. B. Schlegel, G. E. Scuseria, M. A. Robb, J. R. Cheeseman, G. Scalmani, V. Barone, G. A. Petersson, H. Nakatsuji, X. Li, M. Caricato, A. Marenich, J. Bloino, B. G. Janesko, R. Gomperts, B. Mennucci, H. P. Hratchian, J. V. Ortiz, A. F. Izmaylov, J. L. Sonnenberg, D. Williams-Young, F. Ding, F. Lipparini, F. Egidi, J. Goings, B. Peng, A. Petrone, T. Henderson, D. Ranasinghe, V. G. Zakrzewski, J. Gao, N. Rega, G. Zheng, W. Liang, M. Hada, M. Ehara, K. Toyota, R. Fukuda, J. Hasegawa, M. Ishida, T. Nakajima, Y. Hondo, O. Kitao, H. Nakai, T. Vreven, K. Throssell, J. A. Montgomery Jr., J. E. Peralta, F. Ogliaro, M. Bearpark, J. J. Heyd, E. Brothers, K. N. Kudin, V. N. Staroverov, T. Keith, R. Kobayashi, J. Normand, K. Raghavachari, A. Rendell, J. C. Burant, S. S. Iyengar, J. Tomasi, M. Cossi, J. M. Millam, M. Klene, C. Adamo, R. Cammi, J. W. Ochterski, R. L. Martin, K. Morokuma, O. Farakas, J. B. Foresman and D. J. Fox, *Gaussian 09, Revision D.01*, Wallingford CT, 2013.

31 S. Grimme, *J. Comput. Chem.*, 2006, **27**, 1787–1799.

32 S. Grimme, *J. Comput. Chem.*, 2004, **25**, 1463–1473.

33 J. P. Perdew, M. Ernzerhof and K. Burke, *J. Chem. Phys.*, 1996, **105**, 9982–9985.

34 D. E. Woon and T. H. Dunning, *J. Chem. Phys.*, 1993, **98**, 1358–1371.

35 T. H. Dunning, *J. Chem. Phys.*, 1989, **90**, 1007–1023.

36 A. Bergner, M. Dolg, W. Küchle, H. Stoll and H. Preuß, *Mol. Phys.*, 1993, **80**, 1431–1441.

37 M. Dolg, H. Stoll, H. Preuss and R. M. Pitzer, *J. Phys. Chem.*, 1993, **97**, 5852–5859.

38 M. Kaupp, P. v. R. Schleyer, H. Stoll and H. Preuss, *J. Chem. Phys.*, 1991, **94**, 1360–1366.

39 I. Fdez. Galván, M. Vacher, A. Alavi, C. Angeli, F. Aquilante, J. Autschbach, J. J. Bao, S. I. Bokarev, N. A. Bogdanov, R. K. Carlson, L. F. Chibotaru, J. Creutzberg, N. Dattani, M. G. Delcey, S. S. Dong, A. Dreuw, L. Freitag, L. M. Frutos, L. Gagliardi, F. Gendron, A. Giussani, L. González, G. Grell, M. Guo, C. E. Hoyer, M. Johansson, S. Keller, S. Knecht, G. Kovačević, E. Källman, G. Li Manni, M. Lundberg, Y. Ma, S. Mai, J. P. Malhado, P. Å. Malmqvist, P. Marquetand, S. A. Mewes, J. Norell, M. Olivucci, M. Oppel, Q. M. Phung, K. Pierloot, F. Plasser, M. Reiher, A. M. Sand, I. Schapiro, P. Sharma, C. J. Stein, L. K. Sørensen, D. G. Truhlar, M. Ugandi, L. Ungur, A. Valentini, S. Vancoillie, V. Veryazov, O. Weser, T. A. Wesołowski, P. O. Widmark, S. Wouters, A. Zech, J. P. Zobel and R. Lindh, *J. Chem. Theory Comput.*, 2019, **15**, 5925–5964.

40 B. O. Roos, V. Veryazov and P.-O. Widmark, *Theor. Chem. Acc.*, 2004, **111**, 345–351.

41 B. O. Roos, R. Lindh, P.-Å. Malmqvist, V. Veryazov and P.-O. Widmark, *J. Phys. Chem. A*, 2005, **109**, 6575–6579.

42 F. Aquilante, R. Lindh and T. Bondo Pedersen, *J. Chem. Phys.*, 2007, **127**, 114107.

43 P. Å. Malmqvist, B. O. Roos and B. Schimmelpfennig, *Chem. Phys. Lett.*, 2002, **357**, 230–240.

44 T. Shiozaki, W. Győrffy, P. Celani and H.-J. Werner, *J. Chem. Phys.*, 2011, **135**, 081106.

45 L. Ungur and L. F. Chibotaru, *Chem. - A Eur. J.*, 2017, **23**, 3708–3718.

46 K. W. H. Stevens, *Proc. Phys. Soc. London Sect. A*, 1952, **65**, 209–215.

Acknowledgements

We thank The University of Manchester for access to the Computational Shared Facility, the EPSRC (studentship to J.G.C.K.), and The Royal Society (University Research Fellowship to N.F.C.). This project has received funding from the European Research Council (ERC) under the European Union's Horizon 2020 research and innovation programme (grant agreement No. 851504) and the US National Science Foundation (NSF grant numbers DMR-1610226 and DMR-2004732). A portion of this work was performed at the NHMFL which is supported by the NSF (grant number DMR-1644779) and the State of Florida. S.P. thanks the VILLUM FONDEN for research grant 13376. We thank Prof. Richard Winpenny, Prof. Eric McInnes and Dr David Mills for insightful comments.

Author contributions

J.M. and S.H. designed the experiment. C.D.B. synthesised and purified the compound. S.P performed and interpreted the luminescence experiments. J.M., J.N. and M.O. performed the FIRMS measurements. J.G.C.K. and N.F.C. developed theory, wrote code, performed calculations and interpreted spectra. J.M., J.G.C.K., S.H. and N.F.C. wrote the manuscript with contributions from all authors.

Additional information

Supplementary information is available in the online version of the paper. Correspondence and requests for materials should be directed to S.P., S.H and N.F.C.

Competing financial interests

The authors declare no competing financial interests.

yb_trensal_paper_final.pdf (859.00 KiB) view on ChemRxiv • download file

Supporting Information for: Vibronic coupling in a molecular 4f qubit

Jonathan Marbey[a,b,†], Jon G. C. Kragskow[c,†], Christian D. Buch,[d] Joscha Nehrkorn[a], Mykhaylo Ozerov[a], Stergios Piligkos[d,*], Stephen Hill[a,b,*] and Nicholas F. Chilton[c,*]

[a] National High Magnetic Field Laboratory, Tallahassee, Florida, 32310, United States of America

[b] Department of Physics, Florida State University, Tallahassee, Florida, 32306, United States of America

[c] Department of Chemistry, School of Natural Sciences, University of Manchester, Oxford Road, Manchester, M13 9PL, United Kingdom

[d] Department of Chemistry, University of Copenhagen, DK-2100 Copenhagen, Denmark

[†] These two authors contributed equally to this work.

Email: piligkos@chem.ku.dk; shill@magnet.fsu.edu; nicholas.chilton@manchester.ac.uk

Contents

Experimental electronic structure 2
Ab initio electronic structure and vibrational modes 3
Model Hamiltonian 12
Ab initio vibronic coupling and simulation of FIRMS maps 15
Experimental and theoretical FIRMS maps and analysis 23
References 34

Experimental electronic structure

Table S1: CFPs obtained from fits to the experimental emission spectrum of **1**.[1]

CFP	**Experiment (cm^{-1})**
B_2^0	-11.13(7)
B_4^{-3}	0
B_4^0	0.153(3)
B_4^3	8.92(4)
B_6^{-6}	0.101(7)
B_6^{-3}	0.07(3)
B_0^6	0.0071(2)
B_3^6	-0.060(3)
B_6^6	0.034(2)

Table S2: Doublets of J = 7/2 multiplet of **1**: CF energies from experiment, from parameterised model of experiment (main text Equation 1), and principal g-values and compositions of CF wave functions of model in terms of pure $¿ J, m_J \rangle$ states.

Observed energy (cm^{-1})	**Model CF energies (cm^{-1})**	$g_{\perp}$	$g_{¿\vee¿¿}$	**CF wave function composition**	$\langle \hat{J}_z \rangle$
0	0	2.95	4.33	58.333% |±7/2⟩ + 29.778% |±1/2⟩ + 11.889% |∓5/2⟩	±1.895
474	464.2	2.39	0.30	52.305% |±5/2⟩ + 31.374% |∓7/2⟩ + 16.321% |∓1/2⟩	±0.130
745	736.6	0.00	3.43	100% |±3/2⟩	±1.500
920	912.7	3.62	0.61	53.901% |∓1/2⟩ + 35.806% |±5/2⟩ + 10.293% |∓7/2⟩	±0.256

Ab initio electronic structure and vibrational modes

Table S3: CASSCF-XMS-CASPT2-SO results for the $^2F_{7/2}$ ground term of **1** calculated using the x-ray crystallographic structure.

Energy (cm^{-1})	$g_{\perp}$	$g_{¿\vee¿¿}$	**CF wave function composition**	$\langle \hat{J}_z \rangle$
0.0	2.80	4.68	66.603 % |±7/2⟩ + 18.610 % |±1/2⟩ + 14.788 % |∓5/2⟩	±2.054
418.1	2.36	3.11	81.122 % |±5/2⟩ + 18.842 % |∓7/2⟩ + 0.036 % |∓1/2⟩	±1.368
731.8	0.00	3.38	100 % |±3/2⟩	±1.500
915.2	1.87	4.16	81.355 % |±1/2⟩ + 14.555 % |±7/2⟩ + 4.090 % |∓5/2⟩	±0.814

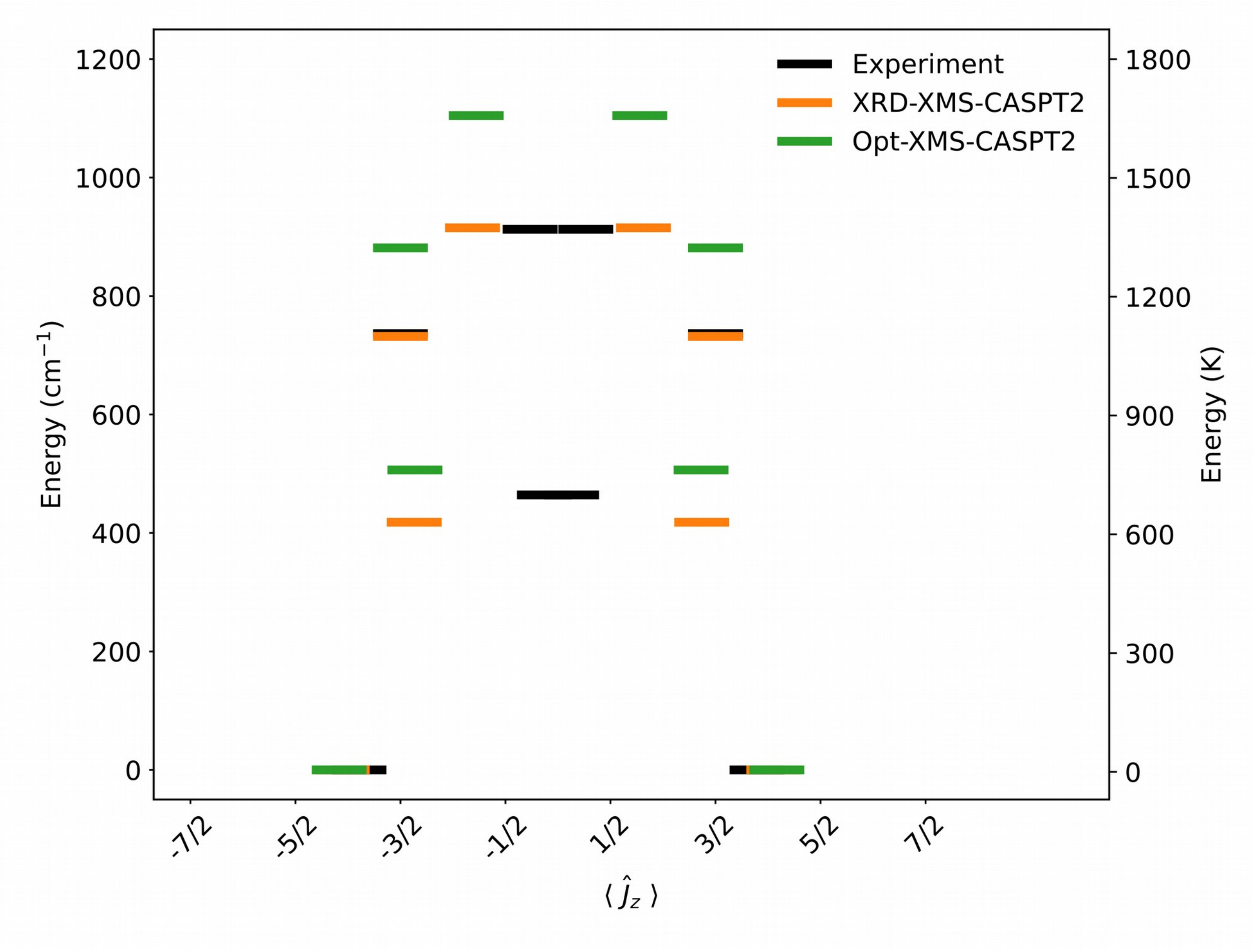

Figure S1: Energies and $\langle \hat{J}_z \rangle$ expectation values of the $^2F_{7/2}$ states of **1** obtained from the experimental CFPs in Table S2 (black), the CASSCF-XMS-CASPT2-SO CFPs for the X-Ray (XRD) crystallographic structure in Table S3 (orange), and the CASSCF-XMS-CASPT2-SO CFPs for the optimised (Opt) structure in Table S6 (green).

Table S4: Coordinates of $\mathbf{1}_{\mathbf{opt}}$ calculated with DFT using the PBE0 functional, see Methods.

Atom	**x (Å)**	**y (Å)**	**z (Å)**
Yb	0.000000	0.000000	0.167551
N	0.000000	0.000000	2.969546
N	-0.679435	2.087931	1.147990
O	-1.738881	0.577725	-0.934359
O	0.369116	-1.794778	-0.934359
O	1.369765	1.217053	-0.934359
C	0.000000	2.392490	2.390990
H	1.091101	2.352570	2.223290
H	-0.243583	3.402480	2.768283
C	-2.445422	1.618309	-1.218309
C	-3.362648	1.594206	-2.301797
H	-3.428500	0.668061	-2.875191
C	-4.127953	2.697898	-2.620804
H	-4.817380	2.642871	-3.467543

C	-4.038677	3.891285	-1.878245
H	-4.649999	4.755585	-2.140554
C	-3.164966	3.941601	-0.812501
H	-3.080837	4.855275	-0.215902
C	-2.359906	2.834241	-0.462058
C	-1.508764	2.963054	0.684773
H	-1.603744	3.923607	1.224104
C	-0.407810	1.342300	3.413145
H	0.001879	1.571607	4.415725
H	-1.504741	1.364693	3.497102
C	-2.071957	-1.196245	2.390990
H	-2.582936	-0.231364	2.223290
H	-2.824842	-1.912189	2.768283
N	-1.468484	-1.632373	1.147990
C	-1.350613	-5.443239	-1.878245
H	-1.793458	-6.404809	-2.140554
C	-1.831044	-4.711741	-0.812501
H	-2.664373	-5.095720	-0.215902
C	-1.274572	-3.460858	-0.462058
C	-1.811698	-2.788155	0.684773
H	-2.596071	-3.350686	1.224104
C	-0.958561	-1.024323	3.413145
H	-1.361991	-0.784176	4.415725
H	-0.429489	-1.985491	3.497102
C	-0.178785	-2.926952	-1.218309
C	0.300701	-3.709241	-2.301797
H	1.135692	-3.303199	-2.875191
C	-0.272472	-4.923861	-2.620804
H	0.119896	-5.493409	-3.467543
C	2.071957	-1.196245	2.390990
H	1.491835	-2.121206	2.223290
H	3.068425	-1.490291	2.768283
N	2.147919	-0.455558	1.147990
C	5.389290	1.551954	-1.878245
H	6.443457	1.649225	-2.140554
C	4.996010	0.770140	-0.812501
H	5.745210	0.240445	-0.215902
C	3.634477	0.626618	-0.462058
C	3.320462	-0.174899	0.684773
H	4.199815	-0.572920	1.224104
C	1.366371	-0.317976	3.413145
H	1.360112	-0.787430	4.415725
H	1.934230	0.620797	3.497102
C	2.624208	1.308643	-1.218309
C	3.061947	2.115036	-2.301797
H	2.292808	2.635137	-2.875191
C	4.400425	2.225963	-2.620804

Table S5: Vibrational mode numbers (*j*), irreducible representations (Mulliken Symbols), energies, transition intensities, and vibronic coupling strength (S_j) of the vibrational modes of $\mathbf{1}_{\mathrm{opt}}$. Vibrational modes observed in the main region of the FIRMS map, and discussed in the

main text, are highlighted. Note that C_3 is an Abelian group, hence the E representation is not strictly irreducible, but we still refer to it as such.

Mode Number (*j*)	**IRREP**	**Energy (cm^{-1})**	**Transition Intensity (km mol^{-1})**	S_j**(cm^{-1})**	**Mode Number (*j*)**	**IRREP**	**Energy (cm^{-1})**	**Transition Intensity (km mol^{-1})**	S_j**(cm^{-1})**
1	E	17.049	0.270	0.5784	91	A	1058.866	2.934	0.0133
2	E	17.049	0.270	0.5783	92	E	1070.501	22.695	0.1729
3	A	21.963	0.022	0.9727	93	E	1070.501	22.696	0.1735
4	E	48.448	0.401	0.8361	94	A	1092.938	1.535	0.1190
5	E	48.449	0.401	0.8364	95	E	1112.483	23.902	0.3673
6	A	61.248	0.002	0.7790	96	E	1112.483	23.901	0.3687
7	E	98.981	1.759	2.0336	97	A	1118.476	18.408	0.3589
8	E	98.981	1.759	2.0337	98	E	1150.153	16.466	0.1277
9	A	102.101	5.546	1.1577	99	E	1150.153	16.466	0.1270
10	A	105.188	2.419	1.0192	100	A	1151.537	3.958	0.1067
11	E	121.533	1.798	1.2315	101	E	1164.854	7.382	0.2312
12	E	121.534	1.798	1.2313	102	E	1164.854	7.382	0.2319
13	A	143.349	0.277	1.4245	103	A	1165.943	37.694	0.0009
14	E	168.810	2.013	1.7976	104	E	1173.738	20.455	0.0523
15	E	168.811	2.013	1.7966	105	E	1173.738	20.454	0.0522
16	A	194.872	1.063	0.5942	106	A	1223.420	1.307	0.0514
17	E	201.390	2.894	1.1321	107	E	1242.242	28.568	0.2618
18	E	201.390	2.893	1.1328	108	E	1242.242	28.569	0.2618
19	A	206.609	5.651	0.5993	109	A	1246.953	78.896	0.0843
20	E	207.233	26.085	1.5501	110	E	1259.564	12.173	0.2604
21	E	207.234	26.086	1.5500	111	E	1259.564	12.175	0.2612
22	E	243.421	10.605	1.6166	112	A	1265.640	47.647	0.0956
23	E	243.421	10.605	1.6162	113	E	1266.950	15.140	0.1743
24	A	243.713	4.543	0.9215	114	E	1266.950	15.139	0.1733
25	A	302.226	4.527	0.6096	115	A	1301.195	22.197	0.0642
26	E	304.782	19.765	1.7560	116	E	1304.526	15.162	0.0751
27	E	304.782	19.765	1.7559	117	E	1304.526	15.164	0.0739
28	A	339.877	0.054	0.5997	118	E	1348.067	14.481	0.1939
29	E	354.097	2.821	0.3409	119	E	1348.067	14.482	0.1928
30	E	354.097	2.821	0.3412	120	A	1356.417	50.598	0.1777
31	A	363.366	3.945	0.8388	121	E	1390.003	77.962	0.8485
32	E	376.891	26.744	0.8078	122	E	1390.003	77.962	0.8491
33	E	376.891	26.745	0.8083	123	A	1393.668	0.311	0.0563
34	A	405.921	13.149	1.0986	124	E	1397.156	39.141	0.3223
35	E	413.150	26.322	2.0820	125	E	1397.156	39.143	0.3222
36	E	413.150	26.321	2.0819	126	A	1398.842	0.516	0.0877
37	A	444.750	0.285	0.7163	127	A	1407.342	0.095	0.0415
38	E	445.645	2.370	0.6812	128	E	1407.378	45.776	0.1315
39	E	445.645	2.371	0.6814	129	E	1407.378	45.775	0.1320
40	A	472.671	16.744	0.1132	130	E	1428.371	31.732	0.1097
41	E	477.090	0.993	0.2042	131	E	1428.371	31.732	0.1096
42	E	477.091	0.992	0.2043	132	A	1429.216	13.744	0.0194
43	A	516.190	7.281	0.1331	133	E	1456.936	10.928	0.1052
44	E	520.657	1.425	1.2191	134	E	1456.936	10.927	0.1058
45	E	520.657	1.425	1.2188	135	A	1457.860	41.731	0.0868
46	A	563.246	0.060	0.1763	136	E	1466.478	10.459	0.1195
47	E	564.025	0.152	0.4047	137	E	1466.478	10.460	0.1190
48	E	564.025	0.152	0.4043	138	A	1471.148	6.904	0.0864
49	E	582.008	9.752	0.8632	139	E	1506.969	16.695	0.3406
50	E	582.008	9.752	0.8629	140	E	1506.969	16.695	0.3406
51	A	586.006	5.708	0.2807	141	A	1507.485	14.102	0.0939
52	E	603.156	39.954	0.8351	142	E	1526.602	433.168	2.5730
53	E	603.156	39.953	0.8341	143	E	1526.602	433.180	2.5726
54	A	605.684	1.054	0.0852	144	A	1536.935	161.499	0.1202
55	E	652.681	10.203	0.6646	145	E	1602.423	110.761	0.7195
56	E	652.681	10.203	0.6648	146	E	1602.423	110.758	0.7188

57	A	653.219	14.113	0.3339	147	A	1603.415	240.739	0.0546
58	E	762.003	30.225	0.0255	148	E	1679.672	5.520	1.1414
59	E	762.003	30.226	0.0256	149	E	1679.672	5.521	1.1413
60	A	762.023	36.891	0.0508	150	A	1680.433	6.621	0.0187
61	A	767.926	7.513	0.5468	151	E	1701.208	933.492	0.7574
62	A	785.476	15.297	0.1128	152	E	1701.208	933.489	0.7564
63	E	785.570	14.472	0.1616	153	A	1716.376	597.625	0.0705
64	E	785.570	14.472	0.1617	154	E	3011.772	3.033	0.0314
65	E	821.184	23.449	0.7419	155	E	3011.772	3.032	0.0315
66	E	821.184	23.450	0.7417	156	A	3014.678	23.269	0.0776
67	A	831.122	0.027	0.1395	157	E	3025.158	45.235	0.0795
68	E	884.926	16.338	0.0916	158	E	3025.158	45.231	0.0787
69	E	884.926	16.338	0.0918	159	A	3028.039	188.955	0.0461
70	A	885.703	9.753	0.0727	160	E	3047.653	51.683	0.1173
71	E	888.620	4.982	0.3671	161	E	3047.653	51.683	0.1150
72	E	888.620	4.981	0.3663	162	A	3048.113	42.433	0.0322
73	E	912.529	46.795	0.5478	163	E	3076.895	28.874	0.0597
74	E	912.529	46.797	0.5479	164	E	3076.895	28.871	0.0592
75	A	916.245	3.304	0.0813	165	A	3077.141	13.919	0.0207
76	A	931.696	25.770	0.1425	166	A	3110.499	1.940	0.0231
77	E	953.927	0.723	0.0385	167	E	3116.819	32.695	0.0308
78	E	953.928	0.723	0.0383	168	E	3116.819	32.699	0.0310
79	A	954.069	0.470	0.0170	169	E	3179.543	13.829	0.0188
80	E	961.663	0.187	0.1682	170	E	3179.543	13.828	0.0179
81	E	961.663	0.187	0.1691	171	A	3179.593	5.148	0.0038
82	E	1001.401	0.256	0.0082	172	E	3195.542	6.700	0.0148
83	E	1001.401	0.256	0.0083	173	E	3195.542	6.701	0.0149
84	A	1001.447	0.204	0.0041	174	A	3195.574	19.944	0.0006
85	A	1010.930	5.017	0.0154	175	E	3225.252	17.020	0.0050
86	E	1012.553	1.503	0.1104	176	E	3225.252	17.019	0.0045
87	E	1012.553	1.503	0.1106	177	A	3225.287	2.224	0.0029
88	A	1041.994	13.635	0.0544	178	E	3231.521	15.861	0.0144
89	E	1057.492	16.170	0.0673	179	E	3231.521	15.862	0.0143
90	E	1057.492	16.171	0.0673	180	A	3231.581	12.413	0.0075

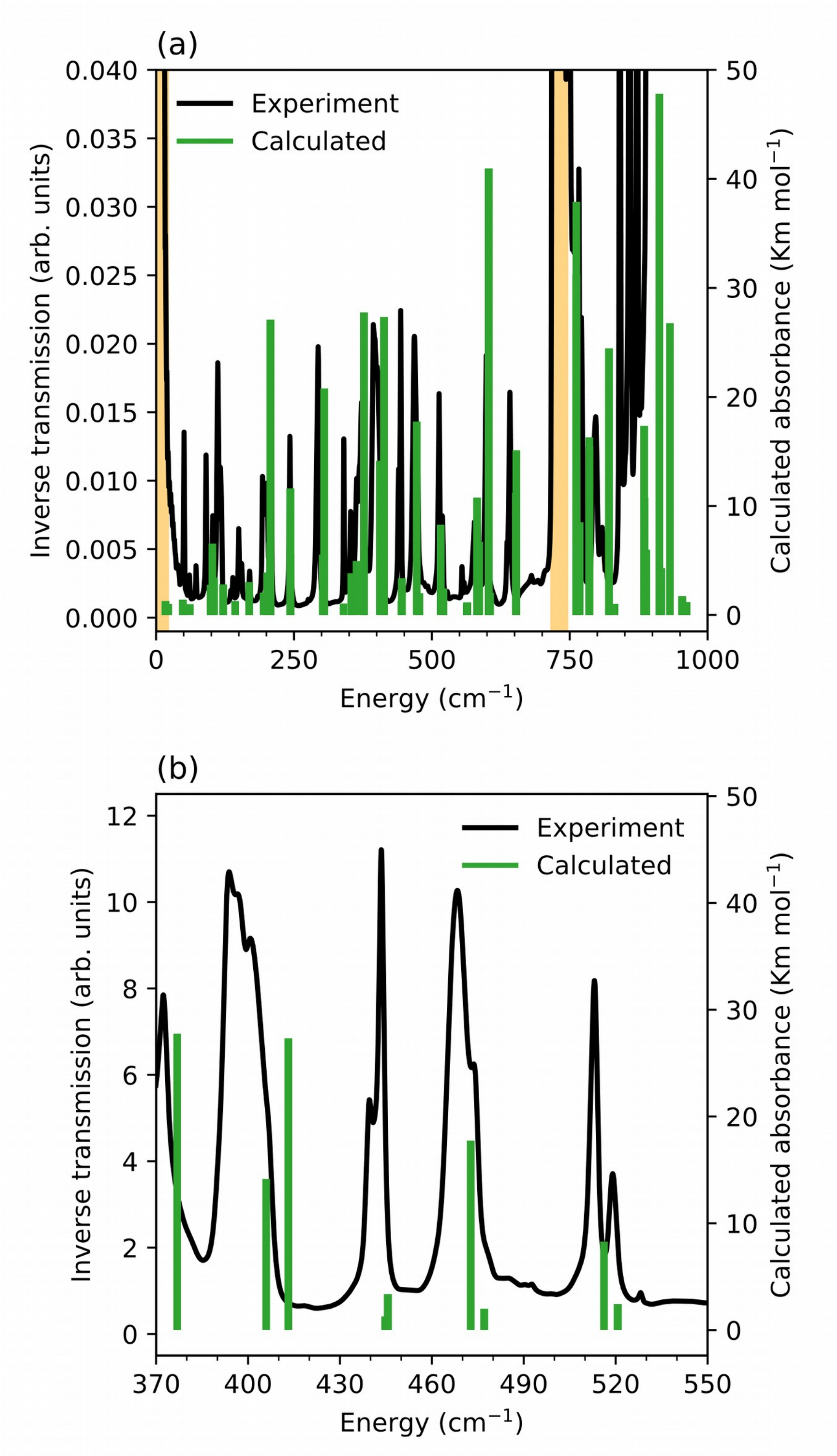

Figure S2: (a) Experimental zero-field FTIR spectrum (black line) and *ab initio* DFT calculated infrared energies and intensities (green lines) in the range 0 – 1000 cm^{-1}. Experimental spectra are plotted as the inverse of the transmission to highlight strong vibrational modes and in (a) have been scaled by 0.002 for readability. Artifacts at 0 and ~720 cm^{-1} (shaded regions) are caused by instrumental “blind spots” where the transmission is near zero because of destructive interference in the beam splitter employed in the FTIR

spectrometer (b) Experimental zero-field FTIR spectrum (black line) and *ab initio* DFT calculated infrared energies and intensities (green lines) in the range 370 – 550 cm^{-1}.

Table S6: CASSCF-XMS-CASPT2-SO results for the $^2F_{7/2}$ ground term of **1$_{\mathbf{opt}}$**.

Energy (cm^{-1})	$g_\perp$	$g_{¿\vee¿¿}$	**CF wave function composition**	$\langle \hat{J}_z \rangle$
0.0	2.77	4.75	68.097% |±7/2⟩ + 16.598 %|±1/2⟩ + 15.305 % |∓5/2⟩	±2.084
506.4	2.36	3.09	81.026 % |±5/2⟩ + 18.940 % |∓7/2⟩ + 0.034 % |∓1/2⟩	±1.363
881.3	0.00	3.37	100% |±3/2⟩	±1.500
1104.7	4.20	1.79	83.368 % |±1/2⟩ + 12.963 % |±7/2⟩ + 3.670 % |∓5/2⟩	±0.779

Table S7: CASSCF-SO results for the $^2F_{7/2}$ ground term of **1$_{\mathbf{opt}}$**.

Energy (cm^{-1})	$g_\perp$	$g_{¿\vee¿¿}$	**CF wave function composition**	$\langle \hat{J}_z \rangle$
0.0	2.40	5.55	74.792 % |±7/2⟩ + 14.848 % |±1/2⟩ + 10.360 % |∓5/2⟩	±2.433
320.0	2.09	3.69	85.098 % |±5/2⟩ + 14.290 % |∓7/2⟩ + 0.613 % |±1/2⟩	±1.624
607.0	0.00	3.39	100 % |±3/2⟩	±1.500
723.2	4.28	1.59	84.539 % |±1/2⟩ + 10.919 % |±7/2⟩ + 4.542 % |∓5/2⟩	±0.691

Table S8: CFPs obtained from *ab initio* calculations on XRD and DFT-optimised geometries of **1**.

CFP	**1**$_{XRD}$ **CASSCF-XMS-CASPT2-SO (cm^{-1})**	**1**$_{opt}$ **CASSCF-SO (cm^{-1})**	**1**$_{opt}$ **CASSCF-XMS-CASPT2-SO (cm^{-1})**
B_2^{-2}	-0.00014	0.00000	0.00026
B_2^{-1}	0.00083	-0.00001	0.00040
B_2^{0}	-16.10461	-14.72160	-20.33683
B_2^{1}	0.00065	0.00001	0.00006
B_2^{2}	0.00077	0.00003	-0.00041
B_4^{-4}	0.00032	0.00000	0.00004
B_4^{-3}	7.19417	-4.67006	3.88208
B_4^{-2}	0.00002	0.00000	-0.00001
B_4^{-1}	-0.00006	0.00000	-0.00001
B_4^{0}	0.05925	0.03273	0.07897
B_4^{1}	-0.00003	0.00000	-0.00002
B_4^{2}	-0.00009	0.00000	0.00004
B_4^{3}	3.19595	-3.29563	-8.21874
B_4^{4}	-0.00026	0.00000	-0.00008
B_6^{-6}	0.07202	0.06120	-0.10246
B_6^{-5}	-0.00001	0.00000	0.00000
B_6^{-4}	-0.00002	0.00000	0.00000
B_6^{-3}	0.08742	-0.05066	0.04386
B_6^{-2}	0.00000	0.00000	0.00000
B_6^{-1}	0.00000	0.00000	0.00000
B_6^{0}	0.00716	0.00599	0.00788
B_6^{1}	0.00000	0.00000	0.00000
B_6^{2}	0.00000	0.00000	0.00000
B_6^{3}	0.27517	-0.03502	-0.09423
B_6^{4}	0.00001	0.00000	0.00000
B_6^{5}	0.00000	0.00000	0.00000
B_6^{6}	-0.06574	-0.01788	0.07732

Model Hamiltonian

Calculating the populations of the lowest four states ¿ and ¿ as a function of magnetic field and vibrational mode energy reveals that, in the limit of $\hbar\omega \rightarrow 0$ and $B=0$, all four states have equal population (Figure S3a), but as the field strength is increased around 5 T ($\delta=$¿5 cm^{-1}), ¿ and ¿ each have 50% population (Figure S3b). Therefore, hot bands originating from excited electronic states will only be present at low fields ($B<$ 5 T), irrespective of the vibrational mode energy. Alternatively, when the energy of the coupled vibrational mode increases above *ca.* 20 cm^{-1}, ¿ and ¿ each have 50% population in zero field (Figure S3a), but when the field strength is increased to around 5 T, ¿ approaches 100% population (Figure S3b). Therefore, hot bands originating from an excited vibrational state will only be observable for low-energy vibrational modes ($\hbar\omega$ < 20 cm^{-1}).

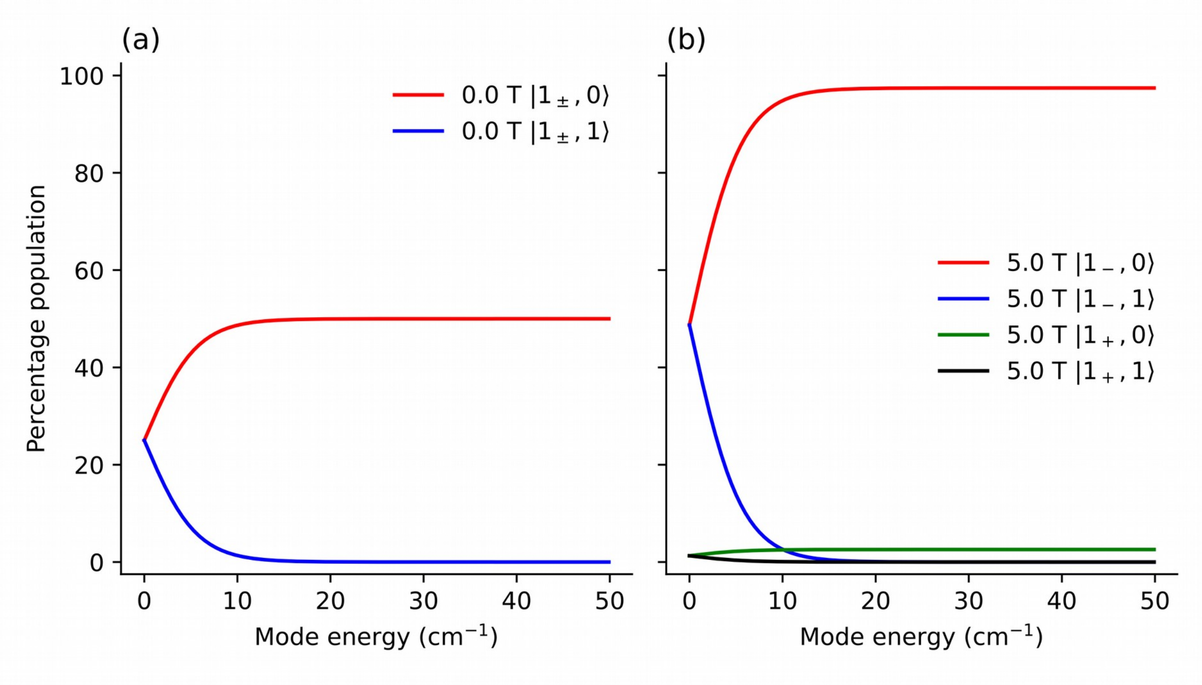

Figure S3: Populations of the lowest four states of the simple vibronic model as a function of vibrational mode energy at 4.2 K in (a) zero applied magnetic field, (b) a 5 T magnetic field applied along the z axis.

The transition matrix elements due to the IR radiation between electronic states are herein defined as A_e and those between vibrational states as A_v. In the direct product basis ¿ the matrix form of the total transition moment, d_T, is:

$$d_T=\begin{bmatrix} 0 & A_v & A_e & 0 & A_e & 0 & A_e & 0 \\ A_v & 0 & 0 & A_e & 0 & A_e & 0 & A_e \\ A_e & 0 & 0 & A_v & A_e & 0 & A_e & 0 \\ 0 & A_e & A_v & 0 & 0 & A_e & 0 & A_e \\ A_e & 0 & A_e & 0 & 0 & A_v & A_e & 0 \\ 0 & A_e & 0 & A_e & A_v & 0 & 0 & A_e \\ A_e & 0 & A_e & 0 & A_e & 0 & 0 & A_v \\ 0 & A_e & 0 & A_e & 0 & A_e & A_v & 0 \end{bmatrix} \qquad \text{S1}$$

The vibronic coupling Hamiltonian $\hat{H}_1$ is defined as below, as the direct product between the electronic and vibrational parts, where we have omitted the factor of $1/\sqrt{2}$ in the latter for simplicity (see Equation S13). Diagonal terms G express energy shifts and off-diagonal terms F describe coupling between different electronic states.

$$\hat{H}_1=\begin{bmatrix} G & F & F & F \\ F & G & F & F \\ F & F & G & F \\ F & F & F & G \end{bmatrix} \otimes \begin{bmatrix} 0 & 1 \\ 1 & 0 \end{bmatrix} = \begin{bmatrix} 0 & G & 0 & F & 0 & F & 0 & F \\ G & 0 & F & 0 & F & 0 & F & 0 \\ 0 & F & 0 & G & 0 & F & 0 & F \\ F & 0 & G & 0 & F & 0 & F & 0 \\ 0 & F & 0 & F & 0 & G & 0 & F \\ F & 0 & F & 0 & G & 0 & F & 0 \\ 0 & F & 0 & F & 0 & F & 0 & G \\ F & 0 & F & 0 & F & 0 & G & 0 \end{bmatrix} \qquad \text{S2}$$

Perturbation theory allows us to determine the first-order corrected eigenstates of $\hat{H}_0+\hat{H}_1$ (Equation 1 plus Equation 2), yielding the un-normalised column eigenvectors below.

¿

S3

Transition probabilities for the cold intra-KD excitations are given in the main text (Equation 3). Transition probabilities for cold inter-KD vibronic excitations (absorption of an IR photon with $h\upsilon=\Delta+\hbar\omega$ and $h\upsilon=2\delta+\Delta+\hbar\omega$), under the approximations $\hbar\omega\ll\Delta$ and $\delta\ll\Delta$, are given below; these expressions diverge when $\delta\rightarrow 0$ and/or $\hbar\omega\rightarrow 0$ (*i.e.* in proximity to the purely electronic inter-KD transitions).

I¿ S4

I¿ S5

Ab initio vibronic coupling and simulation of FIRMS maps

When constructing the total *ab initio* vibronic coupling Hamiltonian, $\widehat{H}_T$ (Equation 4), the electronic Hamiltonians in the ¿$m_J\rangle$ basis ($\widehat{H}_{CF}+\widehat{H}_{Zee}$) can be transformed into the direct product basis ¿$m_J, n_1, n_2, \ldots\rangle$ by taking the Kronecker product with an identity matrix the size of the vibrational basis ($\left(n_{max}+1\right)^{n_{vib}}$, where n_{max} is the maximum number of vibrational quanta considered, herein $n_{max}=1$, and n_{vib} is the number of vibrational modes considered). Likewise, each vibrational matrix ($\widehat{H}_{vib,j}$, constructed in its own vibrational basis) can be transformed into the direct product basis by taking the Kronecker product with an identity matrix the size of the electronic basis ($2J+1=8$) and for each of the other vibrational modes, taking careful consideration of the ordering of the basis; this is summarised in Equation S8.

Assuming the weak-coupling limit where vibrational modes are unaffected by coupling to electronic states, any matrix element of $\widehat{H}_{coup,j}$ for a single mode j in the direct product basis is then:

$$\left\langle m_J', n_j \pm 1 \left| \widehat{H}_{coup,j} \right| m_J, n_j \right\rangle = \left\langle m_J', n_j \pm 1 \left| \sum_{k=2,4,6} \sum_{q=-k}^{k} \widehat{Q}_j \left(\frac{\partial B_k^q}{\partial Q_j} \right)_{eq} \widehat{O}_k^q \right| m_J, n_j \right\rangle \qquad \text{S6}$$

We calculate the electronic and nuclear parts of this expression as $\left\langle m_J' \left| \sum_{k=2,4,6} \sum_{q=-k,k} \left(\frac{\partial B_k^q}{\partial Q_j} \right)_{eq} \widehat{O}_k^q \right| m_J \right\rangle$ and $\left\langle n_j \pm 1 \left| \widehat{Q}_j \right| n_j \right\rangle$, and denote their matrix representations as $\widehat{H}_{coup-e,j}$ and $\widehat{H}_{coup-v,j}$, respectively. These two matrices can be used to obtain the matrix representation of $\widehat{H}_{coup,j}$ through the Kronecker product (note that this is in the basis where only a single vibrational mode is considered; the more general expression is encapsulated in Equation S8):

$$\widehat{H}_{coup,j} = \widehat{H}_{coup-e,j} \otimes \widehat{H}_{coup-v,j} \qquad \text{S7}$$

$$\widehat{H}_T = \left(\widehat{H}_{Zee} + \widehat{H}_{CF} \right) \otimes I_{vib,1} \otimes I_{vib,2} \otimes \ldots + I_{elec} \otimes \widehat{H}_{vib,1} \otimes I_{vib,2} \otimes \ldots + \widehat{H}_{coup-e,1} \otimes \qquad \text{S8}$$

Note that in practice we transform $\widehat{H}_{Zee}$ and $\widehat{H}_{coup-e,j}$ into the eigenbasis of $\widehat{H}_{CF}$, which allows us to correct the CF eigenvalues of our *ab initio* CASSCF-XMS-CASPT2-SO to match experiment.

To obtain $\left(\partial B_k^q / \partial Q_j\right)_{eq}$ for each vibrational mode in Equation S6, we distort the molecular geometry along the normal mode coordinate up to the zero-point displacement (ZPD) and calculate the electronic structure with CASSCF-SO (differences in CFPs are taken from the electronic states calculated at equilibrium using CASSCF-SO, Table S7). Assuming the harmonic approximation for each vibrational mode, we calculate the thermal population of excited states using the Boltzmann distribution and thus determine the thermally averaged displacement for each mode at 4 K and displace the molecule up to ±1.5× the zero-point displacement (ZPD) for all modes; this ensures that we are in the interpolation regime at low temperatures. We define the ZPD of a given mode j as

$$Q_{j,ZPD} = \sqrt{\frac{\hbar}{\omega_j \mu_j}} \qquad \text{S9}$$

where μ_j is the reduced mass of mode j. We calculate the electronic structure with CASSCF-SO at 4 evenly spaced points in both positive and negative directions, and then fit the changes in the crystal field parameters (compared to those calculated at the equilibrium geometry using CASSCF-SO) to cubic polynomials (Equation S10, Figure S4). The first derivative of each B_k^q at $Q_{eq}=0$ is then simply the linear coefficient: $\left(\frac{\partial B_k^q}{\partial Q_j}\right)_{eq} = c$.

$$B_k^q(Q_j) = a Q_j^3 + b Q_j^2 + c Q_j + B_k^q(Q_{eq}) \qquad \text{S10}$$

The vibrational part of Equation S6 is evaluated as

$$\langle n_j - 1 | \widehat{Q}_j | n_j \rangle = \frac{1}{\sqrt{2}} \langle n_j - 1 | \hat{a} | n_j \rangle = \sqrt{\frac{n_j}{2}} \qquad \text{S11}$$

$$\langle n_j + 1 | \widehat{Q}_j | n_j \rangle = \frac{1}{\sqrt{2}} \langle n_j + 1 | \hat{a}^\dagger | n_j \rangle = \sqrt{\frac{n_j + 1}{2}} \qquad \text{S12}$$

As we restrict ourselves to the $n_j = 0$ and $n_j = 1$ basis, the vibrational part becomes:

$$\widehat{H}_{coup-v,j} = \begin{bmatrix} 0 & \frac{1}{\sqrt{2}} \\ \frac{1}{\sqrt{2}} & 0 \end{bmatrix} \qquad \text{S13}$$

Ab initio calculation of vibronic transition intensities is extremely challenging, stemming from not only the calculation of accurate vibrational transition intensities, but also because highly accurate vibronic coupling and electronic structure calculations are needed. In this work we consider only gas-phase vibrational modes, thus there is no representation of the molecular environment, and hence our vibrational transition intensities are already inaccurate compared to the experimental FTIR spectrum (Figure S2, though note the vibrational energies are predicted very well). Therefore, here we use simple selection rules to define relative transition intensities. The intensity, I_{if}, of a transition between two states i and f is proportional to the product of the square of the transition matrix element $\left|\langle i | d_T' | f \rangle\right|^2$ (see below for definition of d_T') and the Boltzmann population of the initial state p_i, which here we convolute with an empirical Gaussian linewidth function $g(\Delta E_{fi})$ with standard deviation of 2 cm^{-1}: $I_{if} \propto p_i \left|\langle i | d_T' | f \rangle\right|^2 g(\Delta E_{fi})$. We write the matrix representation of the total transition moment in the direct product basis as the sum of the transition moments for the purely electronic (d_e) and purely vibrational (d_v) modes:

$$d_T = d_e \otimes I_{vib} + I_{elec} \otimes d_v \qquad \text{S14}$$

We define the vibrational selection rule as:

$$\langle n_j' | d_v | n_j \rangle = \begin{cases} 1\, if\; n_j' = n_j \pm 1 \\ 0\, else \end{cases} \qquad \text{S15}$$

and the electronic selection rule as:

$$\langle m_J' | d_e | m_J \rangle = \begin{cases} 100\, if\; m_J' = m_J \pm 1 \vee m_J' = m_J \\ 0\, else \end{cases} \qquad \text{S16}$$

We have found that in order to match the experimental FIRMS map, we must increase the relative intensity of the electronic transition intensity (hence 100 *vs.* 1 above), and also apply a “mask” to the transitions between the eigenstates of $\widehat{H}_T$ to supress the purely vibrational and purely electronic transitions (we also suppress combination bands in which more than one vibrational quantum is exchanged, which are relevant when more than one vibrational mode is included in $\widehat{H}_T$). This mask is required because the simulated maps are “perfect” and so slight vibronic mixing into pure vibrational bands make these features dominant in the spectra, but they are invisible in experiment due to significant vibrational linewidths and experimental drift across the different FTIR spectra (which, when averaged, obscures these vibrational features). We define our mask M in the direct product basis in the case of a single vibrational mode as:

$$\langle m_J', n_j' | M | m_J, n_j \rangle = \begin{cases} 1\, if\; n_j' = n_j \pm 1 \wedge m_J' = m_J \pm 1 \\ 0\, else \end{cases} \qquad \text{S17}$$

and in the case of multiple modes as:

$$\langle m_J', n_1', n_2', \ldots | M | m_J, n_1, n_2, \ldots \rangle = \begin{cases} 1\, if\; n_j' = n_j \pm 1, m_J' = m_J \pm 1, \wedge n_k' = n_k\, for\, all\, k \\ 0\, else \end{cases} \qquad \text{S18}$$

We then transform the matrix representations of M and d_T into the eigenbasis of $\widehat{H}_T$, and apply the former to the latter element-wise (Hadamard product), where U is the matrix of eigenvector coefficients that diagonalises $\widehat{H}_T$.

$$d_T{}' = U^{-1} d_T U \circ U^{-1} M U \qquad \text{S19}$$

In applying this mask, we note that the absolute values of normalised absorbance seen on our simulated spectra should only be taken as a guide and should not be compared directly with the experimental values. As our FIRMS experiments are performed for powder samples, we must also integrate over the orientation of the external magnetic field in $\widehat{H}_{Zee}$; here we use the Zaremba-Conroy-Wolfberg (ZCW) model with an integration level of 5 (233 directions evenly distributed on a hemisphere) for all of our simulations other than those involving 9 modes, wherein we use a level of 3 (89 directions) in order to speed up our simulation considerably.[4]

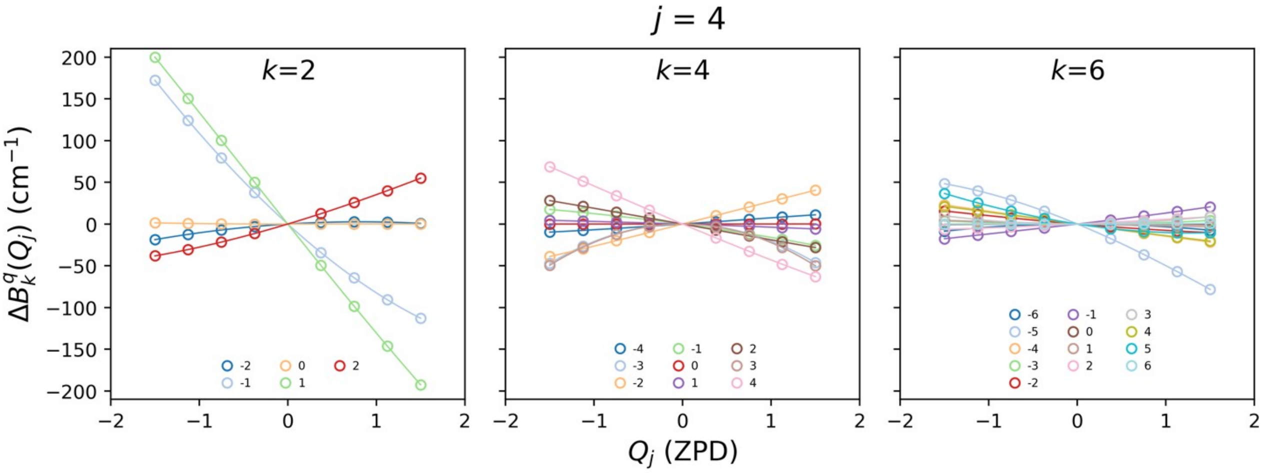
j = 4
k=2
k=4
k=6
ΔB_k^q(Q_j) (cm⁻¹)
Q_j (ZPD)
200
150
100
50
0
−50
−100
−150
−200
−2
−1
0
1
2
-2
-1
0
1
2
-4
-3
-2
-1
0
1
2
3
4
-6
-5
-4
-3
-2
-1
0
1
2
3
4
5
6

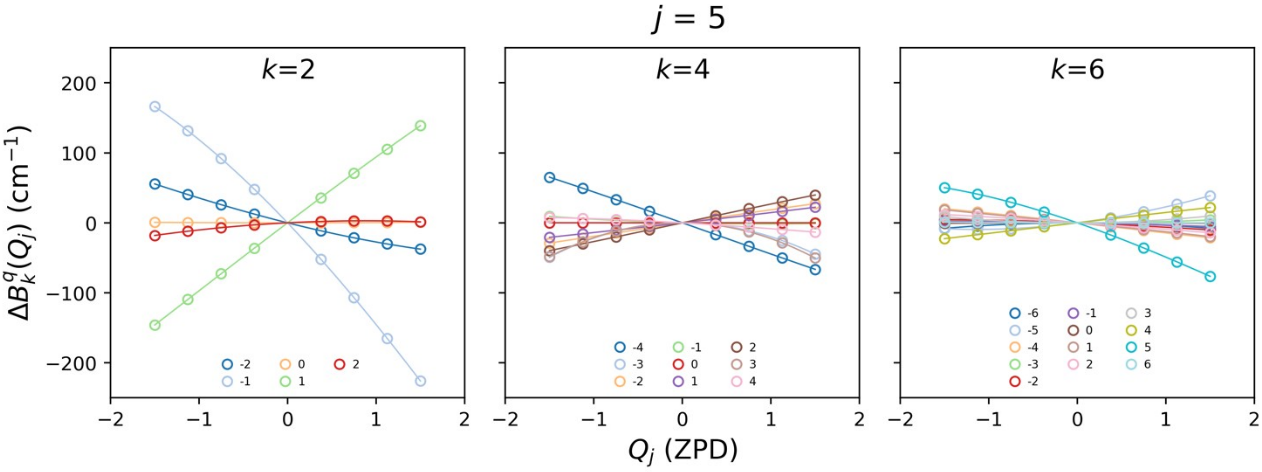
j = 5
k=2
k=4
k=6
ΔB_k^q(Q_j) (cm⁻¹)
Q_j (ZPD)
200
100
0
−100
−200
−2
−1
0
1
2
-2
-1
0
1
2
-4
-3
-2
-1
0
1
2
3
4
-6
-5
-4
-3
-2
-1
0
1
2
3
4
5
6

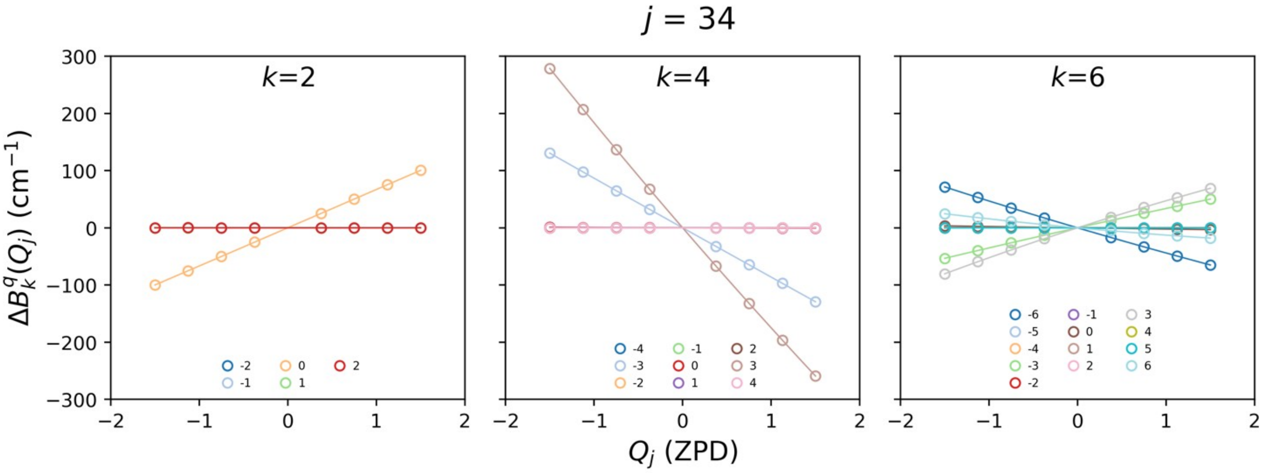

j = 34
k=2
k=4
k=6
$\Delta B_k^q(Q_j)$ (cm^{-1})
Q_j (ZPD)
300
200
100
0
−100
−200
−300
−2
−1
0
1
2
-2 -1 0 1 2
-4 -3 -2 -1 0 1 2 3 4
-6 -5 -4 -3 -2 -1 0 1 2 3 4 5 6

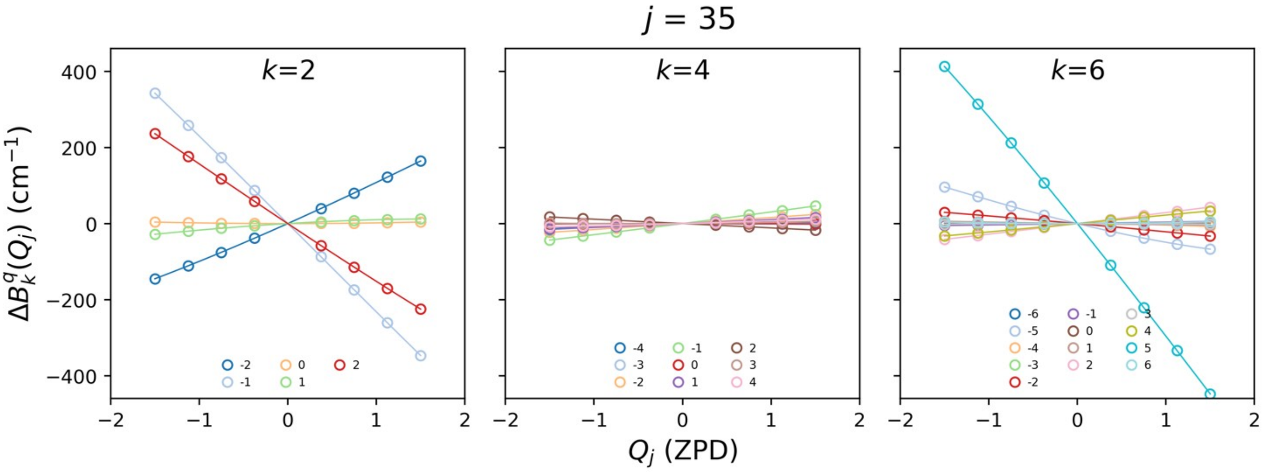

j = 35
k=2
k=4
k=6
$\Delta B_k^q(Q_j)$ (cm^{-1})
Q_j (ZPD)
400
200
0
−200
−400
−2
−1
0
1
2
-2 -1 0 1 2
-4 -3 -2 -1 0 1 2 3 4
-6 -5 -4 -3 -2 -1 0 1 2 3 4 5 6

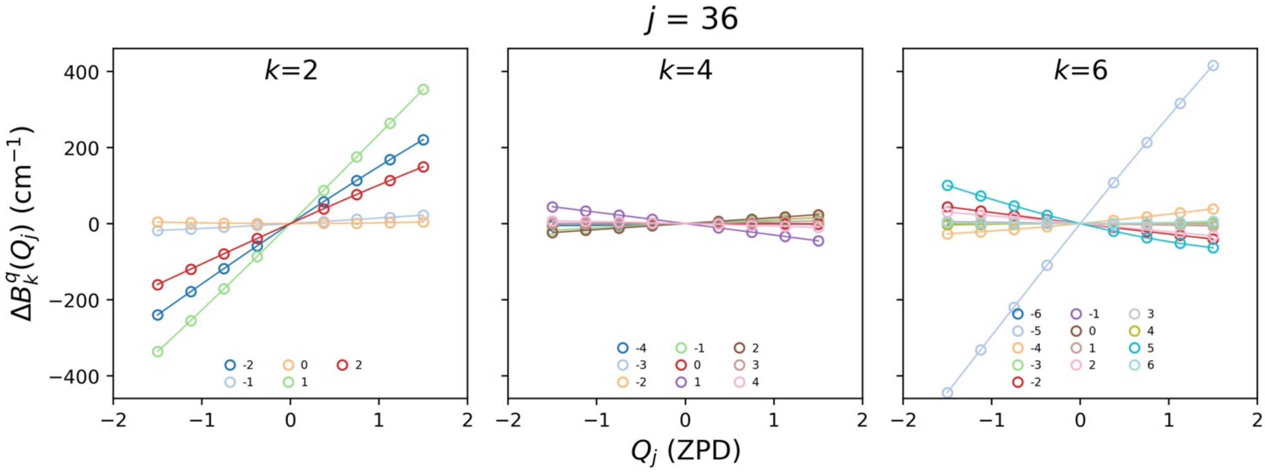
j = 36
k=2
k=4
k=6
$\Delta B_k^q(Q_j)$ (cm^{-1})
400
200
0
−200
−400
−2
−1
0
1
2
Q_j (ZPD)
-2
-1
0
1
2
-4
-3
-2
-1
0
1
2
3
4
-6
-5
-4
-3
-2
-1
0
1
2
3
4
5
6

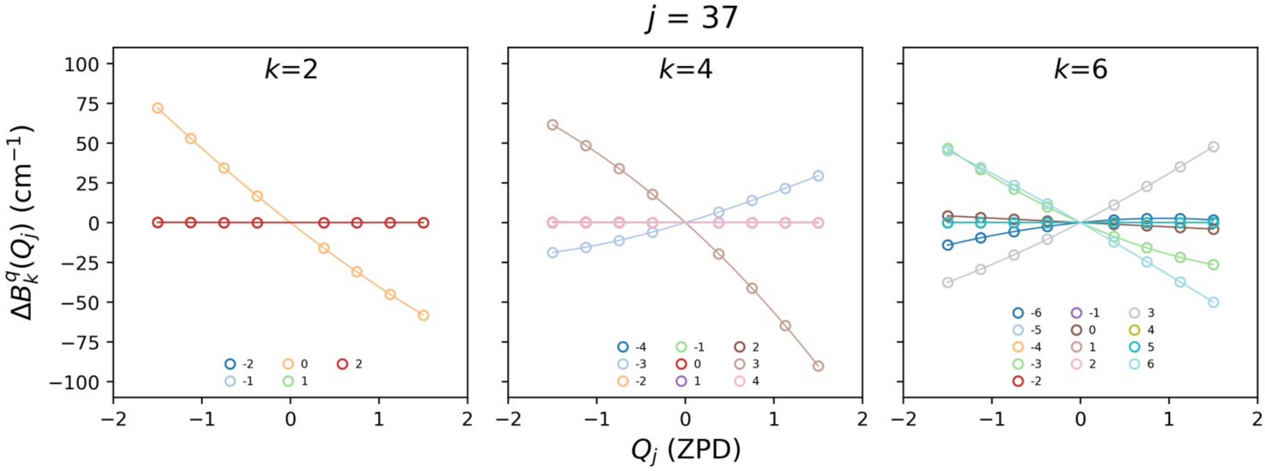
j = 37
k=2
k=4
k=6
$\Delta B_k^q(Q_j)$ (cm^{-1})
100
75
50
25
0
−25
−50
−75
−100
−2
−1
0
1
2
Q_j (ZPD)
-2
-1
0
1
2
-4
-3
-2
-1
0
1
2
3
4
-6
-5
-4
-3
-2
-1
0
1
2
3
4
5
6

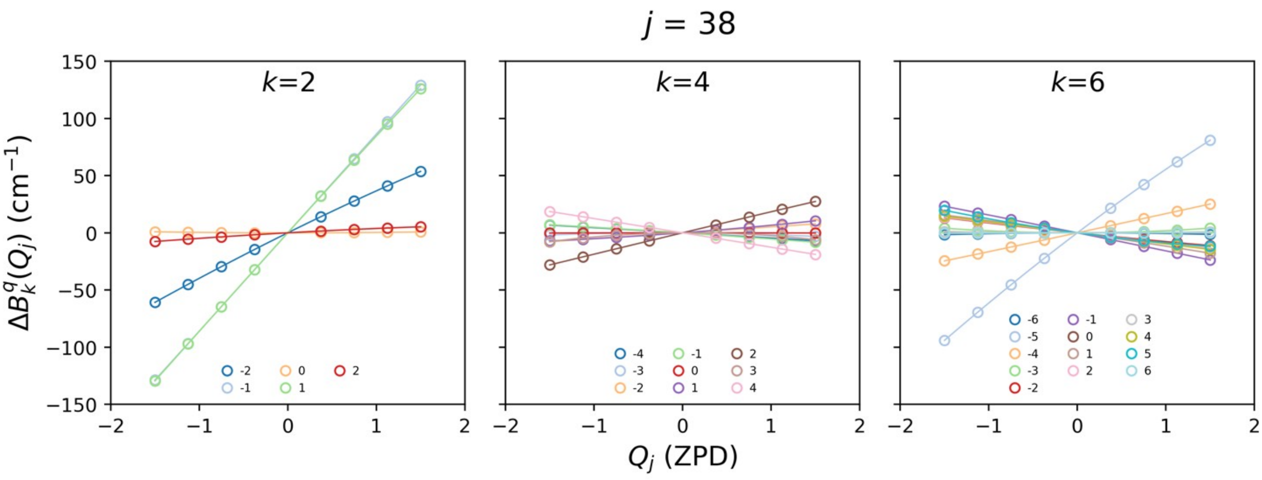
j = 38
k=2
k=4
k=6
$\Delta B_k^q(Q_j)$ (cm^{-1})
150
100
50
0
−50
−100
−150
-2 -1 0 1 2
-4 -3 -2 -1 0 1 2 3 4
-6 -5 -4 -3 -2 -1 0 1 2 3 4 5 6
−2 −1 0 1 2
Q_j (ZPD)

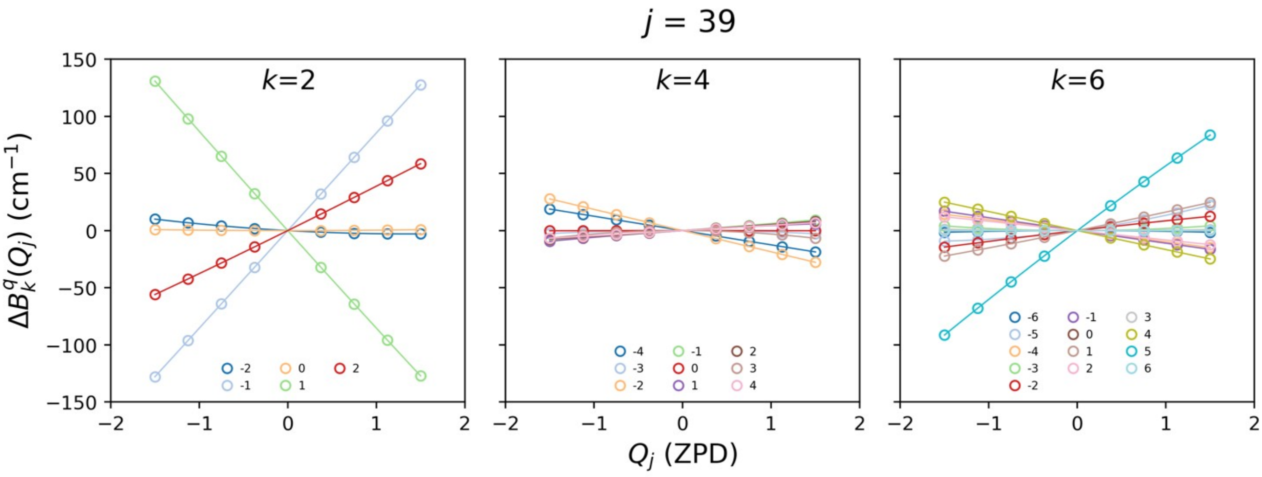
j = 39
k=2
k=4
k=6
$\Delta B_k^q(Q_j)$ (cm^{-1})
150
100
50
0
−50
−100
−150
-2 -1 0 1 2
-4 -3 -2 -1 0 1 2 3 4
-6 -5 -4 -3 -2 -1 0 1 2 3 4 5 6
−2 −1 0 1 2
Q_j (ZPD)

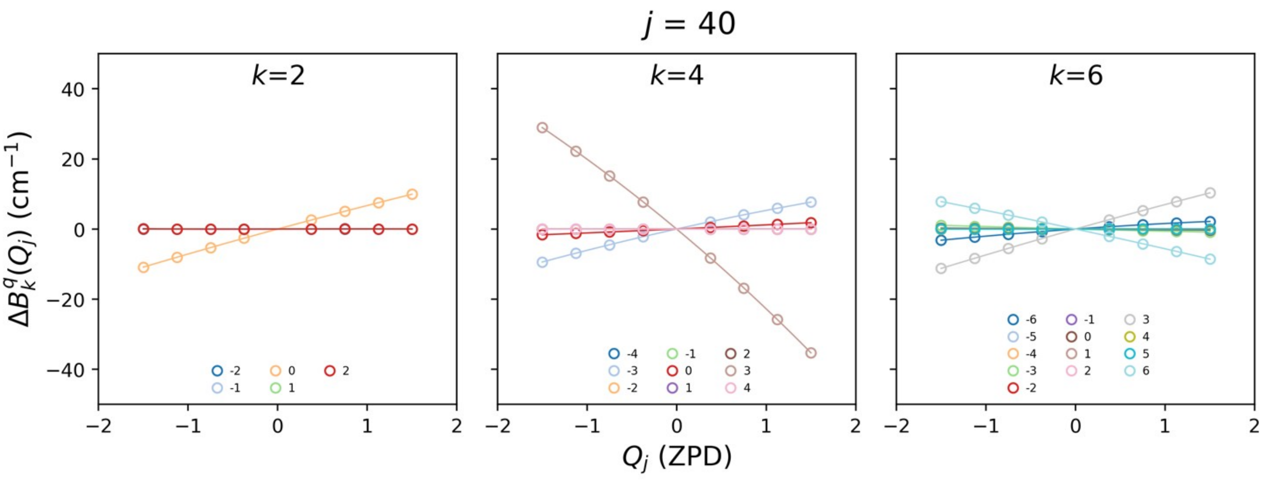
j = 40
k=2
k=4
k=6
$\Delta B_k^q(Q_j)$ (cm^{-1})
Q_j (ZPD)
40
20
0
−20
−40
−2
−1
0
1
2
-2
-1
0
1
2
-4
-3
-2
-1
0
1
2
3
4
-6
-5
-4
-3
-2
-1
0
1
2
3
4
5
6

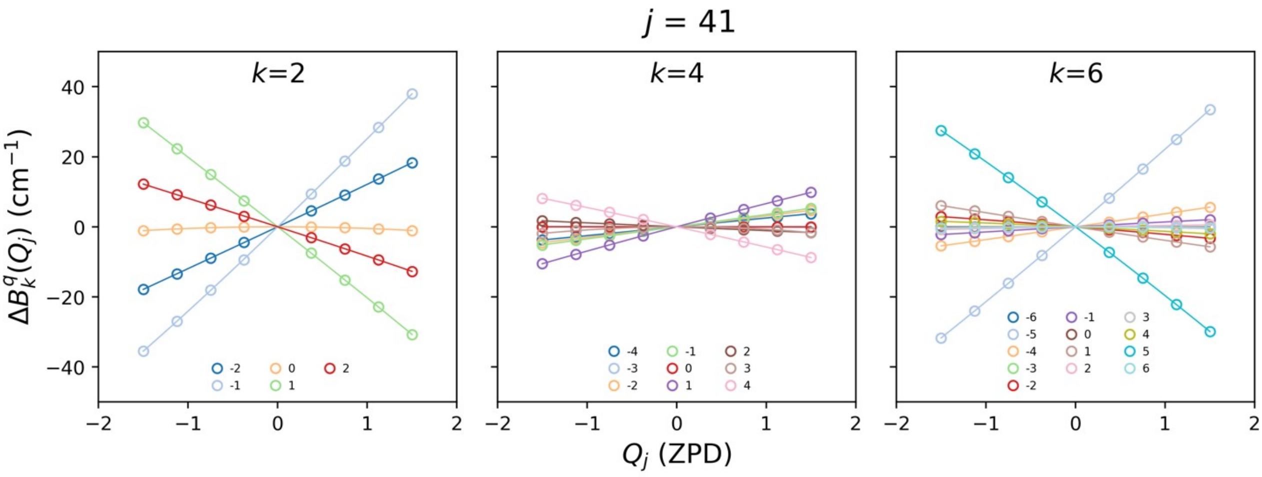
j = 41
k=2
k=4
k=6
$\Delta B_k^q(Q_j)$ (cm^{-1})
Q_j (ZPD)
40
20
0
−20
−40
−2
−1
0
1
2
-2
-1
0
1
2
-4
-3
-2
-1
0
1
2
3
4
-6
-5
-4
-3
-2
-1
0
1
2
3
4
5
6

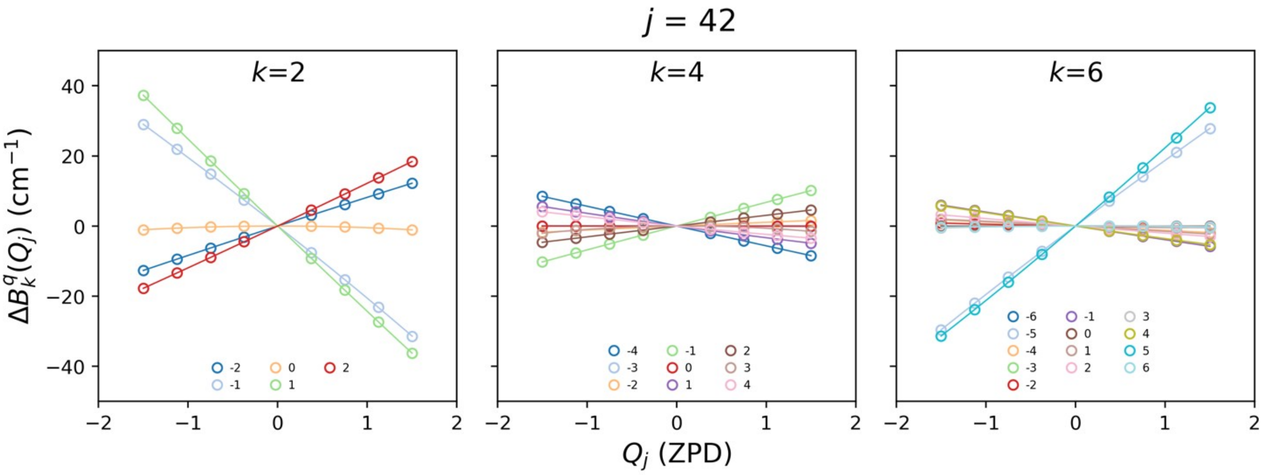
j = 42
k=2
k=4
k=6
$\Delta B_k^q(Q_j)$ (cm^{-1})
40
20
0
−20
−40
Q_j (ZPD)
−2
−1
0
1
2
-2
-1
0
1
2
-4
-3
-2
-1
0
1
2
3
4
-6
-5
-4
-3
-2
-1
0
1
2
3
4
5
6

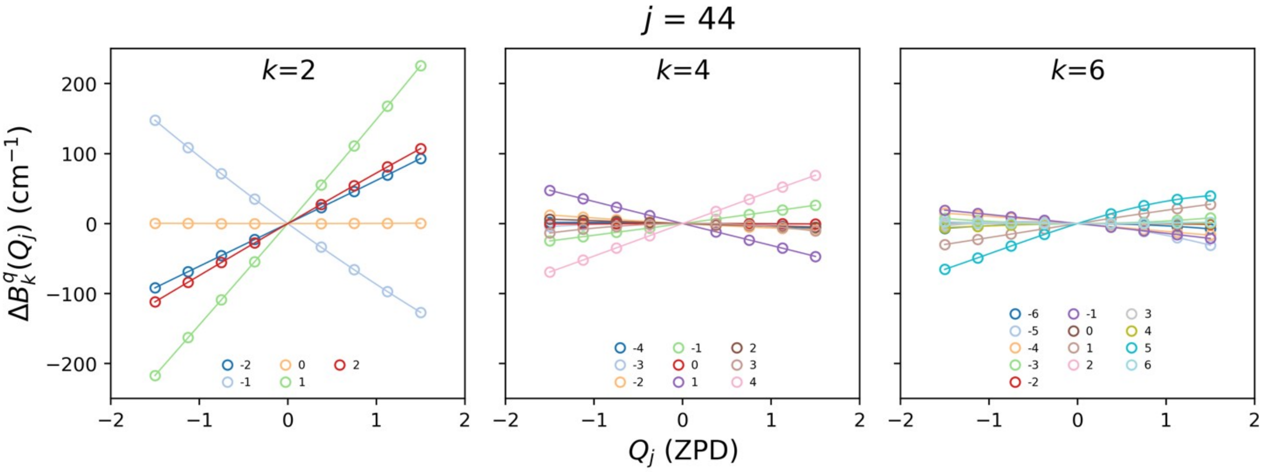
j = 44
k=2
k=4
k=6
$\Delta B_k^q(Q_j)$ (cm^{-1})
200
100
0
−100
−200
Q_j (ZPD)
−2
−1
0
1
2
-2
-1
0
1
2
-4
-3
-2
-1
0
1
2
3
4
-6
-5
-4
-3
-2
-1
0
1
2
3
4
5
6

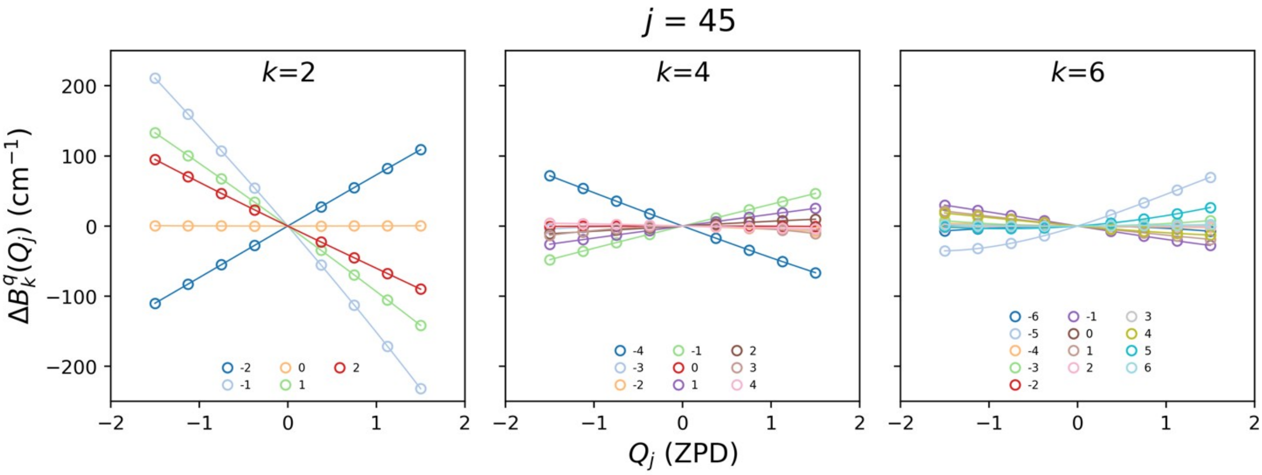

Figure S4: Fits of the changes in the crystal field parameters with third order polynomials as a function of displacement along vibrational modes 4, 5, 34-42, 44, 45. All fits are clearly dominated by linear terms, justifying our first-order Taylor expansion.

Experimental and theoretical FIRMS maps and analysis

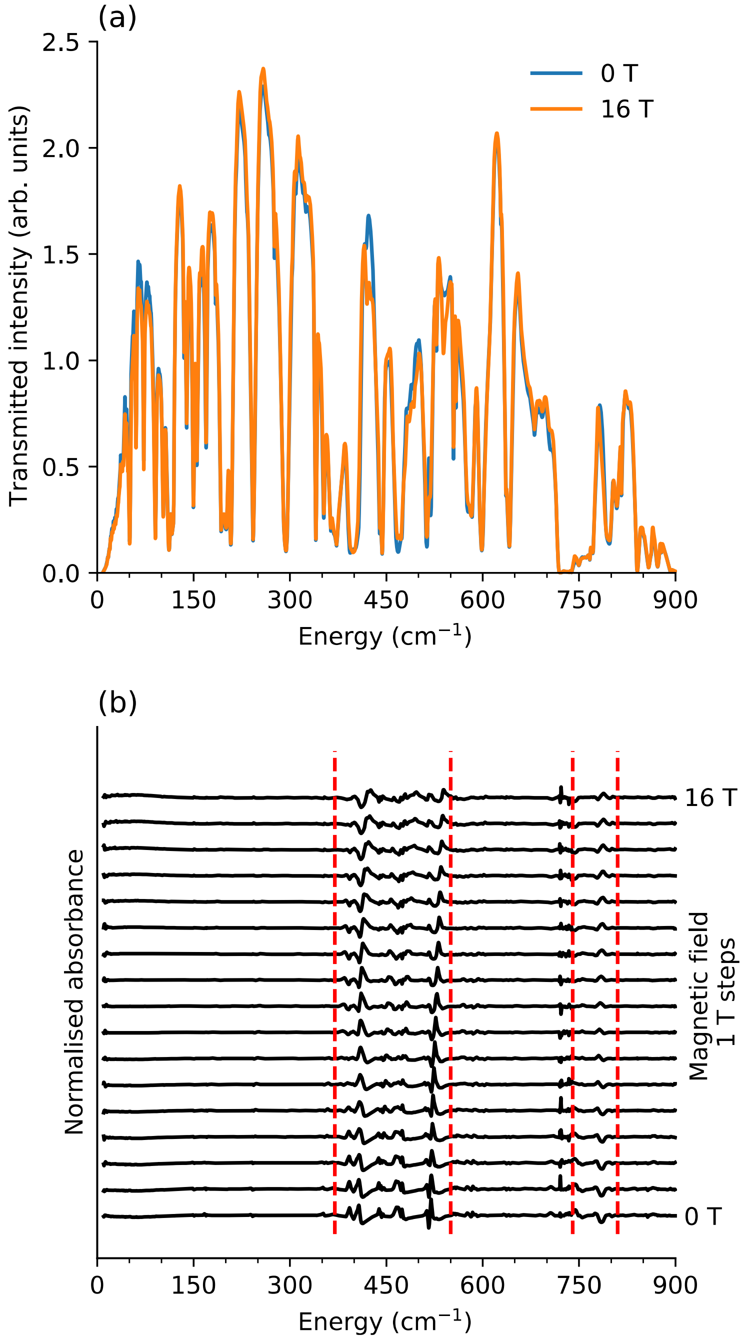

Figure S5: Far-infrared magnetospectroscopy (FIRMS) data for [Yb(trensal)]. (a) Raw FTIR spectra taken in 0 T and 16 T applied magnetic fields. (b) FIRMS spectra at different applied magnetic fields, normalised by the average of all spectra. Intense field dependent spectral features are highlighted by this division and appear in the ranges 370 to 550 cm^{-1} and 740 to 815 cm^{-1} (between dashed red lines – the features just below 740 cm^{-1} are artifacts caused by the spectrometer blind spot at ~720 cm^{-1}). All measurements were performed at 4.2 K.

A brief summary of the assignment of the main features of the FIRMS map is given in the main text, but here we give a more detailed account.

We begin with signal **A** ($E_{B=0}$ = 393 cm^{-1}) which moves to lower energy with increasing field; this is consistent with an electronically hot intra-KD transition ¿. This signal intersects with a band moving to higher energy in the field range 8 – 10 T and therefore could show some avoided crossing type behaviour; unfortunately, due to the low intensity of signal **A**, such behaviour is not seen within our current data. The nearby signal **B** ($E_{B=0}$ = 407 cm^{-1}) is likely the same as side-band 2a in the luminescence data (Figure 2), and is consistent with a cold intra-KD vibronic transition ¿. Both **A** and **B** emanate from a region of low IR transmittance that shows only small shifts at its edges due to vibronic coupling, hence their apparent field-independence near zero-field is likely an artefact of the normalisation scheme. Our DFT calculations predict a vibrational mode at 406 cm^{-1} (mode 34, A symmetry) which involves compression of the entire structure along the axial Yb-NR$_3$ direction (Supplementary Video 13), and a pair of modes of E symmetry at 413 cm^{-1} (modes 35 and 36) which are anti-symmetric N-Yb-N stretches (Table S5, Supplementary Videos 14 and 15). Considering the excellent agreement with the zero-field FTIR spectrum (Figure S2) and that there are no other vibrational modes within ±25 cm^{-1} of the **A** and **B** signals, we are confident with these assignments. Simulations of FIRMS maps obtained from coupling to modes 34-36 simultaneously (Figure S6) gives further weight to our assignment, allowing us to reproduce the broad nature of the vibronic signals seen in the experiment, specifically the dominant band at ~425 cm^{-1} that moves to higher energy with increasing field. Unfortunately in this simulation, the purely electronic ($¿1_{\pm}\rangle \rightarrow \vee 2_{\pm}\rangle$) signal occurs at much higher energy ($E_{B=0} \approx$ 495 cm^{-1}) than in the experiment ($E_{B=0} \approx$ 474 cm^{-1}). This shift is an artefact of our imperfect *ab initio* spin-phonon couplings, where the coupling strengths of these modes are much larger (S_j = 1.1, 2.1, 2.1 for j = 34, 35 respectively) than other modes used to simulate the remaining signals within the 370 cm^{-1} to 550 cm^{-1} region.

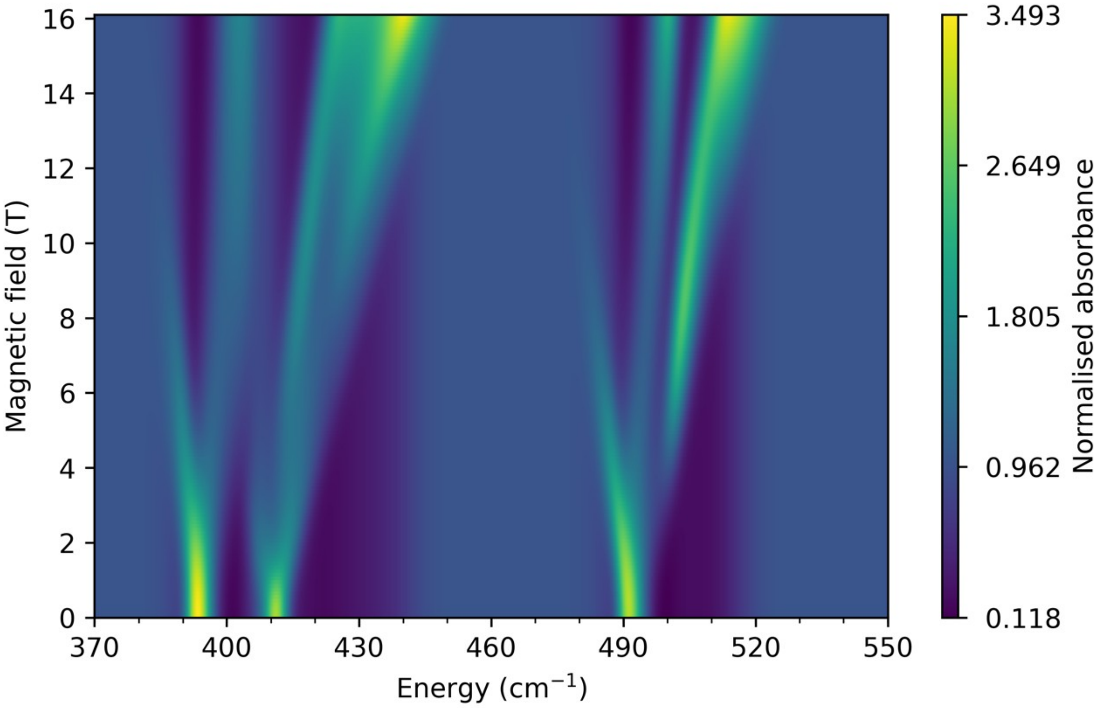

Figure S6: Simulated FIRMS map coupling to modes 34-36 using XMS-CASPT2-SO equilibrium CFPs with experimental CF energies and CASSCF-SO spin-phonon couplings.

Signal **C** ($E_{B=0}$ = 444 cm^{-1}) consists of an electronically hot intra-KD band which disappears at ~ 6 T and a cold intra-KD band. Our DFT results indicate a mode at 444 cm^{-1} (mode 37, A) in which the structure is compressed along the Yb-N dative bond (Supplementary Video 16), and a pair of modes at 446 cm^{-1} (modes 38 and 39, E) which are similar to modes 35 and 36 but include considerable motion of the amine nitrogen (Supplementary Videos 17 and 18). Simulations of the FIRMS map agree very well with the experimental data (Figure S7), specifically the weaker overall intensity compared to features **A** and **B** and the very broad high field arm around 460 – 480 cm^{-1}.

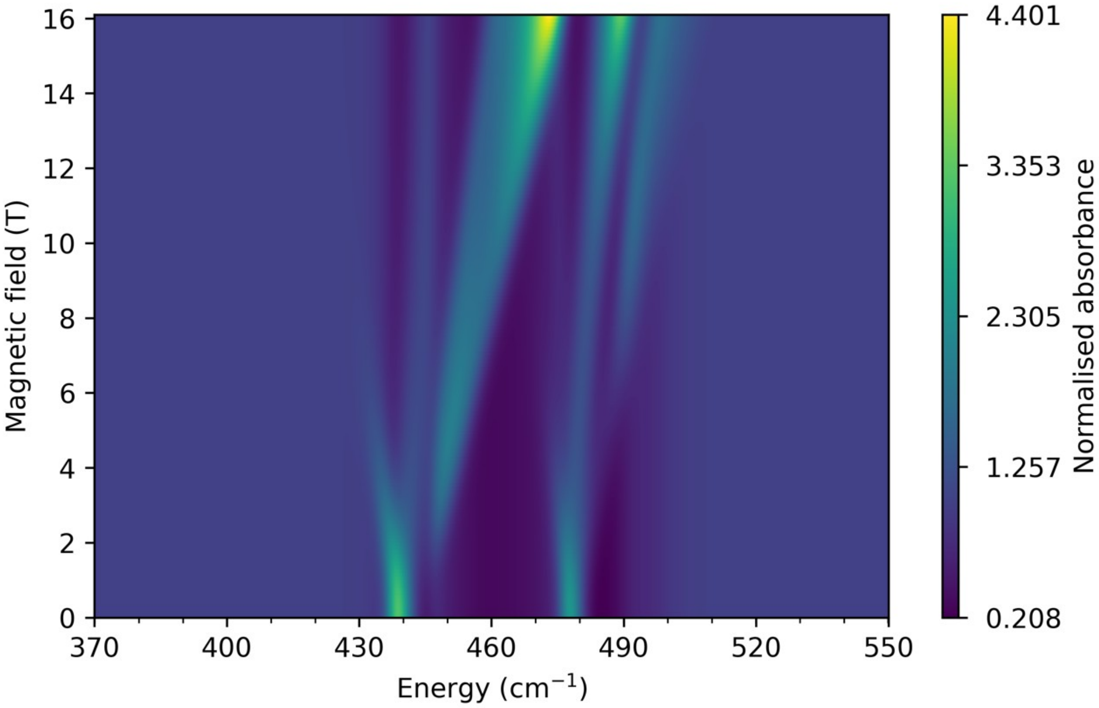

Figure S7: Simulated FIRMS map coupling to modes 37-39 using XMS-CASPT2-SO equilibrium CFPs with experimental CF energies and CASSCF-SO spin-phonon couplings.

Signals **D** ($E_{B=0}$ = 468 cm^{-1}) and **E** ($E_{B=0}$ = 474 cm^{-1}) are composed of many features at zero field which are poorly resolved, though we clearly see both hot and cold electronic bands moving as a function of field. Further, we note that signal **D** intersects with a band from signal **C** giving the appearance of an avoided crossing, but, similar to signal **A**, we do not see any interaction between the two, perhaps due to the low intensity of the peak that moves to low energy with field. Signals **D** and **E** are complicated as they are very close to the purely electronic transition at 474 cm^{-1}, and, hence, could be electronic ($|1_\pm, n\rangle \rightarrow |2_\pm, n\rangle$), intra-KD cold ($|1_\pm, 0\rangle \rightarrow |1_\pm, 1\rangle$, $\hbar\omega$ ~ 470 cm^{-1}) or inter-KD hot ($|1_\pm, 0\rangle \rightarrow |2_\pm, 1\rangle$, $\hbar\omega$ < 20 cm^{-1}) bands. Our DFT calculations do not clarify matters, as they reveal a mode at 473 cm^{-1} (mode 40, A, out-of-plane ring deformation of all aromatic rings, Supplementary Video 19), and two modes at 477 cm^{-1} (modes 41, 42, E, out-of-phase equivalents of mode 40, Supplementary Videos 20 and 21). While in reality there will be numerous acoustic phonon modes below 20 cm^{-1}, the IR transition intensities for these modes will be negligible compared to intramolecular modes. However, we cannot rule out contributions from hot vibrational bands. Nonetheless, our simulations of these signals using modes 40-42 are adequate (Figure S8), showing the broad band of intensity at zero field and overall very weak intensity.

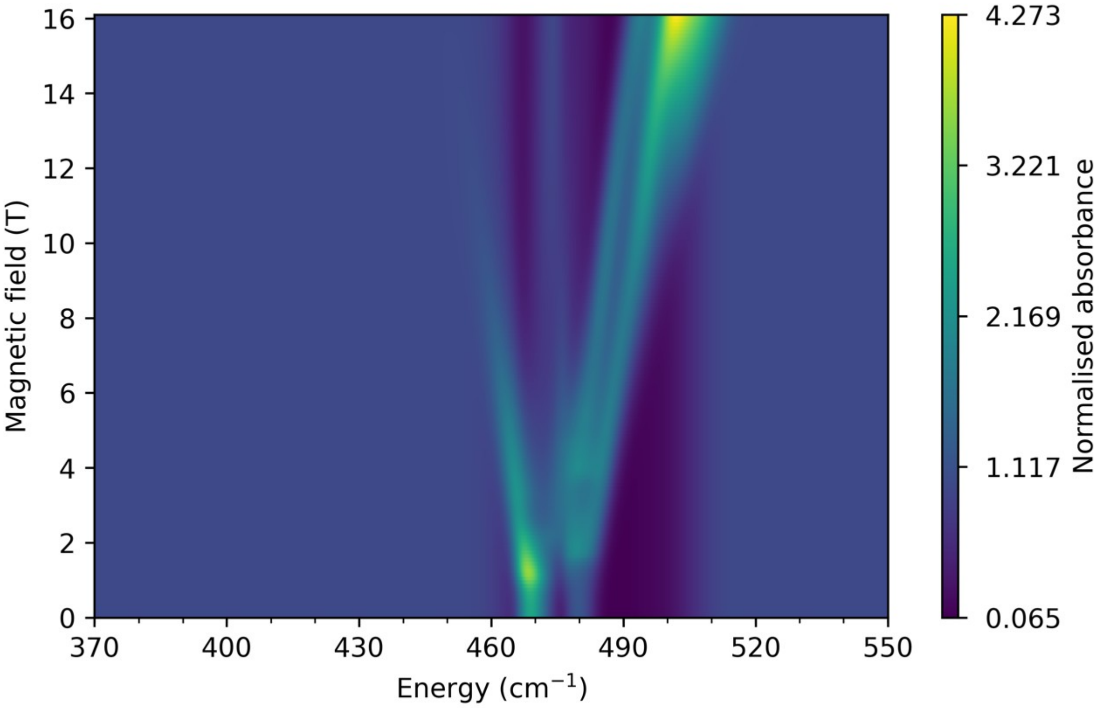

Figure S8: Simulated FIRMS map coupling to modes 40-42 using XMS-CASPT2-SO equilibrium CFPs with experimental CF energies and CASSCF-SO spin-phonon couplings.

The very intense signal **F** ($E_{B=0}$ = 520 cm^{-1}) corresponds to peak 2b in the luminescence measurements (Figure 2), and appears as a weak electronic hot band which fades for B > 5 T and a much stronger cold band. As these are higher in energy than the purely electronic transition, they could be either intra- or inter-KD vibronic transitions or both. In the case of an intra-KD transition, our DFT results indicate a mode of A symmetry at 516 cm^{-1} (mode 43) and a pair of modes of E symmetry at 521 cm^{-1} (modes 44 and 45), all of which are stretches of each N-Yb-O unit (Supplementary Videos 22-24). Alternatively, if these were inter-KD transitions, the energy of the vibrational mode would have to be *ca.* 46 cm^{-1}: there are indeed a pair of modes at 48 cm^{-1} (modes 4 and 5, E) which involve a rocking motion of the entire trensal unit (Supplementary Videos 1 and 2). Simulation of a FIRMS map including modes 43, 44 and 45 suggests that an additional signal should be present at ~537 cm^{-1} and that the purely electronic transition would borrow significant intensity from these modes to become dominant in the spectra (Figure S9), neither of these observations are compatible with the experiment (Figure 3). On the other hand, simulation of a FIRMS map with modes 4 and 5 show the correct intensity pattern, where signal **F** is dominant over the purely electronic transition (Figure S10). Thus, we suggest that signal **F** is a cold inter-KD transition $\left|1_{\pm},0\right\rangle \rightarrow \left|1_{\pm},1\right\rangle$ coupling to vibrational modes 4 and 5 at 48 cm^{-1}.

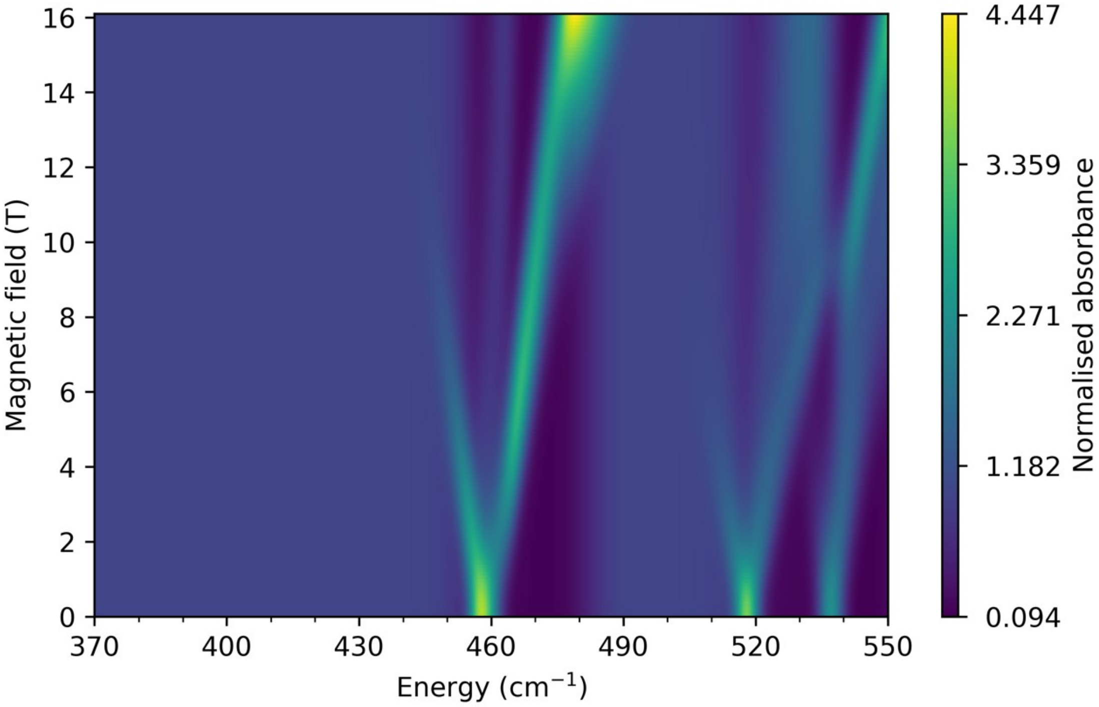

Figure S9: Simulated FIRMS map coupling to modes 43, 44 and 45 using XMS-CASPT2-SO equilibrium CFPs with experimental CF energies and CASSCF-SO spin-phonon couplings.

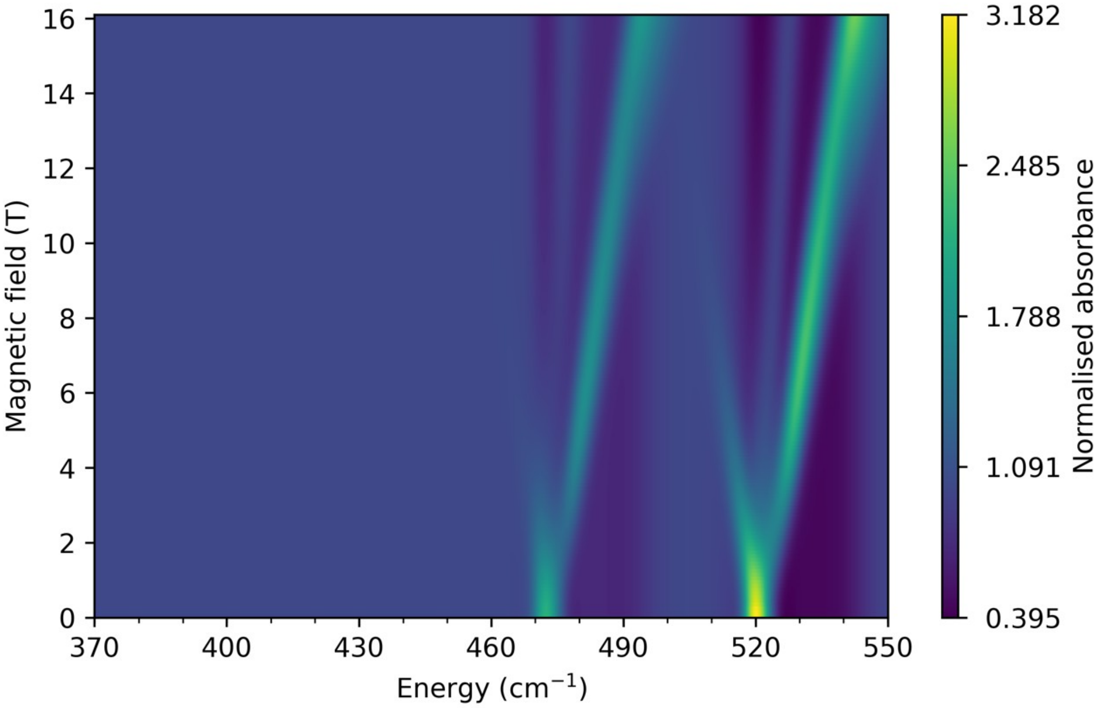

Figure S10: Simulated FIRMS map coupling to modes 4 and 5 using XMS-CASPT2-SO equilibrium CFPs with experimental CF energies and CASSCF-SO spin-phonon couplings.

Comparing the individual 3 mode simulations (Figures S6-S10) to the 9+2 mode composite simulation (Figure 3b) in the main text, we see almost identical results for the purely vibronic signals. This agreement is unsurprising, as we neglect the quadratic terms in Equation 5 which couple vibrational modes together. However, while the vibrational modes are separate from one-another, all will couple to the electronic structure simultaneously, and so we see only a single purely electronic signal ($|1_{\pm}\rangle \rightarrow |2_{\pm}\rangle, E_{B=0}$≈495 cm^{-1}) in our 9 mode simulation. This signal is significantly shifted from its experimental value ($E_{B=0}$≈ 474 cm^{-1}) and matches well with the electronic signal we see in the simulation involving only modes 34-36 (Figure S6), hence we conclude that the spin-phonon couplings of modes 34-36 are overestimated, and is the cause of the shift.

In the higher energy range near the second excited KD, there is a very intense signal **G** ($E_{B=0}$ ≈ 775 cm^{-1}) in the experimental FIRMS map which seems almost field independent at high (> 10 T) and low (< 6 T) fields, but more field dependent at intermediate fields (Figure S11). The shape of this signal is similar to that of the avoided crossings observed by Xue *et al.*, in which a purely electronic and field dependent transition interacts with a nearby purely vibrational transition.[5] Unfortunately, we are unable to see any signal corresponding to the nearby purely electronic $|1_{\pm}, n\rangle \rightarrow |3_{\pm}, n\rangle$ transition at zero field, as it lies in a region of low IR transmission. However, due to the relatively strong field dependence of signal **G** and its distance from the expected $|1_{\pm},n\rangle \rightarrow |3_{\pm},n\rangle$ transition energy (*ca.* 745 cm^{-1}), signal **G** is unlikely to be the result of an avoided crossing. Rather, we believe signal **G** is caused by an intra-Kramers vibronic transition, and will have an increased signal intensity due to its proximity to the nearby electronic transition. To account for its unusual shape, we note that, much like signals **A** and **B**, signal **G** emanates from a region of high IR absorption which effectively masks any less intense field dependent signals. Indeed, tracing backwards from the field-dependent region at 8 T (785 cm^{-1}) to 0 T gives $E_{B=0} \approx$ 765 cm^{-1}, which coincides with three modes in our DFT calculations at 762 cm^{-1} (modes 58 and 59, E, and mode 60, A, which are all out-of-plane bends of the aromatic hydrogens, Supplementary Videos 25-27), and a single mode at 768 cm^{-1} (mode 61, A, which is a Yb-NR$_3$ stretch, Supplementary Video 28), and thus signal **G** could result from an intra-KD transition coupled to modes 58-61. Alternatively, similar to signal **F**, signal **G** could be caused by an inter-KD transition $|1_{\pm},0\rangle \rightarrow |3_{\pm},1\rangle$ with a mode of *ca.* 10-30 cm^{-1}, or a $|1_{\pm},0\rangle \rightarrow |2_{\pm},1\rangle$ inter-KD transition with a mode around 290 cm^{-1}. Given the plethora of possible origins for this signal, its broad character, and its positioning adjacent to a strong IR absorption, we do not attempt to simulate this signal here.

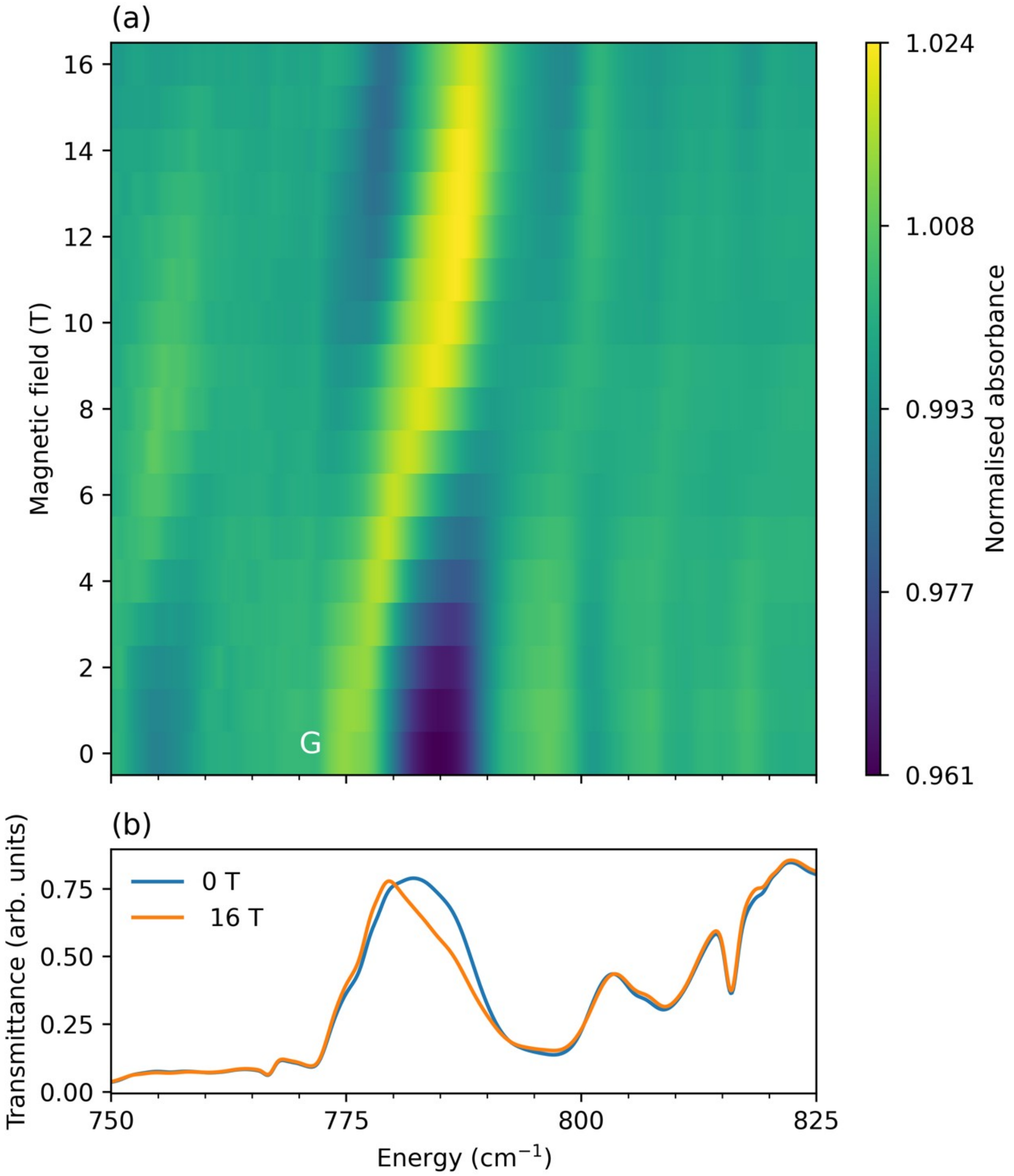

Figure S11: (a) Experimental FIRMS map measured at 4.2 K in the range 750 to 825 cm^{-1}; field dependent signal labelled as **G**. (b) Raw FTIR spectra taken in 0 T and 16 T applied magnetic fields.

In the lower energy range, there are weak signals in the experimental FIRMS map at 167 cm^{-1}, 238 cm^{-1}, 553 cm^{-1}, 581 cm^{-1}, all of which are distant from any electronic transitions (Figures S12 and S13). Of these, the former two are clearly present in the luminescence measurements (Peaks 1a and 1c, Figure 2) and are intra-KD vibronic transitions at energies which match those of vibrational modes from our DFT calculations (Table S5). The energies of the latter two signals match well with vibrational modes from DFT and could be intra-KD signals. However, as they are also above the energy of the first excited electronic state they could also be inter-KD transitions involving low energy modes which are also present in our DFT results.

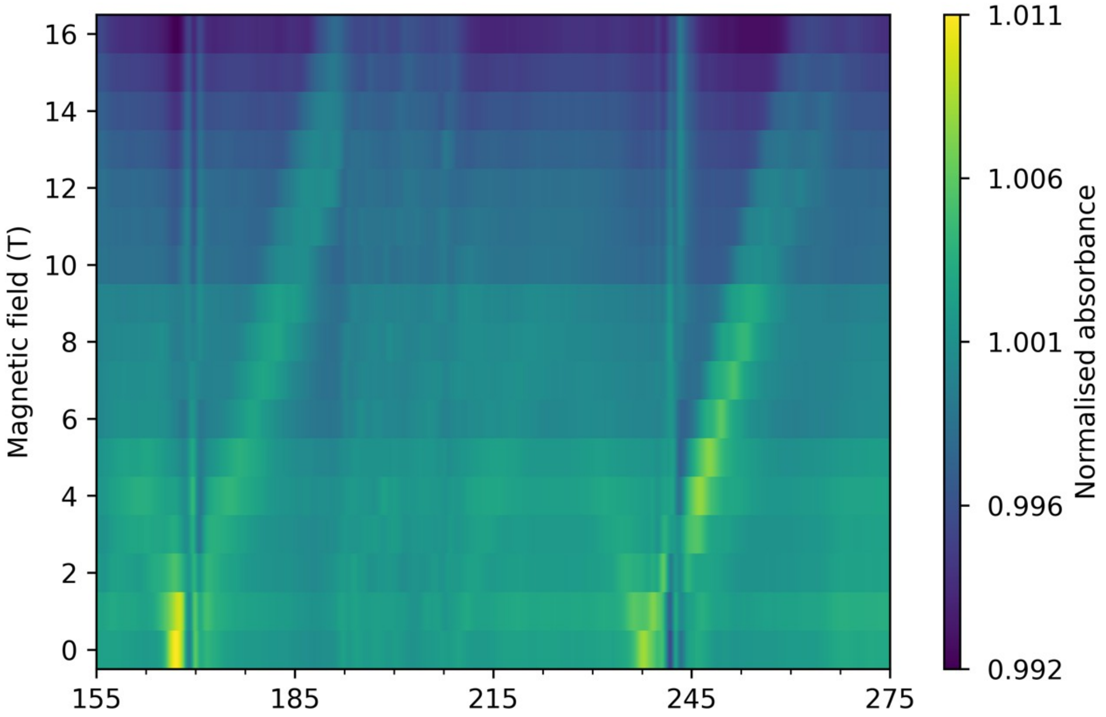

Figure S12: Experimental FIRMS map measured at 4.2 K in the range 155 to 275 cm^{-1}.

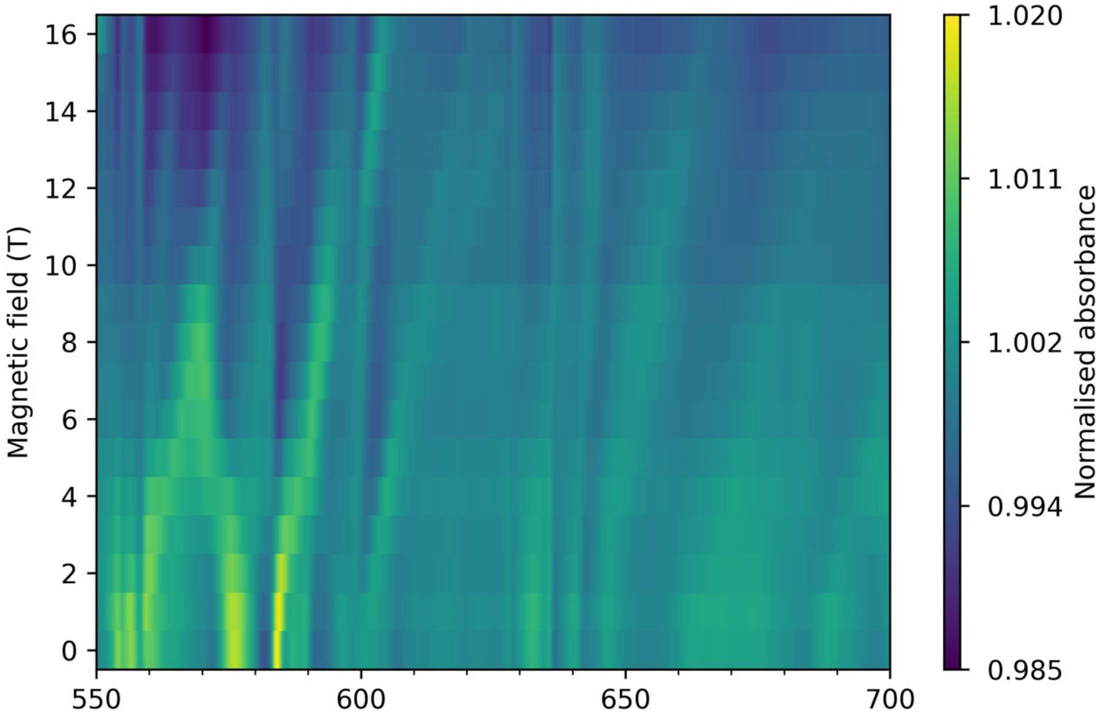

Figure S13: Experimental FIRMS map measured at 4.2 K in the range 550 to 700 cm^{-1}.

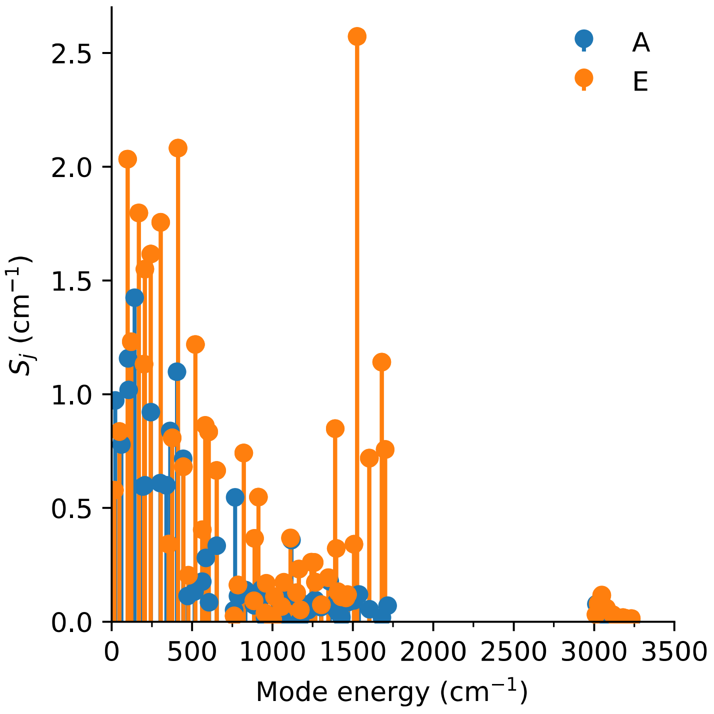

Figure S14: *Ab initio* calculated vibronic coupling strength S_j of modes of $\mathbf{1}_{\mathbf{opt}}$ with A (blue) and E (orange) symmetry.

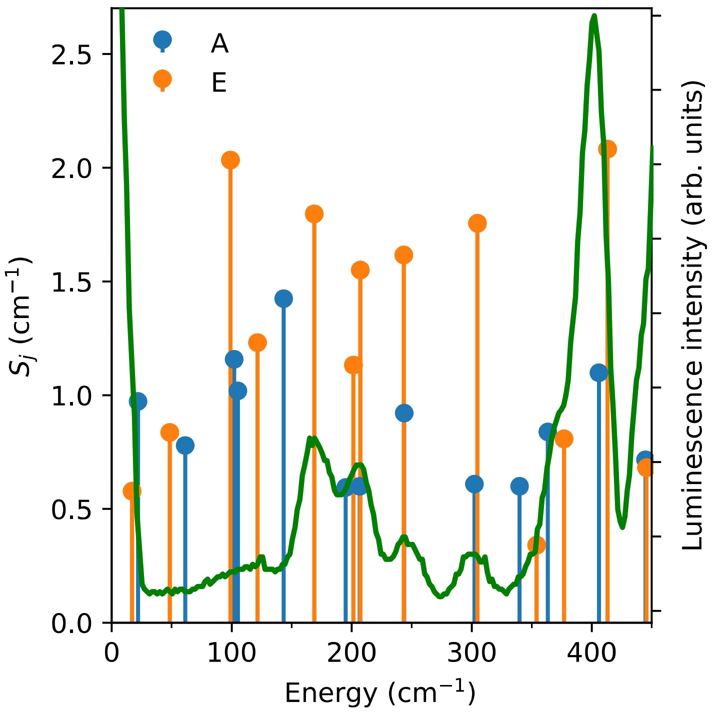

Figure S15: Ab initio calculated vibronic coupling strength S_j of modes of $\mathbf{1}_{\mathbf{opt}}$ with A (blue) and E (orange) symmetry superimposed onto the luminescence spectrum (green) of **1** in the region 0 cm^{-1} to 450 cm^{-1}.

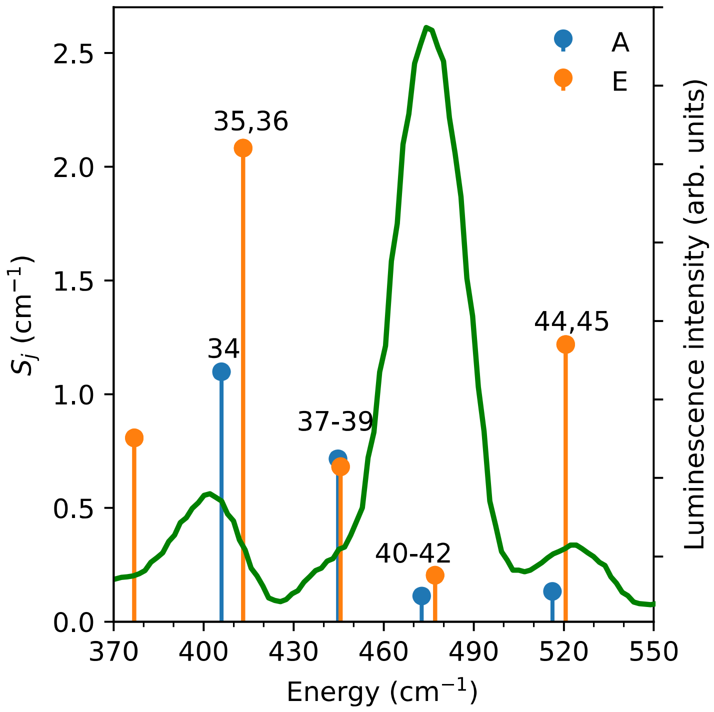

Figure S16: Ab initio calculated vibronic coupling strength S_j of modes of $\mathbf{1}_{\mathbf{opt}}$ with A (blue) and E (orange) symmetry superimposed onto the luminescence spectrum (green) of **1** in the region 370 cm^{-1} to 550 cm^{-1}.

References

1 K. S. Pedersen, J. Dreiser, H. Weihe, R. Sibille, H. V. Johannesen, M. A. Sørensen, B. E. Nielsen, M. Sigrist, H. Mutka, S. Rols, J. Bendix and S. Piligkos, *Inorg. Chem.*, 2015, **54**, 7600–7606.

2 R. Orbach, *Proc. R. Soc. London. Ser. A. Math. Phys. Sci.*, 1961, **264**, 458–484.

3 P. W. Atkins and R. S. Friedman, *Molecular Quantum Mechanics*, Oxford University Press, Oxford, 4th edn., 2006.

4 M. Eden and M. H. Levitt, *J. Magn. Res.*, 1998, **132**, 220–239.

5 D. H. Moseley, S. E. Stavretis, K. Thirunavukkuarasu, M. Ozerov, Y. Cheng, L. L. Daemen, J. Ludwig, Z. Lu, D. Smirnov, C. M. Brown, A. Pandey, A. J. Ramirez-Cuesta, A. C. Lamb, M. Atanasov, E. Bill, F. Neese and Z. L. Xue, *Nat. Commun.*, 2018, **9**, 2572.

yb_trensal_SI_final.docx (4.33 MiB) view on ChemRxiv • download file